Chapter 5

Syntheses, characterization and SOD synzyme activity of copper(II) complexes with bi-dentate pivalamide ligands – Crystallography, DFT studies and DNA/BSA interactions

Published in Polyhedron, 225 (2022) 116054.

5.1 INTRODUCTION

Crystal engineering of coordination complexes is an interesting branch of supramolecular chemistry.[1] Although crystallography is essentially linked with the H-bonded interactions in organic solids, it has immensely contributed to the study of metal complexes and organometallic compounds. In coordination chemistry, crystal engineering majorly corresponds to two- or three-dimensional extended networks of ligand to metal bonds, *via* polydentate ligands. Just as in organic solids, supramolecular synthons can be efficiently employed to study the H-bonded motifs in inorganic compounds as well.[2–5]

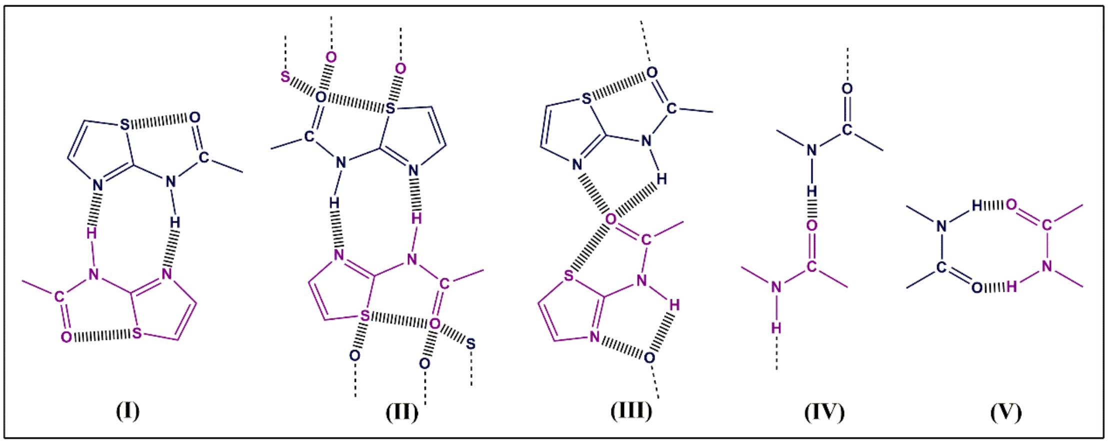

Scheme 5.1 Possible Hydrogen-bonding models in thiazole based amides

In our earlier studies, we have established that pivalic acid-based salts have a great potential to act as two-component gelators.[6] There have been several reports based on gelation studies of HSA (12-hydroxy stearic acid) which confirm that efficiency of gelation in aromatic solvents is maximum for primary amides.[7] This inspired us to synthesize pivalic acid-based amides containing various aliphatic, alicyclic and heterocyclic (thiazole and imidazole based) backbones, as our group has previously explored the properties of thiazole based gelators in great detail.[8,9] We recently reported a study based on phase selective organo-gelation of pivalamides with aromatic and aliphatic backbones.[10,11] While we could not obtain any gelators in these heterocyclic backbones containing amides **(L1-L5)**, we exploited these for the synthesis of mononuclear copper metal complexes **(C1-C5)** to get an insight into their intermolecular H-bonding patterns and the types of supramolecular synthons exhibited by them (Scheme 5.1). These supramolecular assemblies were assigned graph sets in order to determine the preferred modes of hydrogen bonding in their crystal structures.[12] All the crystal structures were subjected to Hirshfeld surface analyses to quantify the contribution of various non-covalent interactions towards stability and overall packing in the crystalline state.

Additionally, thiazole containing compounds are widely known for their exclusive biological properties like anti-protozoal, anti-convulsant, anti-diabetic, anti-inflammatory, anti-tumor, antiviral, and many more because of the presence of toxophoric –N=C–S– group. Thiazole based metal complexes have been widely studied in the past for their promising anti-fungal, anti-bacterial and cytotoxic behavior.[13–15] This inspired us to investigate the properties of synthesized complexes for their newer biological activities.

5.2 BACKGROUND

In coordination chemistry, the binding of bioactive molecules to their bioactive targets occurs primarily through supramolecular interactions. With decades of dedicated work in the design and synthesis of novel supramolecular architectures, supramolecular synthesis of multi-functional systems has evolved and brought us closer to develop such systems for the betterment of mankind. The key is to gain control over supramolecular assemblies, which can contribute to development of host-guest assemblies, target selective drug delivery, biosensors, tissue engineering, etc.[16]

Dismutation of superoxide ion.

The superoxide ion is a product of oxygen metabolism in the living systems and can be a mediator of reperfusion diseases such as myocardial infarction (stroke), initiate inflammatory processes associated with diseases like arthritis, even cause oxidative injury to the tissues which can lead to various neurological disorders like Parkinson’s and Alzheimer’s.[17] The superoxide radical ($O_2^{\cdot -}$), hydroxyl radical (HO^-) and hydrogen peroxide (H_2O_2) are called Reactive Oxygen Species (ROS) which are generated in the body as a result of oxidative stress when the level of antioxidants in the body is depleted either by redox metals such as chromium and copper or redox-inactive metals such as lead and cadmium.

Naturally occurring superoxide dismutases (SOD) in living systems contain Cu/Zn and Mn centers, which act as a natural defense mechanism against the superoxide-mediated oxidative damages in the cells.[18,19] The catalytic cycle of a conventional SOD follows a 'ping-pong' mechanism, where disproportionation of two superoxide anions ($O_2^{\cdot -}$) forms molecular oxygen (O_2) and hydrogen peroxide (H_2O_2), as shown in Scheme 5.2.

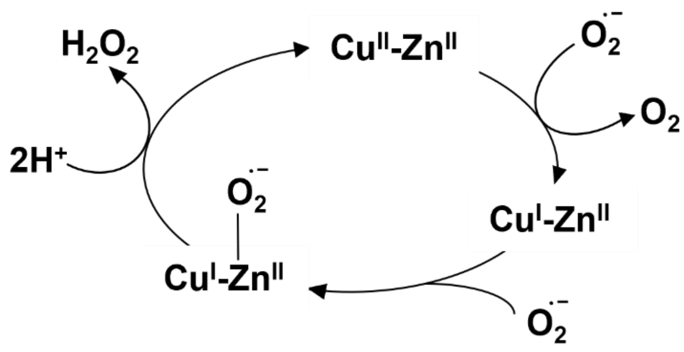

Scheme 5.2 Catalytic cycle in a conventional SOD complex

It has been long known that redox-active transition metal ions in a coordination environment make good candidates for biological catalytic activity in redox reactions.[20] Specially, those containing copper(II) have potentials matching with reactive oxygen species and hence they can be best utilized in catalyzing the dismutation of superoxide anion.

Synthetic enzymes (*synzymes*) which can mimic a natural enzyme function carry a potential to act as pharmaceutical agents for the treatment of aforementioned neuro degenerative disorders and may possess superior anticancer activity. In that regard, low molecular weight SOD mimics are of prime importance as they have the ability to access intercellular space, cellular permeability, longer half-life in the blood, potential for oral delivery, etc. and naturally, umpteen SOD mimicking complexes have been prepared and reported in the literature.[19,21,22] Most commonly employed complexes possess either mono/bi-nuclear Cu^{2+} and/or Zn^{2+} centers. This inspired us to exploit the abilities of the synthesized copper(II) complexes to act as SOD *synzymes*. The study has been further extended to assess the DNA cleavage ability of all the ligands and complexes.

DNA cleavage studies.

Complexes which can cleave nucleic acids at desired sites in suitable pH conditions can be very useful in the area of genetic engineering, tumor treatment and anti-microbial/anti-viral applications. It is believed that as compared to natural enzymes, artificial nucleases have more resistance to harsh reaction conditions and act with greater efficiency and selectivity in cleaving DNA chain.

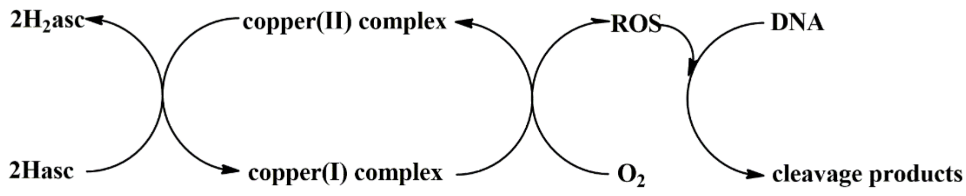

Scheme 5.3 DNA cleavage in presence of ascorbic acid

Among synthetic nucleases, metal complexes have higher catalytic activity and binding ability than other metal ions. These artificial nucleases can be customized by using different metal ions, coupled with a wide range of ligands. DNA cleavage property is also found to be dependent on the coordination number of the ion, ligand geometry, ligand size, type and electrical charge, core metal–metal distances and type of bridging group, and a hydrophobic environment around the ion, etc.[23,24]

The DNA cleavage mechanisms are of mainly two types – 1. hydrolysis and 2. oxidative cleavage. Generally, oxidative cleaving agents show high efficiency and versatility but require the addition of oxidative and/or reductive agent to initiate cleavage. Also, oxidative cleavage is mediated by reactive oxygen species (ROS) that are diffusible and can cause other severe cytotoxic effects. These drawbacks hamper their use *in vivo*. In that regard, hydrolytic cleavage of DNA in the absence of any external agents does not suffer from these disadvantages. It involves scission of the phosphoester bond to generate fragments which can be subsequently identified. Hydrolysis requires a metal ion capable of binding hard oxygen atoms, polarizing bonds and rapid ligand exchange for a decent catalytic turnover. Metal ions such as zinc(II), iron(III), lanthanum(III), copper(II), cobalt(III), etc. have been chosen for DNA cleavage studies because of their ability in assisting Lewis activation, nucleophile generation, and leaving group stabilization, make them suitable for the catalysis of hydrolytic reactions of DNA. As compared to mononuclear complexes, dinuclear complexes have higher activity as a result of the cooperative interaction of metal ions in stabilizing the transition state of phophodiester cleavage.[25–27]

DNA binding.

A variety of studies focusing on small molecules which react with the DNA strands *via* multiple non-covalent interactions (such as van der Waals interactions, H-bonding with the functional units bound along the groove of DNA helix and π-π interactions with the intercalation of aromatic heterocyclic groups between the base pairs) make them potential candidates for drug design.[28,29] Small molecules have the capability to stabilize the so-called adducts formed as they can conveniently bind with the DNA strands (*via* intercalation, insertion, groove binding and by discrete phosphate coordination, also called the 'phosphate clamp'[30]) without altering its configuration (Figure 5.1).

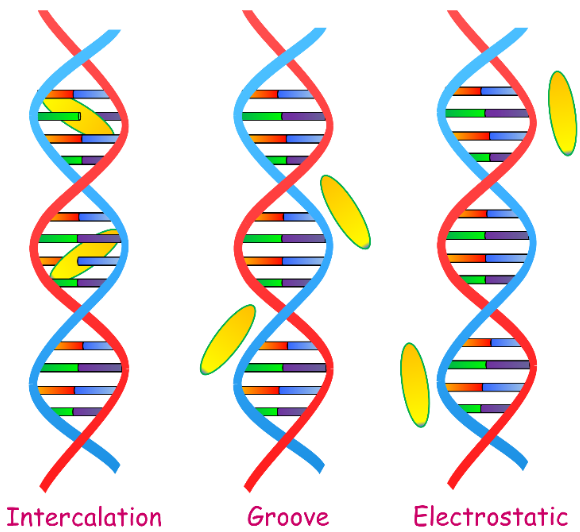

Figure 5.1 Possible modes of DNA binding

Transition metal complexes which form chelates are known for their potential to act as agents for probes of DNA structure in solution, mediation of strand scission, chemotherapeutic agents and so on. In this regard, transition metal complexes have proved to be a fascinating class as they exhibit well defined coordination geometries and very distinctive chemical, electrochemical and photo-physical properties which enhance the functionality of the binding agents. It has also been established that such transition metal complexes have an intrinsic ability to bind to DNA.

BSA interactions.

Serum albumins are the most soluble proteins found in mammalian blood plasma and play an important role in many physiological functions. They are also involved in transportation, distribution and metabolism of drugs, amino acids and metal ions. Investigation of binding mechanism of drugs with serum albumins is very important as it influences the absorption, distribution, metabolism and excretion of the drugs. In that regard, Bovine Serum Albumin (BSA) is most commonly used while establishing relevant models for establishing the affinity of small molecules with albumins. It is widely available, inexpensive and structurally resembles Human Serum Albumin (HSA) by approx. 76%.[31,32]

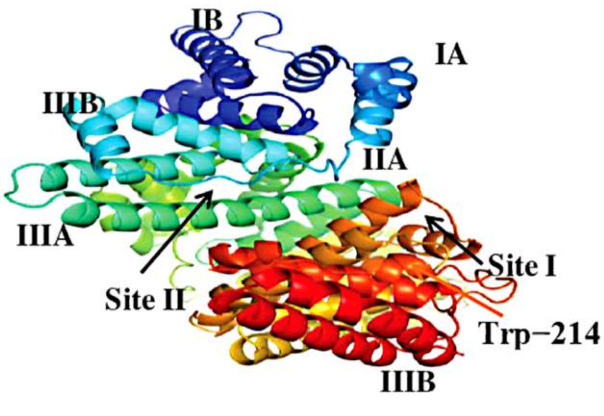

Figure 5.2 Discrete binding sites of BSA protein

BSA is a globular, non-glycosylated protein, made of 583 amino acid residues which are bound in a single chain and crosslinked *via* 17 cysteine residues with a molecular mass of 66400 Da. The high solubility of BSA arises from the presence of ionized residues, such as glutamic acid and lysine and very content of tryptophan, methionine, isoleucine, etc. These ionized residues confer the protein with a high charge, of 185 ions/molecule at a neutral pH.[32]

Many drug molecules are known to reversibly bind with very specific sites of BSA protein. The most prominent are sites I and II (Figure 5.2). These binding properties are investigated using fluorescence spectral titration. BSA protein in its own right can emit intensely upon excitation, due to the presence of three amino acid residues: tryptophan, tyrosine and phenylalanine with a relative intensity ratio of 10:9:0.5. The metal complex is considered to bind with BSA when the fluorescence intensity around 345 nm decreases with a gradual addition of complex.

Fluorescence quenching can occur mainly *via* two mechanisms, 1. static quenching, where a non-fluorescent ground-state complex is formed between the fluorophore and the quencher and 2. dynamic quenching, a collisional process where the fluorophore and quencher interact during the transient existence of the excited state. The BSA interaction has been found to be highly pronounced with mono- and polynuclear complexes of Cu^{2+}, Ni^{2+}, Zn^{2+}, Co^{2+}, Pt^{2+}, etc. containing ligands having pharmacologically active moieties. It has also been suggested that the planarity of the ligands coordinating with the metal center can play an important role in enhancing protein binding ability.

In the light of above facts, we hereby report the antioxidant SOD enzymatic activity, DNA cleavage, BSA protein binding and ct-DNA binding studies of the synthesized copper(II) complexes (**C1-C5**).

5.3 EXPERIMENTAL PROCEDURES

5.3.1 Synthesis of amides/ligands

Pivaloyl chloride (0.5 mL, 4 mmol) (in dry dichloromethane) was added to a solution of amine (4 mmol) and triethylamine (0.5 mL, 4 mmol) in a round bottom flask. The mixture was stirred under N_2 atmosphere overnight. The reaction mixture was then added to dil. HCl (5%) and extracted several times with dichloromethane. The combined dichloromethane phases were dried over Na_2SO_4 and the solvent was removed on rotary evaporator (Scheme 5.4).

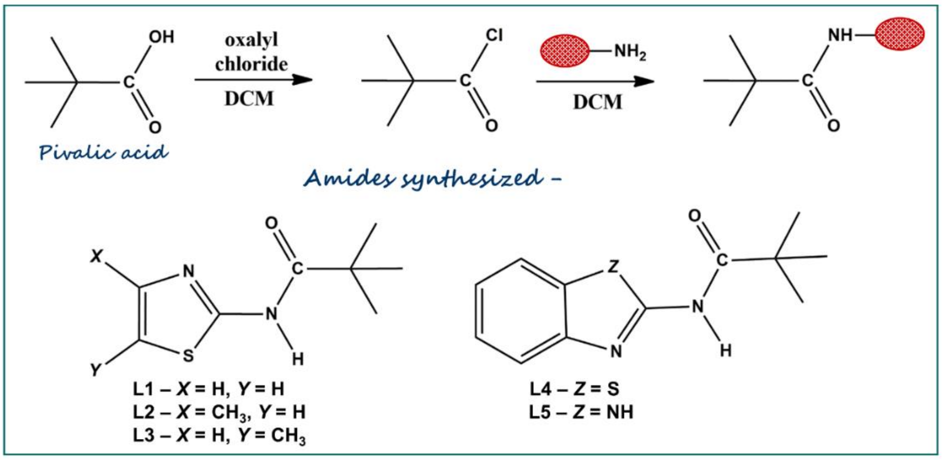

Scheme 5.4 Heterocyclic pivalamide ligands L1-L5 synthesized in the study

5.3.2 Synthesis of metal complexes

A methanolic solution of $Cu(CH_3COO)_2.H_2O$ (0.2 g, 1 mmol) was added dropwise to the subsequent pivalamide ligands (**L1-L5**, 2 mmol) dissolved in 10 mL methanol and stirred overnight to obtain a clear bluish green solution. The solutions were filtered, and the solids obtained kept for recrystallization in different solvents (Scheme 5.5).

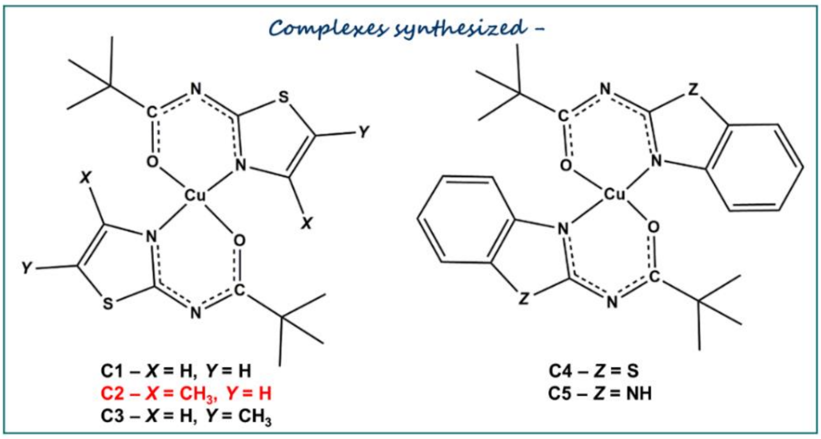

Scheme 5.5 Copper(II) metal complexes C1-C5 synthesized using L1-L5

5.3.3 Antioxidant assay

The superoxide dismutase (SOD) activity was measured using NADH-PMS-NBT method (Scheme 5.6).[33] Non-enzymatic (NADH-PMS-NBT) system contained 30 μM PMS and 80 μM NADH in phosphate buffer(pH=7.8) at RT (313 K) was used to produce superoxide ion which reacted with 75 μM NBT to form bluish-black colored formazan complex. The absorbance of the solutions was monitored at 560.0 nm at various concentrations of the complexes under uniform conditions in triplicates.

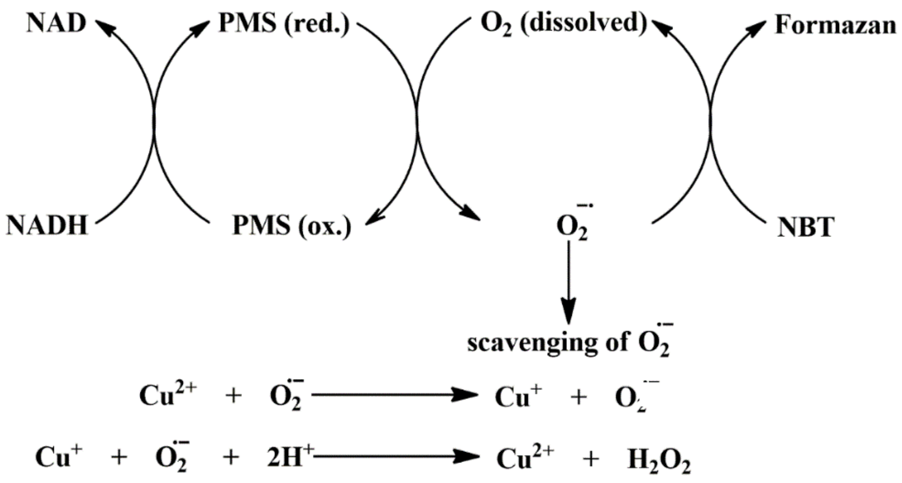

Scheme 5.6 Assessing SOD mimic activity using NADH-PMS-NBT method

The %inhibition of NBT reduction was calculated using equation 5.1 –

$$\%\textbf{inhibition of NBT reduction at a particular concentration} = \frac{(A_{blank} - A_{sample})}{A_{blank}}\ x\ 100\%$$

-(5.1)

The IC_{50} value was calculated as the concentration of the complex that caused 50% inhibition of NBT reduction, from the plots of %inhibition vs. concentration of complex (μM).

5.3.4 DNA cleavage studies

The cleavage studies were performed using agarose gel electrophoresis.[34,35] E. coli supercoiled plasmid DNA (obtained from HiMedia plasmid extraction kit) was incubated with different concentrations of complexes (1-80 μM) and ligands (50, 80 μM) in tris(hydroxymethyl)-aminomethane-HCl (15mM)/NaCl (150 mM) buffer (pH adjusted to 7.5 with conc. HCl) for 1 hour in presence of 10 mM H_2O_2 at 30°C. The agarose gel (1%) was prepared in TBE (Tris.HCl-Boric acid-EDTA) buffer containing ethidium bromide (0.5 μg/mL). Gel electrophoresis experiment was run in TBE (Tris.HCl-boric acid-EDTA) buffer at 100 V for 1 hour. The samples were loaded using loading buffer containing 25% bromophenol blue and 0.25% xylene cyanol prepared in 30% glycerol. The bands were visualized in Biorad UV imaging chamber. The amount of DNA present in each lane was calculated using standard imaging software.

5.3.5 Protein binding studies

The protein binding studies were performed using fluorescence quenching experiments in bovine serum albumin stock solution (BSA, 16.67 μM) in tris(hydroxymethyl)-aminomethane-HCl (15 mM)/NaCl (150 mM) buffer (pH adjusted to 7.5 with conc. HCl). The spectra were recorded at RT (313 K) with λ_{ex} = 296 nm and λ_{em} = 344 nm. The concentration of BSA was kept constant and the complex concentration was raised regularly. Synchronous fluorescence spectra of BSA in presence of complexes was also recorded using the same concentrations at two different Δλ values (difference between excitation and emission wavelengths of BSA) of 15 and 60 nm.

5.3.6 DNA binding studies

Absorption Studies. The DNA binding studies were performed in tris(hydroxymethyl)-aminomethane-HCl (15 mM)/NaCl (150 mM) buffer (pH adjusted to 7.5 with conc. HCl) using 1 mM solutions of complexes prepared in DMSO. The concentration of calf thymus-DNA (solution prepared in TRIS-HCl/NaCl buffer) was acquired from absorption intensity observed at 258 nm using molar extinction coefficient value of 6600 M^{-1}. The absorption titration experiments were performed with a fixed concentration of compounds (10 μM) and gradually increasing the concentration of DNA (0-48.84 μM) at RT (313 K). An equal amount of DNA was added to both the cuvettes, containing the test solution and the reference in order to eliminate the absorbance of DNA itself.

Ethidium Bromide Displacement Assay. For emission studies, a solution containing 36.73 μM DNA and 166.67 μM EB in TRIS-HCl/NaCl buffer was titrated by addition of complexes at RT (313 K). The influence of complexes on DNA-EB was recorded with λ_{ex} = 546 nm and λ_{em} = 610 nm, at a bandwidth of 2.5 nm.

5.3.7 Materials and Methods

All the chemicals were obtained from Sigma Aldrich and TCI and the solvents were obtained from SD Fine Chemicals, India and were used without any further purification.

5.3.7.1 NMR studies

NMR data was recorded on BRUKER AVANCE, 400 MHz spectrometer in $CDCl_3$, with TMS as internal standard. The ^{1}H and ^{13}C NMR spectra of all ligands can be found in Supplementary Data* at the end of the chapter.

5.3.7.2 FT-IR studies

FT-IR studies were performed on Bruker Alpha FT-IR spectrometer in solid state as KBr pellets. The FT-IR spectra of all ligands can be found in Supplementary Data* at the end of the chapter.

5.3.7.3 Single crystal X-ray studies

Diffraction data for all the ligands and complexes synthesized was collected on an Xcalibur, EOS, Gemini diffractometer with graphite monochromatic Mo Kα radiation (0.71073 Å). All structures were solved and refined using the Olex2[36] software and ShelXL[37] refinement package. Graphics were generated using MERCURY, version 4.3.1. All structures were solved by direct methods and refined in a regular pattern. In all the cases, non-hydrogen atoms were treated anisotropically. Whenever possible, the hydrogen atoms were refined by locating on a difference Fourier map.

5.3.7.4 Powder X-ray studies

Powder diffraction pattern of **C4** was recorded on an XPERT (Cu Kα radiation, λ = 1.54056 Å) diffractometer on a continuous scanning mode at 2θ value 5-90º.

5.3.7.5 Computational calculations

Gaussian16[38] was used to optimize the geometries of all the complexes **C1-C5**. Full geometry optimizations were carried out using the density functional theory (DFT) method at the B3LYP[39–42] level under LANL2DZ[43,44] basis set along with Gauss View visualization program.

5.3.7.6 Hirshfeld studies

The 3D Hirshfeld surfaces[45,46] and 2D fingerprint plots of the compounds were obtained using *CrystalExplorer* 3.1.[47,48]

5.3.7.7 UV-vis studies

UV-vis spectrophotometer was used to carry out studies of metal complexes and ligands, the DNA binding studies and SOD activity of the complexes. The spectrum was recorded using Perkin Elmer Lambda 35 dual beam UV-vis Spectrophotometer.

5.3.7.8 Fluorescence studies

Fluorescence spectra was recorded in solution phase on JASCO FP-6300 fluorescence spectrophotometer.

5.3.7.9 ESR studies

The ESR studies were performed in solution phase using DMSO (Methanol for **C1**) as solvent at room temperature and liquid nitrogen temperature on Bruker Biospin GmBH ESR instrument with a center field of 3200G, sweep width of 2000G and a microwave frequency in the range 9.447-9.454 GHz (JESR160 ESR JEOL instrument for **C1**).

5.3.7.10 ESI-MS studies

All the complexes were subjected to positive ion ESI-MS studies in solution phase using methanol as solvent on Waters Alliance E2695/HPLC-TQD Mass Spectrometer.

5.3.8 Analytical Data

The synthesized ligands were characterized using FT-IR, ^{1}H-NMR, ^{13}C-NMR and single crystal X-ray diffraction. All the compounds showed IR bands for C=O stretching around 1690-1640 cm^{-1}, two N-H stretching bands around 3300 cm^{-1}, 2900 cm^{-1} and N-H bending around 1550-1640 cm^{-1}, indicating the formation of amides.

Ligands -

L1 (N-(thiazol-2-yl) pivalamide). 2-aminothiazole was treated with pivaloyl chloride as mentioned in the procedure above and the compound was isolated. Single crystals were obtained from a (1:1) mixture of methanol and acetonitrile (Yield= 68%). M.P. (°C) = 110.

^{1}H NMR ($CDCl_3$/ppm): 9.874 (*s*, 1H, NH), 7.463 (*d*, 1H, CH), 6.994 (*d*, 1H, CH), 1.351 (*s*, 9H, 3(CH_3). ^{13}C NMR ($CDCl_3$/ppm): 176, 136, 128, 115, 39, 27.

FT-IR (KBr, ν/cm^{-1}): 3186, 2981, 1680, 1536, 1493, 1459, 1395, 1322, 1283, 1242, 1164, 1147, 1065, 921, 742.

L2 (N-(4-methylthiazol-2-yl)pivalamide). 2-amino-4-methylthiazole was treated with pivaloyl chloride as mentioned in the procedure above and the compound was isolated. Single crystals were obtained from a (1:1) mixture of methanol and acetonitrile (Yield= 68%). M.P. (°C) = 110.

^{1}H NMR ($CDCl_3$/ppm): 9.009 (*s*, 1H, NH), 6.530 (*s*, 1H, CH), 2.351 (*s*, 3H, CH_3), 1.330 (*s*, 9H, 3(CH_3). ^{13}C NMR ($CDCl_3$/ppm): 176, 146, 108, 39, 27, 16.

FT-IR (KBr, ν/cm^{-1}): 3268, 3116, 2969, 2743, 1657, 1531, 1476, 1399, 1371, 1311, 1289, 1159, 1007, 984, 922, 845, 818, 723, 669.

L3 (N-(5-methylthiazol-2-yl)pivalamide). The above process was repeated using 2-amino-5-methylthiazole. Single crystals were obtained from a mixture of (1:2) mixture of methanol and acetonitrile (Yield= 62%). M.P. (°C) = 128.

^{1}H NMR ($CDCl_3$/ppm): 9.065 (*s*, 1H, NH), 7.095 (*m*, 1H, CH), 2.417 (*s*, 3H, CH_3), 1.335 (*s*, 9H, 3(CH_3). ^{13}C NMR ($CDCl_3$/ppm): 176, 157, 134, 127, 39, 27.

FT-IR (KBr, ν/cm^{-1}): 3178, 3042, 2970, 2700, 1678, 1531, 1456, 1393, 1371, 1304, 1281, 1150, 1022, 993, 919, 852, 813, 776, 741, 697.

L4 (N-(benzothiazol-2-yl)pivalamide). The reaction was carried out in presence of 2-aminobenzthiazole (Yield= 66%). M.P. (°C) = 64.

^{1}H NMR ($CDCl_3$/ppm): 9.606 (*s*, 1H, NH), 7.857 (*d*, 1H, CH), 7.784 (*d*, 1H, CH), 7.486 (*m*, 1H, CH), 7.360 (*m*, 1H, CH), 1.388 (*s*, 9H, 3(CH_3). ^{13}C NMR ($CDCl_3$/ppm): 184, 177, 160, 146, 131, 126, 123, 121, 119, 39, 38, 27, 26.

FT-IR (KBr, ν/cm^{-1}): 3177, 2974, 2690, 2553, 2193, 1872, 1789, 1689, 1599, 1548, 1447, 1398, 1366, 1307, 1225, 1198, 1152, 1015, 946, 881, 820, 760, 684, 619, 529.

L5 (N-(benzoimidazol-2-yl)pivalamide). The same procedure was carried out using 2-aminobenzimidazole. The single crystals were obtained from a (1:1) mixture of ethyl acetate and methanol (Yield= 69%). M.P. (°C) = 244.

^{1}H NMR ($CDCl_3$/ppm): 9.395 (*s*, 1H, NH), 7.559 (*m*, 2H, 2(CH)), 7.489 (m, 2H, 2(CH)), 1.352 (*s*, 9H, 3(CH_3). ^{13}C NMR ($CDCl_3$/ppm): 179, 147, 122, 39, 27.

FT-IR (KBr, ν/cm^{-1}): 3378, 3057, 2969, 1685, 1629, 1559, 1515, 1457, 1407, 1367, 1309, 1272, 1222, 1151, 1116, 1021, 938, 864, 827, 741, 710, 618.

Complexes - In the mass spectra of **C1, C3** and **C4** complexes, molecular ion peaks corresponding to $[CuL]^+$ have been obtained. In **C5**, a peak corresponding to $[CuL_2]+H^+$ has been observed.

C1 or (Cu(L1)$_2$ (Cu(N-(thiazol-2-yl)pivalamide)$_2$). The single crystals were obtained from a mixture of methanol and acetonitrile (Yield=72%).

FT-IR (KBr, ν/cm^{-1}): 3358, 3134, 3090, 2956, 1760, 1633, 1518, 1473, 1452, 1358, 1318, 1245, 1185, 1159, 925, 870, 774, 757, 707, 643, 618, 527, 494, 455.

ESI-MS (*m/z*): 185, 247 (Cu(II)+ **L1**), 249.

C3 or (Cu(L3)$_2$) (Cu(N-(5-methylthiazol-2-yl)pivalamide)$_2$). The single crystals were obtained from a (1:1) mixture of methanol and ethanol (Yield=70%).

FT-IR (KBr, ν/cm^{-1}): 3433, 3098, 2955, 2922, 2373, 1672, 1480, 1460, 1355, 1243, 1148, 917, 840, 757, 627, 564, 529, 479.

ESI-MS (*m/z*): 199, 261 (Cu(II)+ **L3**), 263.

C4 or (Cu(L4)$_2$) (Cu(N-(benzothiazol-2-yl)pivalamide)$_2$) Yield=69%. FT-IR (KBr, ν/cm^{-1}): 3433, 3290, 3141, 3065, 2960, 2869, 2748, 1634, 1560, 1481, 1457, 1417, 1337, 1224, 1132, 1021, 759, 722, 621.

ESI-MS (*m/z*): 235, 297 (Cu(II)+ **L4**), 299.

C5 or (Cu(L5)$_2$) (Cu(N-(benzoimidazol-2-yl)pivalamide)$_2$) The single crystals were obtained from ethanol containing few drops of acetonitrile (Yield=71%).

FT-IR (KBr, ν/cm^{-1}): 3406, 3182, 3068, 2802, 1622, 1549, 1490, 1361, 1318, 1277, 1219, 1151, 1062, 1029, 945, 916, 821, 782, 743, 637, 562, 470, 451s.

ESI-MS (*m/z*): 218, 497 (Cu(II)+ 2**L5**), 499.

5.4 RESULTS AND DISCUSSION

5.4.1 UV studies of metal complexes

The electronic spectra of all the complexes and their respective ligands were recorded in methanol at room temperature and we observe absorption peaks in all compounds between 300-350 nm corresponding to *n*-π* transition and a peak between 500-900 nm corresponding to the ligand field transition indicating the formation of copper(II) complex. The charge transfer transition has been observed as a shoulder between 350-450 nm (Figure 5.3).

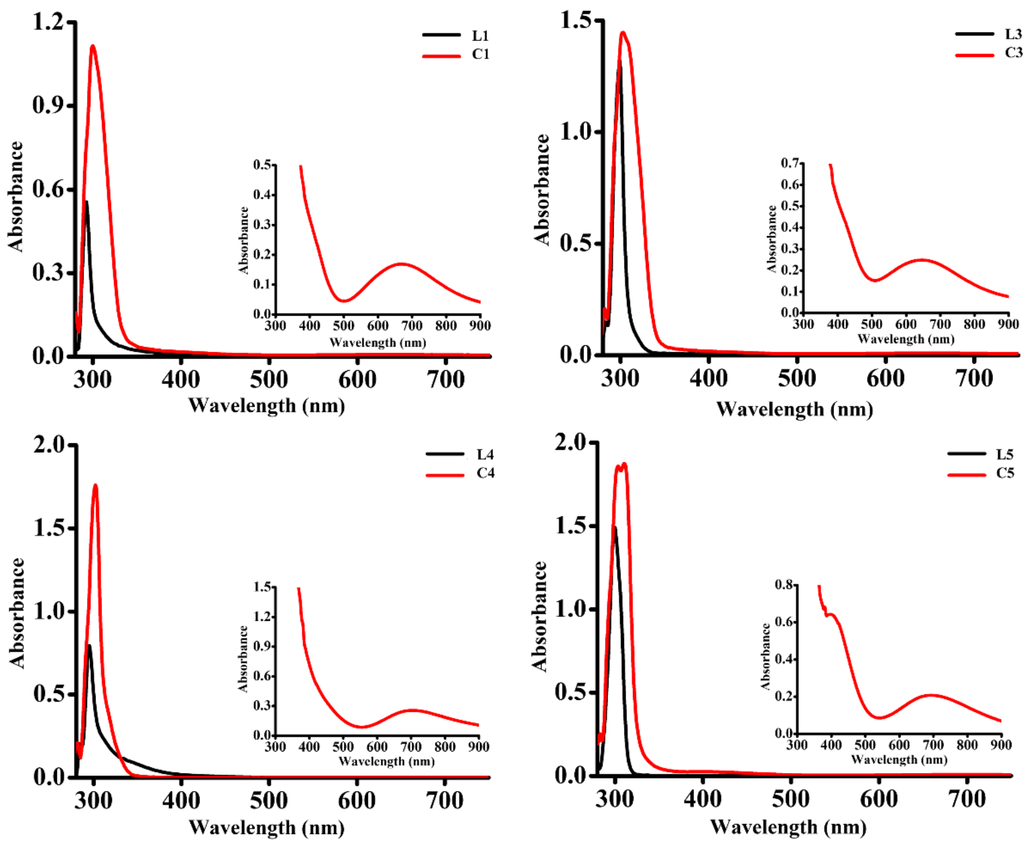

Figure 5.3 UV-vis spectra of ligands and their respective complexes

5.4.2 ESR analysis

Table 5.1 g and A values for all complexes, obtained from ESR data

Complex	g values
C1	$g_z = 2.28$, $g_x = 2.08$, $g_y = 2.05$, $A_z = 179 \times 10^{-4}\ cm^{-1}$; $A_x = 6.07 \times 10^{-4}\ cm^{-1}$, $A_y = 5.98 \times 10^{-4}\ cm^{-1}$
C3	$g_{II} = 2.2$, $g_{\perp} = 2.062$
C4	$g_{II} = 2.3$, $g_{\perp} = 2.05$, $A_{II} = 161 \times 10^{-4}\ cm^{-1}$
C5	$g_{II} = 2.2$, $g_{\perp} = 2.1$

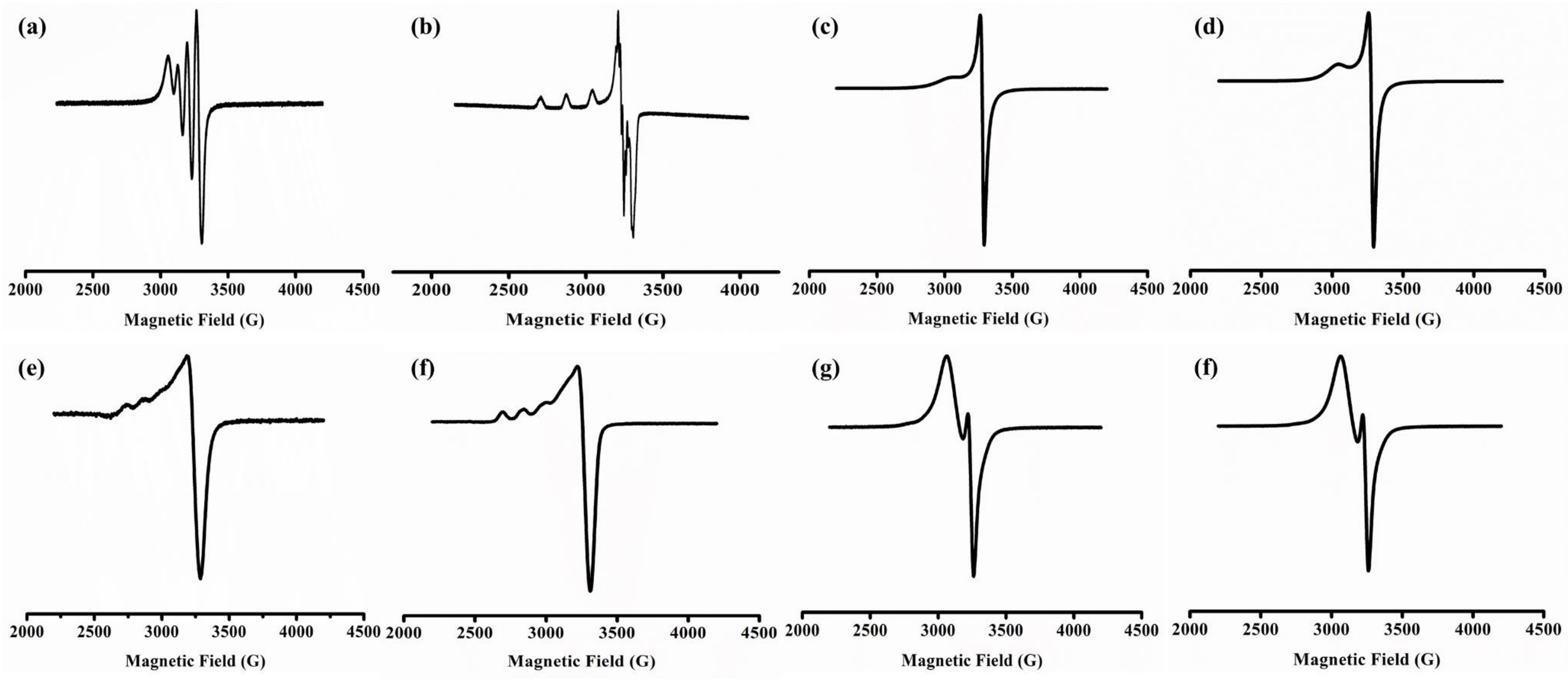

Figure 5.4 X-band ESR spectrum for (a) C1, RT (methanol) (b) C1, LNT (methanol) (c) C3, RT (DMSO) (d) C3, LNT (DMSO) (e) C4, RT (DMSO) (f) C4, LNT (DMSO) (g) C5, RT (DMSO) (h) C5, LNT (DMSO)

The X-band ESR spectra of all complexes was recorded in solution state with DMSO as solvent (Methanol for **C1**) at room temperature (RT) and liquid nitrogen temperature (LNT) (Figure 5.4). The spectra recorded at RT and LNT were found to be identical. Complex **C1** exhibits anisotropic ESR while **C3**, **C4** and **C5** exhibit axial ESR. Hyperfine splitting characteristic of normal copper(II) complexes has been observed in **C1** and **C4**. The observed g and A values have been presented in Table 5.1. The observed A_{II} values between 160-180 x 10^{-4} cm^{-1} support N_2O_2 coordination.

5.4.3 Crystallography

The ligands and complexes were characterized using single crystal X-ray diffraction studies. Crystallographic parameters and H-bond parameters of all the crystal structures have been tabulated in Tables S5.1* and S5.2* respectively. Unfortunately, single crystals for **L4** and **C4** could not be obtained, hence powder XRD spectrum for complex **C4** was recorded (Figure S5.2*).

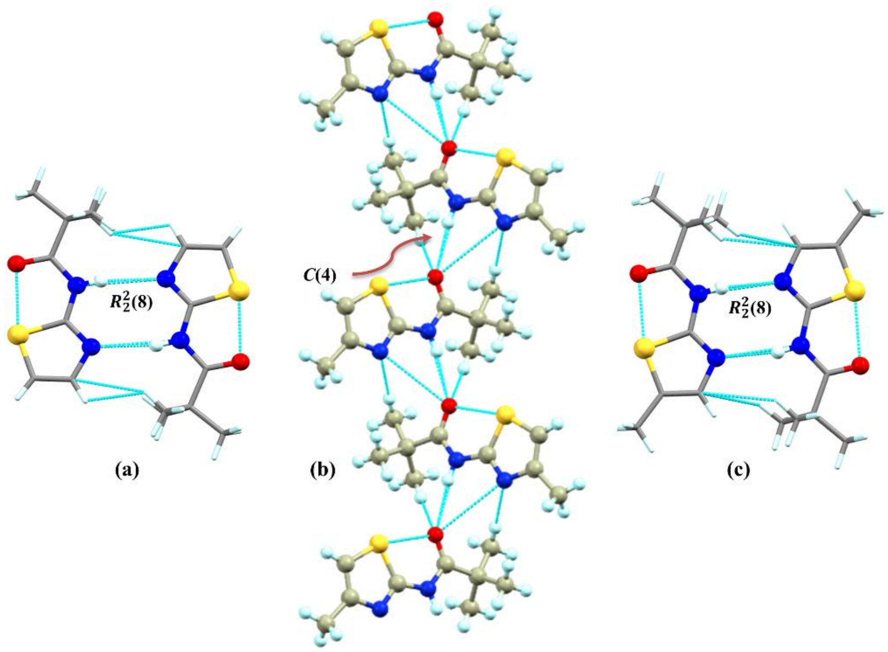

Figure 5.5 Zero dimensional hydrogen bonded networks present in (a) Ligand L1 and (c) Ligand L3 as a result of N-H…N, C-H…C and S…O interactions (b) 1D network formed in compound L2, as viewed from *a* axis

L1 [*N-(thiazol-2-yl) pivalamide]* The single crystals of **L1** were obtained from a mixture of methanol and acetonitrile at RT. **L1** crystallizes out in monoclinic, *$P2_1/c$*

space group. We find a synthon of the type $R_2^2(8)$ in the structure composed of N-H…N (bond length= 2.26 Å) type interactions (Figure 5.5 (a)) as shown in Scheme 5.1(Type A). We also find intramolecular S…O interactions with a bond length of 2.63 Å and various other van der Waals interactions in the crystal structure.

L2 [*N-(4-methylthiazol-2-yl)pivalamide]* Crystals of ligand **L2** were obtained from a mixture of methanol and ethanol. The structure crystallizes out in monoclinic, *P2₁/c* space group and showcases a one-dimensional assembly, unlike other thiazole-based pivalamides where we obtained a zero-dimensional closed network. The network is formed as a result of N-H…O interactions (bond length= 2.21 Å) forming a ***C(4)*** type graph set. We also found several interactions like C-H…N (bond length= 2.67 Å), C-H…O (bond length= 2.58 Å), S…O (bond length= 2.73 Å) in the network. (Figure 5.5 (b))

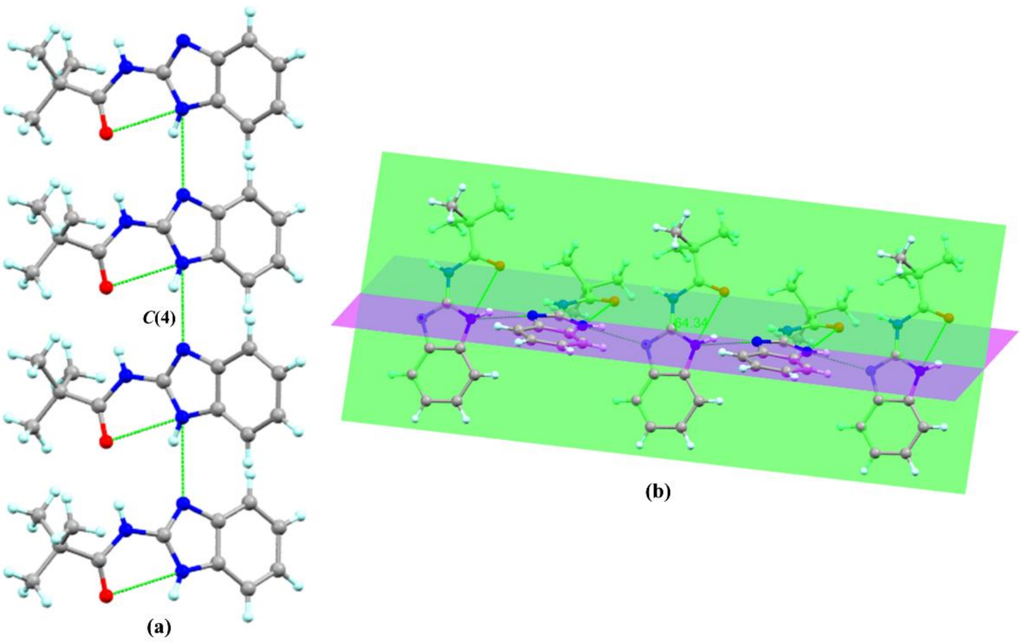

Figure 5.6 (a) Ligand L5 as viewed from a axis, (b) angle between the planes formed between two adjacent molecules

L3 [*N-(5-methylthiazol-2-yl)pivalamide]* Crystals of ligand **L3** were obtained from methanol and acetonitrile. The compound crystallizes out in orthorhombic *Pbca* space group. The supramolecular arrangement of **2** (Figure 5.5 (c)) is similar to that found in compound **L1** (S…O bond length= 2.64 Å and N-H…N bond length=2.25 Å) as illustrated by Type A(Scheme 1). We also find a number of van der Waals contacts, C-H…O interactions, etc. in the crystal structure.

L5 [*N-(benzoimidazol-2-yl)pivalamide]* The single crystals of compound **L5** obtained from methanol and ethyl acetate mixture crystallize out in orthorhombic, *Pca2₁* space group. The structure showcases a unique closed ring type synthon comprising of N-H…O (bond length= 2.6 Å) and N-H…N (bond length= 2.11 Å) interactions (Figure 5.6). The angle between the planes of two adjacent molecules was found to be 59.65°. Besides, N…O (bond length= Å) type interactions and various van der Waals interactions were also found to be present.

All the single crystal structures of complexes are evident of a nearly square planar geometry formed by a coordination of 2 oxygen and 2 nitrogen atoms of the heterocyclic ligands in *trans* fashion.

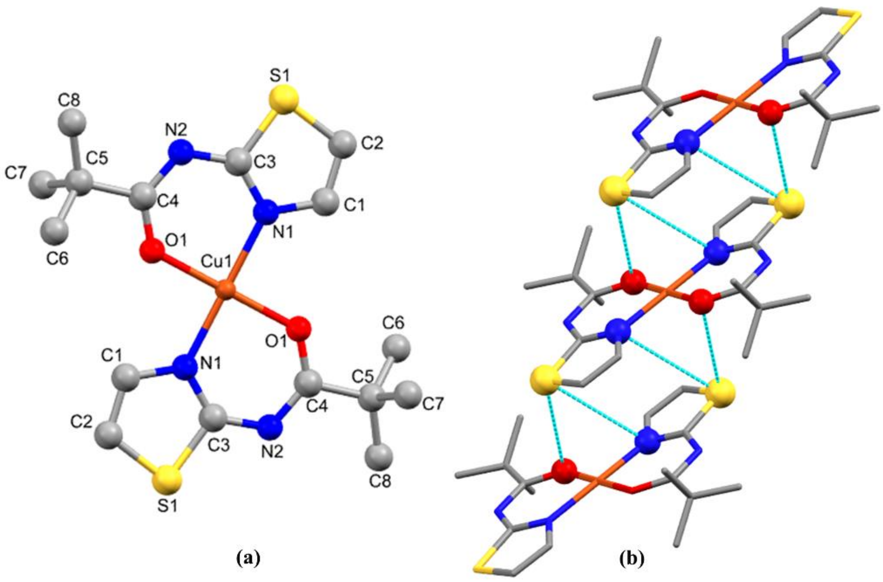

Figure 5.7 (a) asymmetric unit of complex C1, (b) non-covalent interactions present in the crystal structure (H atoms are not shown for clarity of image)

C1 [*Cu(N-(thiazol-2-yl)pivalamide)₂]* The single crystals of **C1** were obtained from a mixture of methanol and acetonitrile at RT. The complex crystallizes out in triclinic *P-1* space group and possesses a near square planar geometry (adjacent bond angles= 90.75°, 89.25°) (Figure 5.7). Two oxygen atoms of amide group and two nitrogen atoms of the thiazole rings form coordinate bonds with the copper atom in +2 oxidation state. We find a unique synthon comprising of S…O (bond length= 3.6 Å) and S…N (3.7 Å) interactions, extending in 2D. Other non-covalent interactions include the C-H…N interactions which extends the structure in 3D.

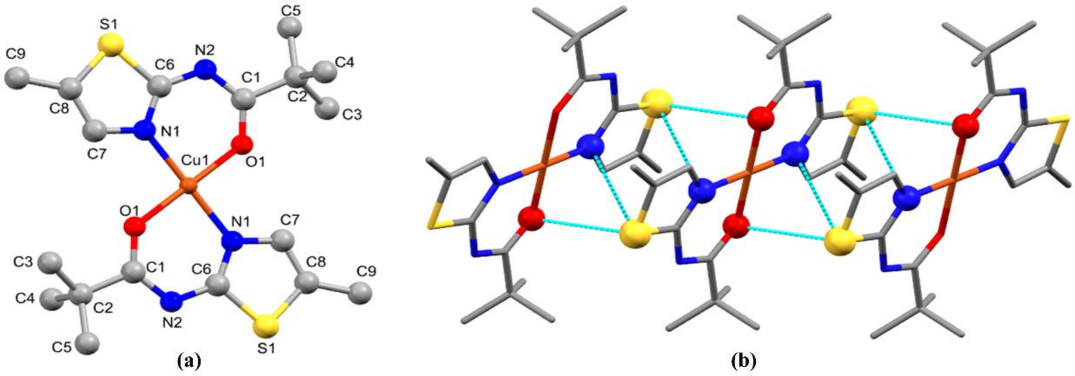

Figure 5.8 (a) asymmetric unit of complex C3, (b) S…O and S…N interactions present in the complex C2 (H atoms are not shown for clarity of image)

C3 ***[Cu(N-(5-methylthiazol-2-yl)pivalamide)$_2$]*** Complex **C3** crystallized out in the form of green needle like crystals from a mixture of methanol and ethanol. The crystal belongs to monoclinic *P2$_1$/c* space group and possesses a similar near square planar geometry as in **C1** (adjacent bond angles= 89.68^{o}, 90.32^{o}) (Figure 5.8(a)). The donor atoms are also similar as in complex **C1** and we find the same synthon as in **C1** having S…O (bond length= 3.56 Å) and S…N (bond length= 3.81 Å) interactions (Figure 5.8(b)). We don't find any other non-covalent interactions in the crystal structure.

C5 ***[Cu(N-(benzoimidazol-2-yl)pivalamide)$_2$]*** **C5** crystals were obtained from a mixture of ethanol and acetonitrile at RT. The complex crystallizes out in monoclinic *P2$_1$/n* space group. The geometry of the complex is distorted square planar (Figure 5.9) and the donor atoms are the same as in above mentioned complexes. The complex comprises of H-bonded synthon of type $\boldsymbol{R_2^2(8)}$ which extends in 1D and many other N-H…C, C-H…π, van der Waals interactions, etc.

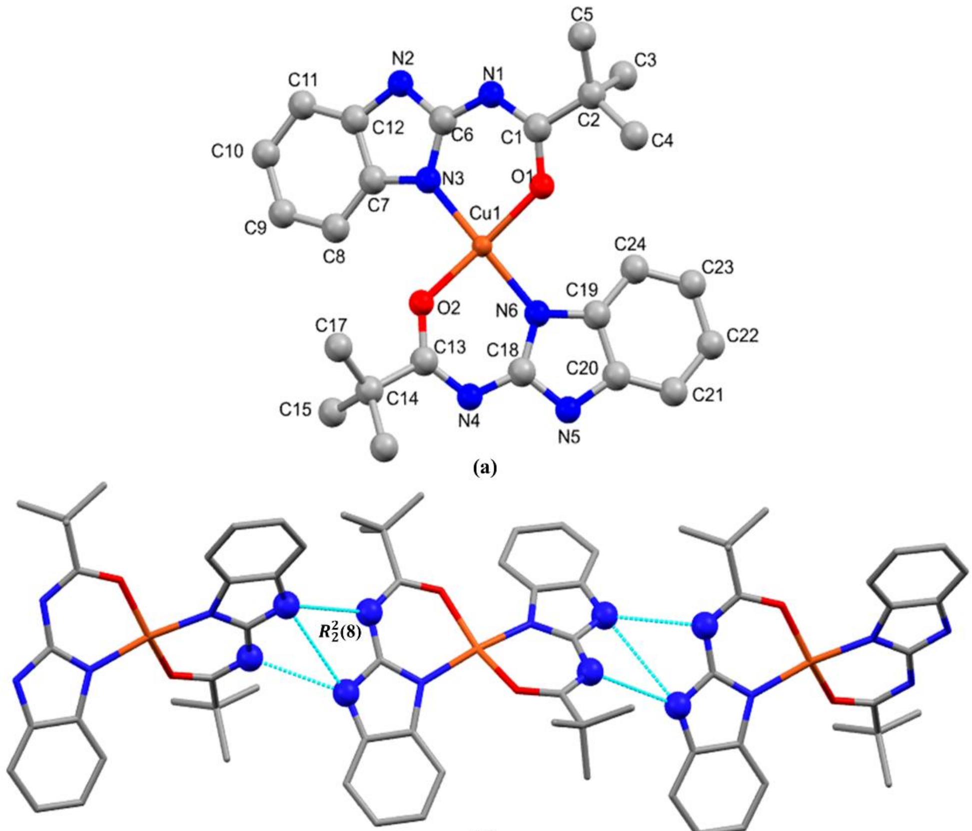

Figure 5.9 (a) asymmetric unit of C4, (b) Intermolecular H-bonding interactions found in the structure (H atoms are not shown for clarity of image)

Single crystals suitable for diffraction study of **C4** could not be obtained, hence, powder X-ray studies were performed for **C4**. Major peaks were observed at 2θ values 5.7, 9.9, 10.3, 12.5, 13.2, 14.1, 14.9, 20.9, 22.2 and 25.3 (Figure S5.2*).

5.4.4 Hirshfeld studies

The ligands (**L1, L2, L3, L5**) and copper (II) complexes (**C1, C3, C5**) were subjected to Hirshfeld analyses in order to quantify and compare the non-covalent interactions prevalent in the structures. The 2D fingerprint plots of all the ligands show multiple spikes corresponding to H…C (d_i=1.1, d_e=1.7), H…N (d_i= 0.9, d_e= 1.3), H…O (d_i= 0.9, d_e= 1.2), H…H (d_i= 1.1, d_e= 1.1), N…H (d_i= 1.3, d_e= 0.9), O…H (d_i= 0.9, d_e= 1.2) and C…H (d_i= 1.7, d_e= 1.2) interactions (Figures 5.10, 5.11).

We also find a small amount of S…H, S…O and S…S interactions in the thiazole-based ligands, which are validated from single crystal studies also. The metal complexes exhibit a more diverse cluster of non-covalent interactions which include some rare interactions like C…N, Cu…S, Cu…H, Cu…C and many more.

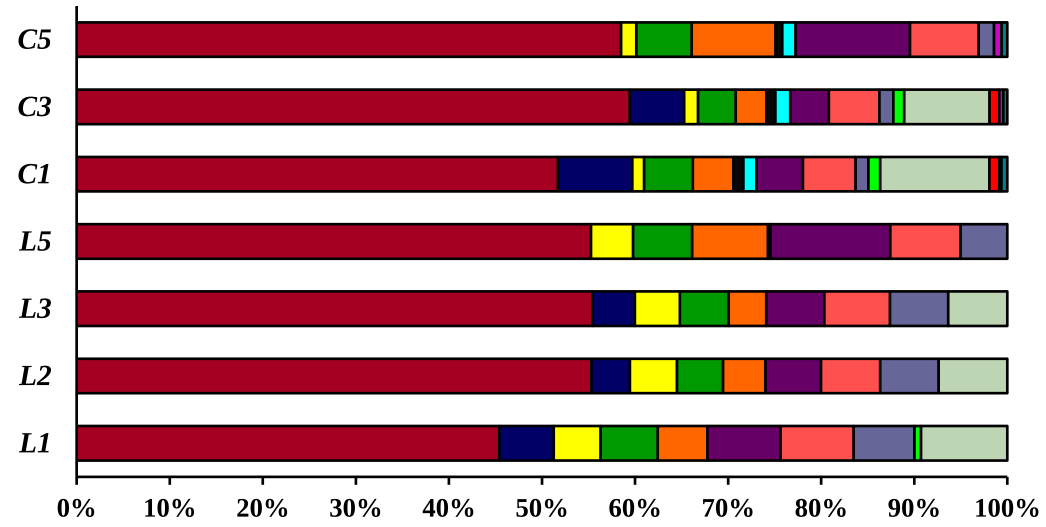

	L1	L2	L3	L5	C1	C3	C5
H-H	45.1	54.7	55	55	48.5	55.8	57.1
H-S	5.8	4.1	4.5	0	7.5	5.5	0
H-O	5	5	4.8	4.5	1.2	1.4	1.6
H-N	6.1	4.9	5.2	6.3	4.9	3.8	5.8
H-C	5.3	4.5	4	8.1	4.1	3.1	8.8
C-N	0	0	0	0.2	1	0.9	0.7
C-C	0	0	0	0.1	1.3	1.5	1.4
C-H	7.8	5.9	6.2	12.8	4.7	3.9	12
N-H	7.8	6.3	7	7.5	5.3	5.1	7.2
O-H	6.5	6.2	6.2	5	1.3	1.4	1.6
S-O	0.7	0	0	0	1.2	1.1	0
S-H	9.2	7.3	6.3	0	11	8.6	0
Cu-S	0	0	0	0	1	1	0
Cu-H	0	0	0	0	0.2	0.4	0.8
Cu-C	0	0	0	0	0.6	0.4	0.6

Figure 5.10 Intermolecular interactions calculated from Hirshfeld studies

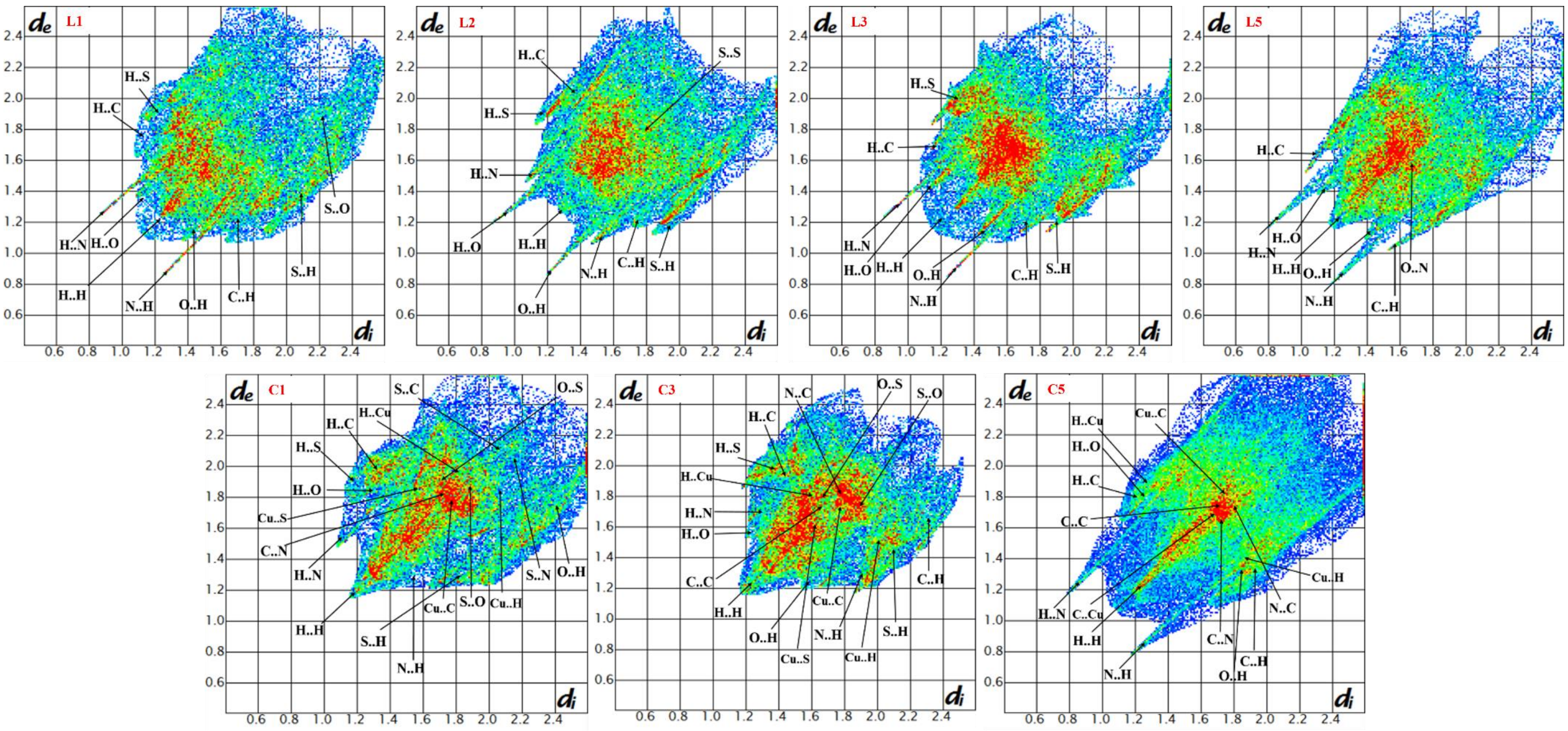

Figure 5.11 Two-Dimensional Hirshfeld fingerprint plots of ligands and complexes. The color in the sequence white-blue-green-red is a summary of the frequencies of each combination of distances d_e and d_i across the Hirshfeld surfaces of a molecule (in increasing order), where d_i is internal distance and d_e external distance from the Hirshfeld surface to the nearest molecule

5.4.5 Computational studies

The theoretical calculations were obtained for all complexes. The bond parameters of optimized geometries (Figure 5.12) are in agreement with those obtained from single crystal studies.

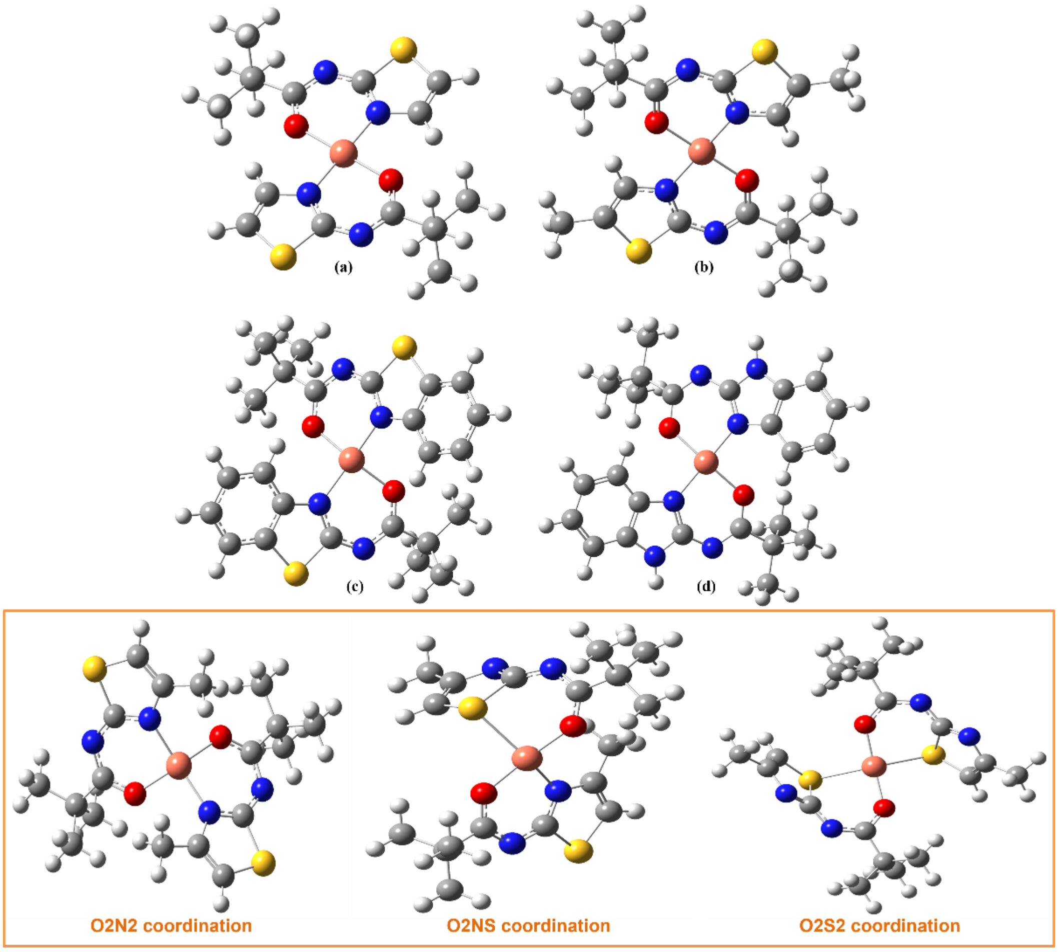

Figure 5.12 Optimized geometries of (a) C1. (b) C3, (c) C4 and (d) C5 and various coordination modes of complex C2, which could not be isolated in free form

The geometry of complex **C2**, which could not be isolated in free form was investigated using computational studies. A plausible reason could be the methyl-methyl repulsions between the tert-butyl group of one ligand and the methyl group on thiazole ring of another. In that regard, since all the metal complexes in this series were formed with O2N2 coordination, this complex too, was supposed to be following the trend. But since the two methyl groups come very close in this geometry (Figure 5.12), their repulsion prevented the formation of coordination complex. O2NS and O2S2 coordination calculations gave complexes with unusual geometries which do not seem likely to be isolated. Also, since sulphur atom is a weaker base than oxygen and nitrogen, it is less likely to form a coordination bond with copper atom in presence of the latter two. Nevertheless, the energies obtained for **C2** from the computational experiments were found to be very close to the complexes formed and we could not make any solid conclusions regarding our hypothesis.

Table 5.2 HOMO-LUMO energies obtained from computational studies

	E (kJ/mol)	HOMO	LUMO	ΔE (eV)
C1	-3.17 x 10^6	-6.2123	-1.7385	4.4738
C2	-3.44 x 10^6	-	-	-
C3	-3.37 x 10^6	-5.9903	-1.5657	4.4246
C4	-3.98 x 10^6	-6.2243	-1.8506	4.3737
C5	-3.38 x 10^6	-5.8738	-1.1965	4.6773

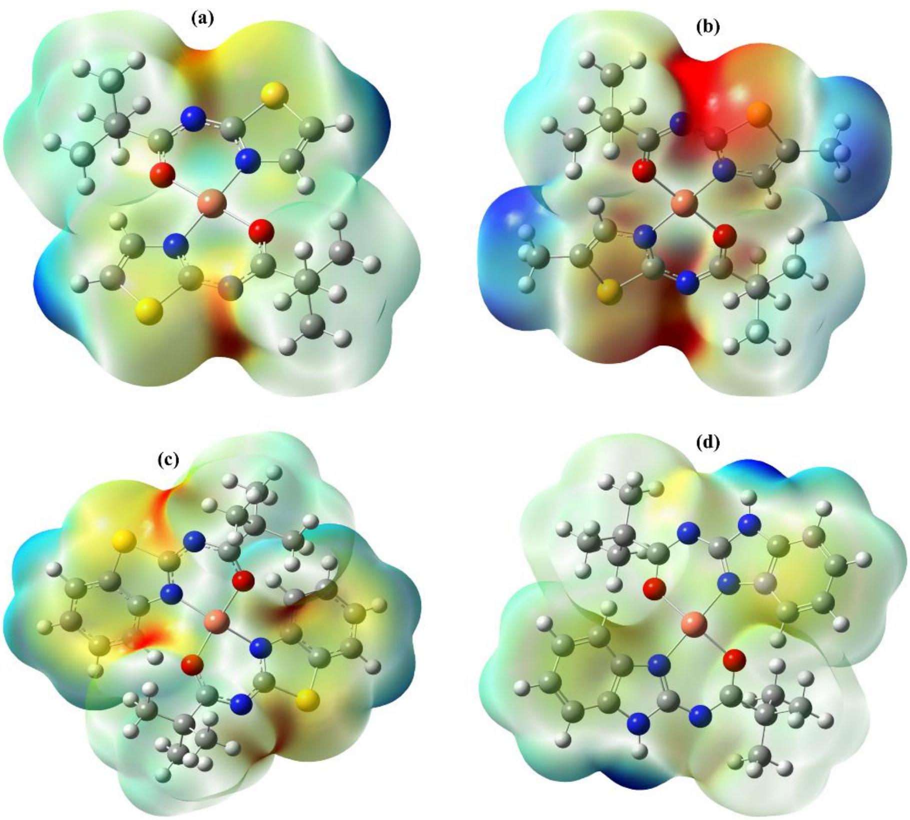

Figure 5.13 MESP plots for (a) C1, (b) C3, (c) C4 and (d) C5

The MESP plots are evident of a positive density around the copper atom and negative densities around the subsequent donor atoms of the ligands (Figure 5.13). As can be seen from plot, there is complete delocalization of π-electron density on the part of the ligand which is involved in coordination with the metal ion, which can facilitate the redox.

The energy gaps between HOMO (highest occupied molecular orbital) and LUMO (lowest unoccupied molecular orbital) were found to be 4.47, 4.42, 4.37 and 4.67 eV for complexes **C1**, **C3**, **C4** and **C5** respectively (Figure 5.14 Table 5.2). This order approximately matches with the order of SOD mimic activity of the complexes.

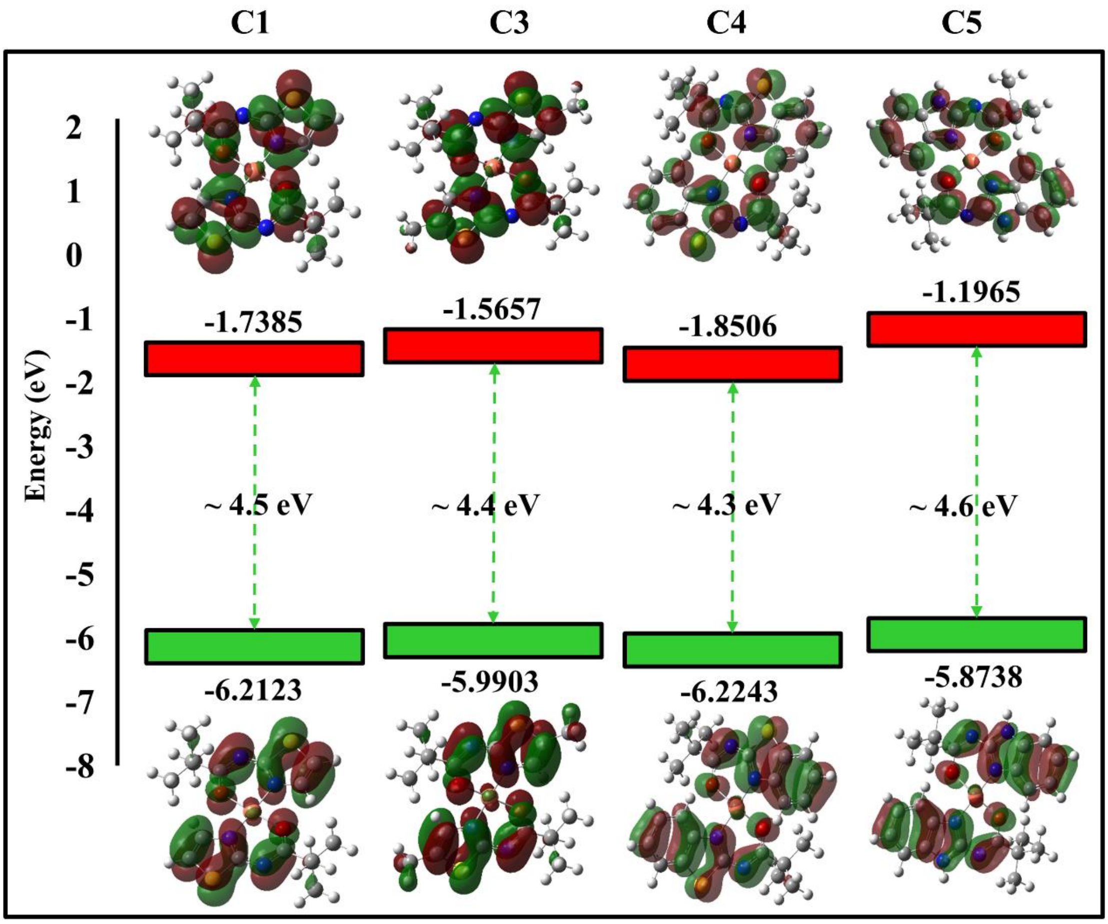

Figure 5.14 HOMO-LUMO band gap in the complexes formed

5.4.6 Superoxide dismutase activity

Copper(II) systems are known to show excellent superoxide dismutase activity. The complexes reported here have been found to be active SOD mimics, being able to scavenge the superoxide at low concentrations. It is remarkable to note that the IC_{50} values for the complexes fall in the range of 0.28-1.21 μM, in the order, **C3 < C4 < C1 < C5**.

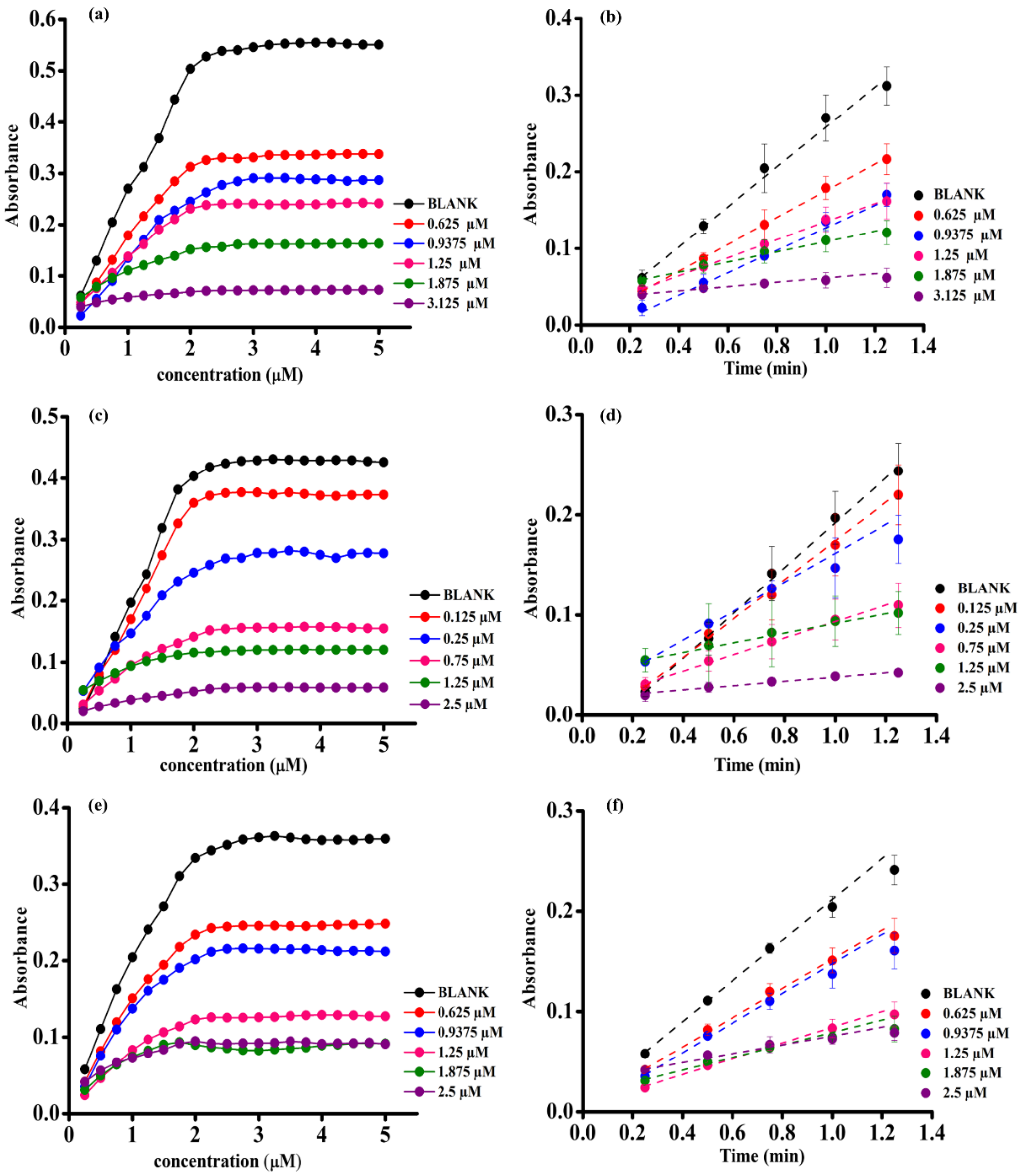

Figure 5.15 Plots of absorbance recorded at 560.0 nm at an interval of 15sec for different concentrations of complex (a) C1, (b) C3 and (c) C4 IC_{50} for C1= 1.062 μM, C3= 0.285 μM, C4= 0.794 μM

The values are listed in Table 5.3, along with those of native Cu-Zn SOD and certain selected compounds from the literature. We can infer that the synthesized complexes are more efficient than Vitamin C, $CuSO_4$, $Cu(en)_2$ and number of previously reported SOD mimics in literature.

A lower value of **C3** (Figure 5.16) may be attributed to the presence of electron donating methyl group present on the thiazole ring, causing an increased basicity of the nitrogen atom, which might be easing the access of superoxide anion to the copper center. This proves that even the slightest changes in ligand design and coordination environment of a complex can substantially affect their activity. Similar experiments when carried out to assess the activity of ligands failed to provide any positive results, which suggests that the ligands essentially remained SOD silent (Figure S5.1*).

Table 5.3 IC_{50} values for the synthesized complexes and similar Cu complexes reported in literature

Complex	IC_{50} (μM)	Reference
C1 [a]	**1.062**	This work
C3 [a]	**0.285**	
C4 [a]	**0.794**	
C5 [a]	**1.213**	
Native Cu-Zn SOD [b]	0.03-0.15	49,50
Vitamin C [a]	852	51
$Cu(en)_2Cl$ [a]	1000	49
$CuCl_2.2H_2O$ [b]	0.910	52
$CuSO_4$ [b]	30.0	53
$[Cu_2(indo)_4(H_2O)_2]$ [c]	1.31	53
Cu(II) salan complexes [b]	0.75-3.0	54
[Cu(sal)(phen)] [b]	1.01	53

(IC_{50} was determined by a= inhibition of NBT, b= xanthine/xanthine oxidase, c= alkaline DMSO)

A decreased Lewis acidity of **C1** could cause a reduced reactivity with superoxide ion and hence lower activity.[54] There is a report of similar instance of nitrogen basicity leading to substantial changes in SOD activity. But given the fact that structure of complexes **C1** and **C3** vary only by the presence of a methyl group, and **C4** and **C5** vary by the heteroatom (N or S), the IC_{50} values of **C4** and **C5** are fairly closer than those of **C1** and **C3**. This also indicates that thiazole-based complexes have a better SOD activity than those with imidazole-based backbones.

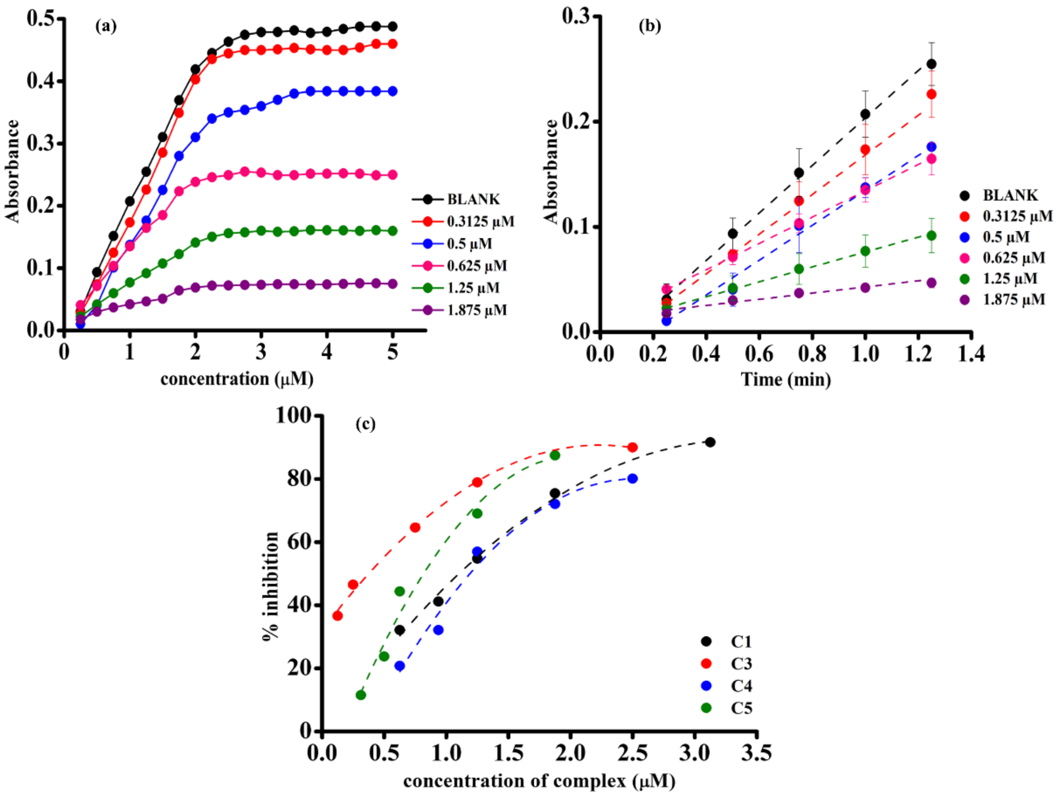

Figure 5.16 Plots of (a) Absorbance recorded at 560.0 nm at an interval of 15sec for different concentrations of complex C5 and (b) %inhibition plots of all complexes at various concentrations (μM); IC_{50} for C5= 1.213 μM

5.4.7 DNA cleavage studies

The DNA cleavage studies were performed to assess the interaction of the complexes with supercoiled plasmid DNA. For the purpose, gel electrophoresis was employed to visualize different forms of plasmid DNA, namely supercoiled form (Form I), nicked form (Form II, obtained after one of the DNA strands is cleaved) and linear form (Form III, obtained after both the strands are broken). This way, Form I migrates faster than any other form, and nicked form (Form II), which is the bulkiest, migrates with least velocity.[55–57] The efficacy of the ligands and the complexes was examined for the cleavage of plasmid DNA using gel electrophoresis (Figure 5.17). The complex **C3** was employed for the initial studies where different concentrations were assessed starting with the smallest concentration of complex (1-25 μM) (Figure 5.17(a)). It was found that the intensity of Form II and Form III bands increased with increasing concentration of **C3**.

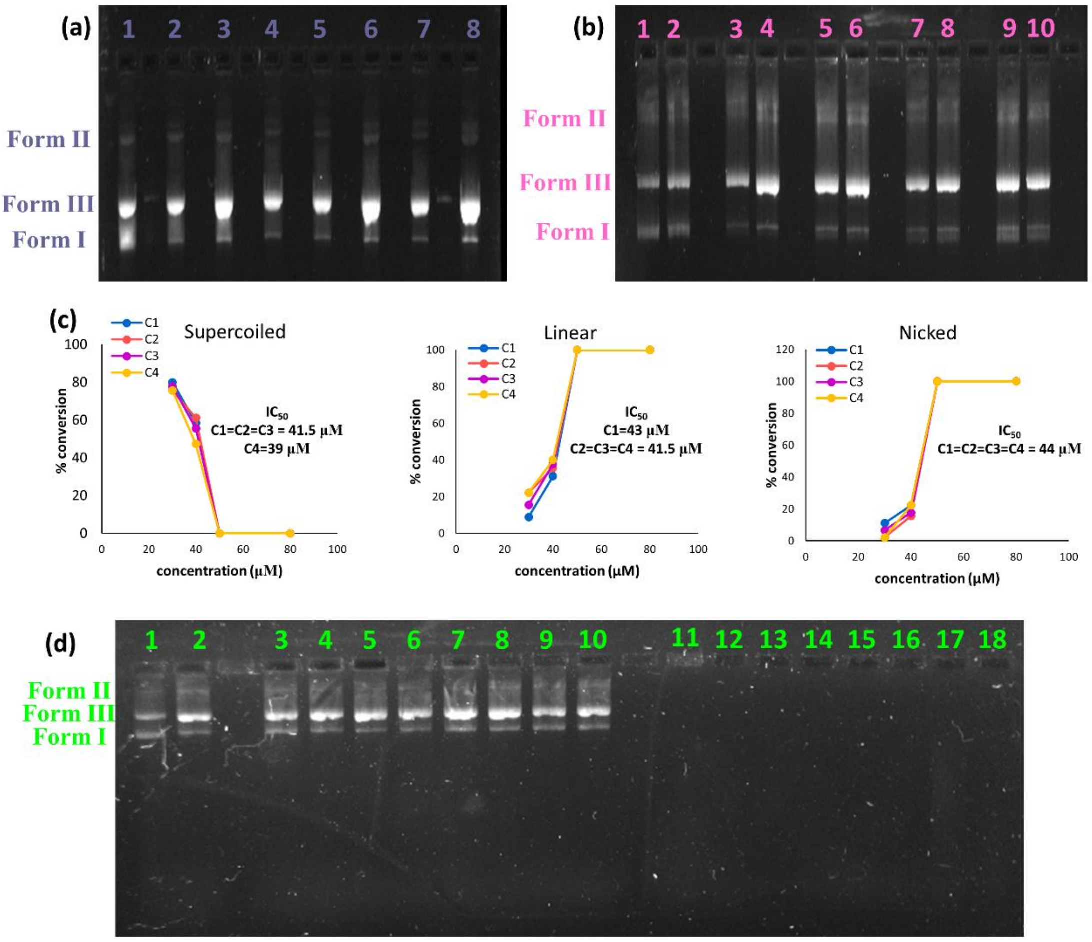

Figure 5.17 Cleavage of supercoiled DNA (0.1 µg/µL) with different concentrations of ligands and complexes in the presence of 10 mM H_2O_2 after 1 h incubation at 30 °C in Tris-HCl/NaCl buffer (pH = 7.2). (a) Lane 1: DNA control; lane 2: DNA + H_2O_2 (10 mM); Lanes 3–8: DNA + H_2O_2 (10 mM) + complex C3 (1 µM, 5 µM, 10 µM, 15 µM, 20 µM, 25 µM respectively; (b) Lane 1: DNA control; lane 2: DNA + H_2O_2 (10 mM); Lanes 3–10: DNA + H_2O_2 (10 mM) + complexes (C1 (30 µM), C1 (40 µM), C3 (30 µM), C3 (40 µM), C4 (30 µM), C4 (40 µM), C5 (30 µM), C5 (40 µM)) respectively; (c)%conversion of individual forms of DNA in all complexes and their respective IC_{50} values, calculated from bands obtained in experiment (b) and (d); (d) Lane 1: DNA control; lane 2: DNA + H_2O_2 (10 mM); lanes 3–10: DNA + H_2O_2 (10 mM) + ligands (L1 (50 µM), L1 (80 µM), L3 (50 µM), L3 (80 µM), L4 (50 µM), L4 (80 µM), L5 (50 µM), L5 (80 µM)), lanes 11–18: DNA + H_2O_2 (10 mM) + complexes (C1 (50 µM), C1 (80 µM), C3 (50 µM), C3 (80 µM), C4 (50 µM), C4 (80 µM), C5 (50 µM), C5 (80 µM)) respectively.

Similar experiments were then performed using higher concentration of all complexes (30, 40, 50, 80 µM) (Figure 5.17(b), (d)). In presence of peroxide, it was observed that the complexes could cleave supercoiled (Form I) DNA into subsequent Forms II and III. No bands of supercoiled, nicked or linear form of DNA were observed in higher concentrations, which shows that all the complexes could fully cleave all the DNA present in the system.

The IC_{50} values were calculated for all complexes indicating the concentration which facilitated 50% conversion of plasmid DNA. The values for all the three forms fall in the range of 40-45 μM (Table 5.4). Since all the cleavage studies were performed in presence of peroxide, we believe that the reaction between the metal ions and peroxide might be generating diffusible hydroxyl radicals or molecular oxygen, which might be involved in Fenton type reaction[58] and thereby showing strong DNA cleavage activity.

Table 5.4 IC_{50} values obtained from the cleavage studies

Complex	IC_{50} (μM)		
	Form I	Form II	Form III
C1	**41.5**	**43**	**44**
C3	**41.5**	**41.5**	**44**
C4	**41.5**	**41.5**	**44**
C5	**39**	**41.5**	**44**

5.4.8 BSA binding studies

The BSA binding ability of any molecule can be assessed by fluorescence spectral titration technique. A quenching in the fluorescence intensity of BSA (along with a blue shift) upon addition of any compound is associated with conformational and dynamic changes in the protein structure.[59] The fluorescence of BSA is caused due to the presence of tryptophan (Trp) and tyrosine (Tyr) residues in its structure. The intensity decreases with increasing concentrations of all the complexes as shown in Figure 5.18. Emission spectra for all ligands was also recorded in presence of BSA and can be found in Supplementary Data, Figure S5.3*. All the parameters are listed in Table 5.5.

The fluorescence quenching constant/ Stern-Volmer constant K_{SV} was calculated using the Stern-Volmer equation (equation 5.2)[60]:

$$I_0 / I = 1 + K_{SV} [Q] \qquad - (5.2)$$

where I_0 and I are the fluorescence emission intensities in the absence and presence of a quencher (complex) respectively and [Q] is the concentration of quencher; K_{SV} was obtained from the slope of the plot of I_0/I vs. [Q] (Figures 5.18(f), S5.3*).

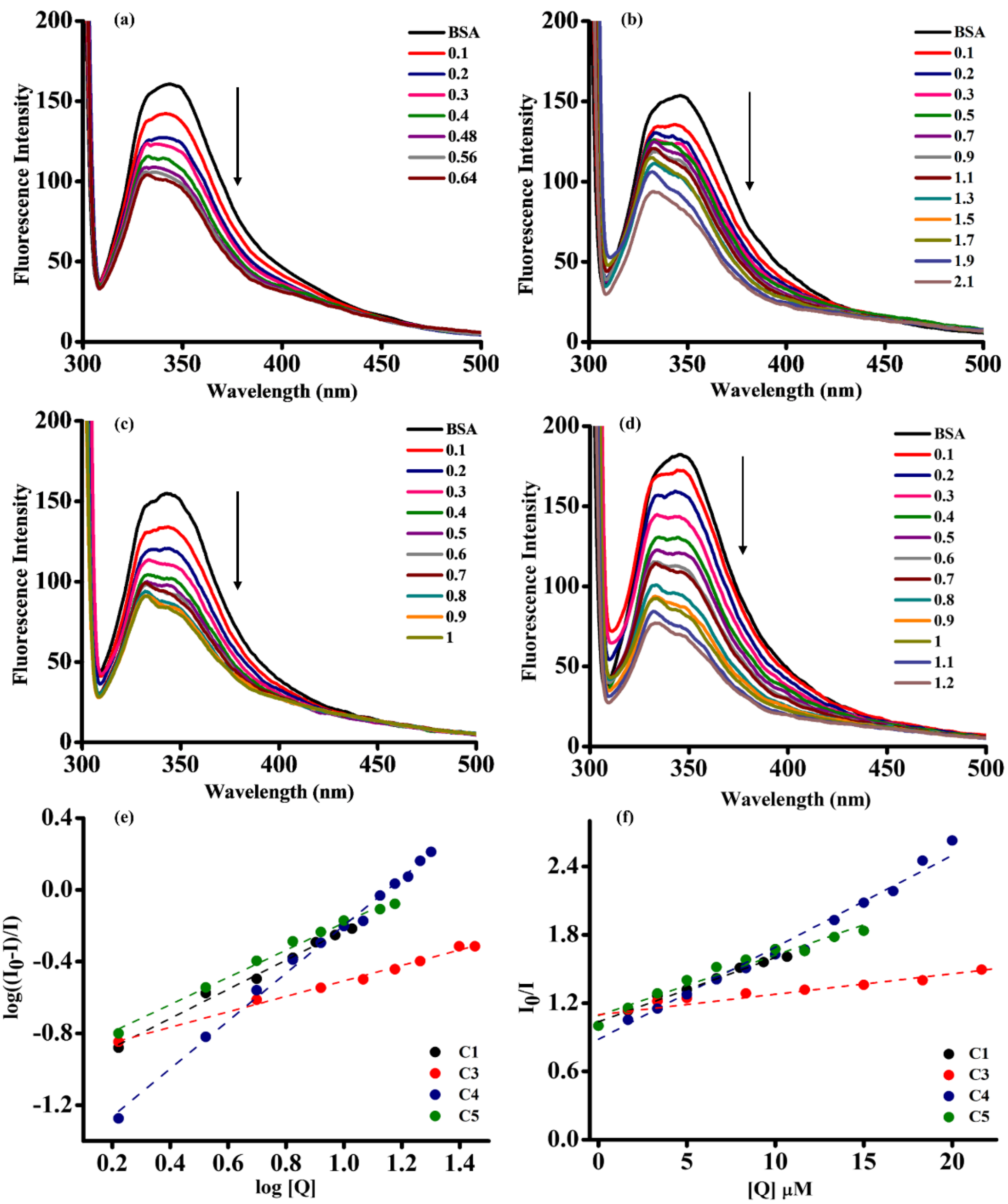

Figure 5.18 The emission spectra of BSA (16.67 x 10-6 M; λ_{ex} = 296 nm, λ_{em} = 344 nm) in presence of increasing amounts of (a) C1, (b) C3, (c) C4 and (d) C5, (e) Scatchard plots and (f) Stern-Volmer plots of fluorescence quenching with different concentrations of complexes

The *n* values for **C1, C4** and **C5** are close to 1, which is suggestive of the presence of a single binding site in the BSA protein structure. However, the K_{BSA} values follow the order **C3** > **C4** > **C1** > **C5**, again revealing the fact that **C3** has an enhanced activity than other complexes and **C5**, having an imidazole backbone, has the weakest interaction with BSA.

The addition of complexes causes quenching of fluorescence which proves that the complexes interacted with the BSA protein. The binding constants were calculated according to Scatchard equation (equation 5.3)[61]:

$$\mathbf{\log [(I_0 - I) / I] = \log K_{BSA} + \mathit{n} \log [Q]} \qquad - (5.3)$$

where K_{BSA} is the binding constant of complexes with BSA (calculated from the intercept of plots of $\log[(I_0–I)/I)$ and $\log[Q]$; Figures 5.18(e), S5.3*) and *n*, the number of binding sites, obtained from the slope value.

Bimolecular quenching rate constant K_q was also determined using equation 5.4:

$$\mathbf{K_q = K_{SV} / \tau_0} \qquad - (5.4)$$

where K_{SV} is the Stern-Volmer constant and τ_0 is the average lifetime of the fluorophore in the absence of the quencher (τ_0 = 10 ns for BSA[62]).

The binding constants for ligands and the complexes are not very different. Complexes **C1** and **C5** have higher while **C3** and **C4** have lower values of binding constants than the ligands. It appears that the interaction with the protein is mainly through ligands and its extent is modified depending on the balance between the σ- and π-interaction with the metal ion in the complexes which affects the electron density over the ligands through polarization.

The values of quenching constants for the binding of BSA to the compounds are of the order 10^{12} $Lmol^{-1}s^{-1}$, which are two-fold higher than the maximum scatter collision quenching constant of BSA, 2.0 x 10^{10} $Lmol^{-1}s^{-1}$.[62] This means that the quenching of BSA fluorescence by the complexes is not initiated by a dynamic mechanism. Also, the double logarithmic Scatchard plots for all complexes were found to be straight lines, which suggests that the quenching is caused by the formation of a complex, indicating a static quenching mechanism.

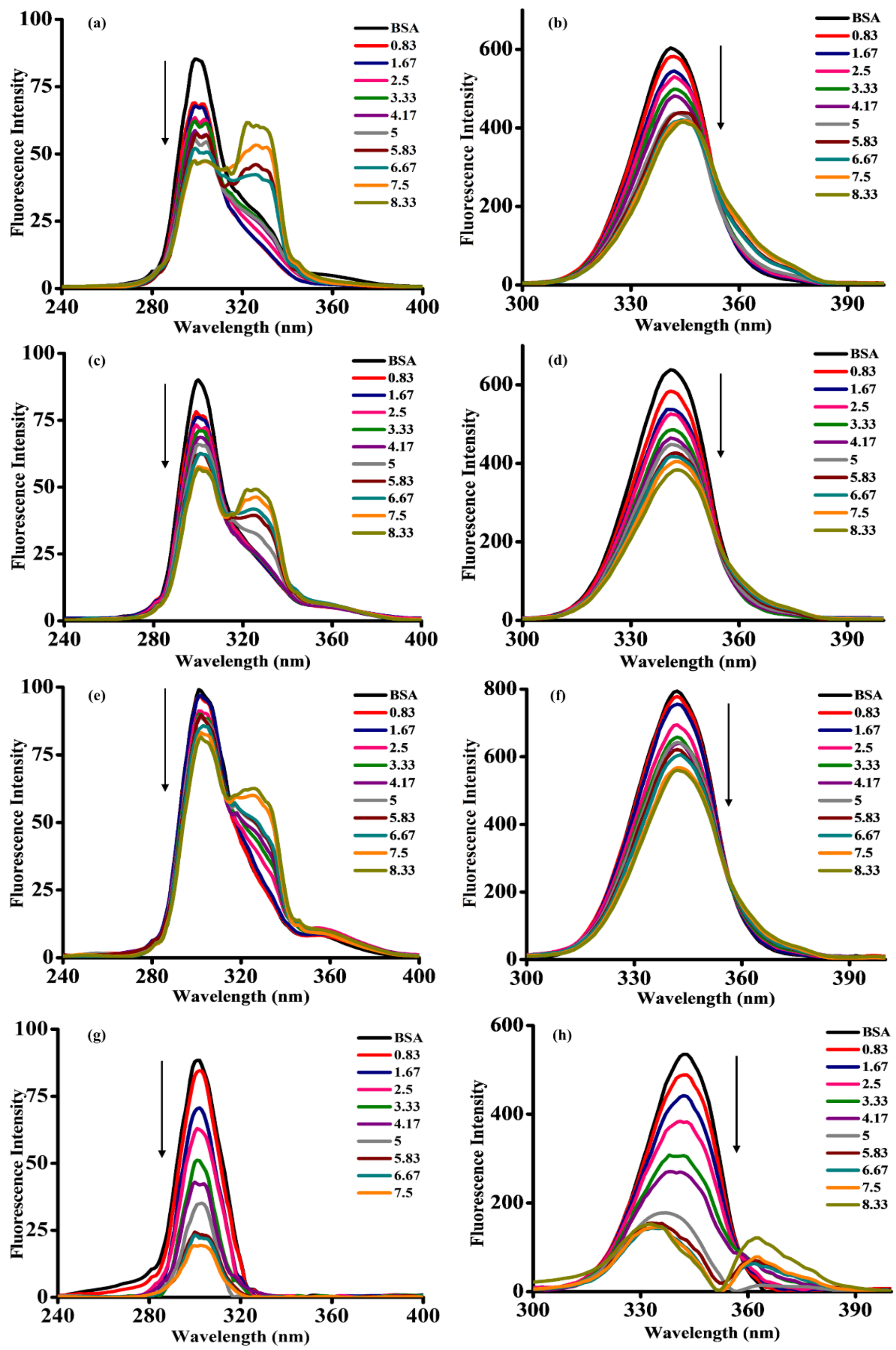

Figure 5.19 Synchronous BSA spectra in tris-HCl/NaCl buffer (pH=7.5) in presence of increasing concentrations of C1 ((a) Δλ =15 nm and (b) Δλ =60 nm), C3 ((c) Δλ =15 nm and (d) Δλ =60 nm), C4 ((e) Δλ =15 nm and (f) Δλ =60 nm) and C5 ((g) Δλ =15 nm and (h) Δλ =60 nm), the downward arrow signifies a decrease in fluorescence intensity with increasing concentration of quencher)

5.4.8.1 BSA conformational analysis

Synchronous fluorescence spectra of BSA were recorded in presence of the synthesized complexes to attain information regarding the molecular microenvironment in the vicinity of the fluorophores.

This study can reflect the spectra of a different nature of chromophores; for a Δλ value of 15 nm, the fluorescence of BSA is characteristic of tyrosine residue, while a Δλ value of 60 nm corresponds to the tryptophan residue.[63,64]

The quenching of BSA fluorescence was monitored through a simultaneous scanning at wavelength difference of 15 nm and 60 nm. The synchronous BSA spectra for various concentrations of complexes at Δλ =15 nm (Figure 5.19) show a slight irregular decrease in the fluorescence intensity at 300 nm with a minor shift of 0-10 nm, while the spectra at Δλ = 60 nm for increasing concentrations of complexes showed a regular and significant decrease in the intensity at 341 nm, upto ~(30-40)% of the initial fluorescence intensity of BSA for compounds **C1**, **C3, C4** and upto 70% for **C5**. These results clearly suggest that all complexes can interact with both Tyr and Trp residues, while the interaction of **C5** with these residues is much stronger as compared to the other complexes.

Table 5.5 BSA and DNA binding parameters of the complexes and ligands

	BSA				DNA	
	K_{sv} (10^5 M^{-1})	K_q (10^{13} $M^{-1}s^{-1}$)	K_{BSA} (10^5 M^{-1})	n	K_{sv} (10^4 M^{-1})	K_b (10^4 M^{-1})
C1	0.611	0.611	0.905	0.815	0.48	0.386
C3	0.221	0.221	1.15	0.431	0.64	0.09
C4	0.617	0.617	1.14	0.76	0.61	1.43
C5	0.723	0.723	0.299	1.33	0.74	3.17
L1	0.444	0.444	0.736	0.789	No Binding	
L3	0.737	0.737	1.412	0.6633	0.25	1.46
L4	0.834	0.834	0.937	0.9499	0.31	3.6
L5	0.648	0.648	1.059	0.7724	No Binding	

5.4.9 DNA binding studies

The ability of metal complexes to bind with DNA can be studied by absorption titration. Generally, a metal complex having an aromatic backbone binds with DNA causing a change in absorption (hypochromism in intercalative mode and hyperchromism in groove binding) and bathochromism (shift in wavelength) as a result of strong stacking interactions between the complex and base pairs of DNA.

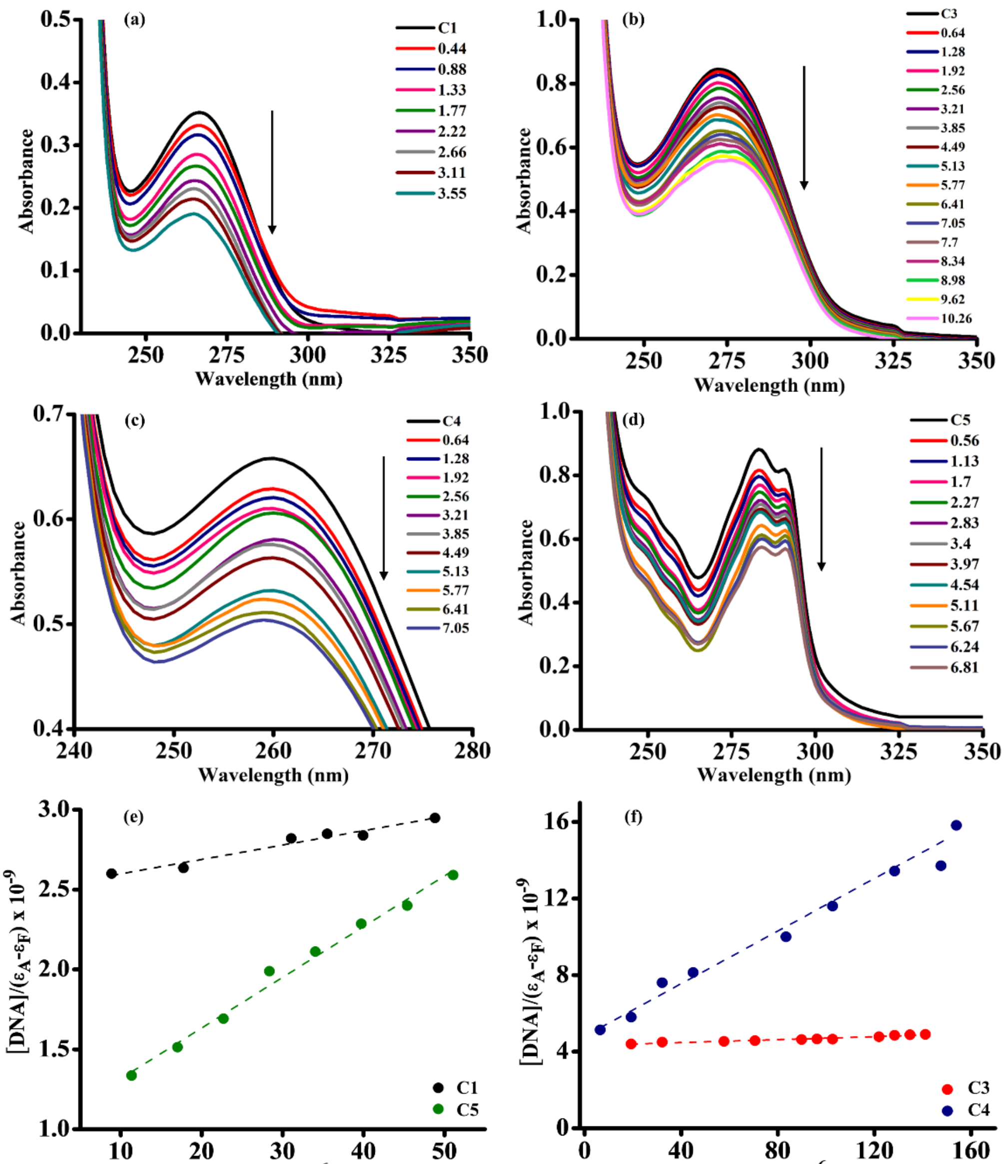

Figure 5.20 (a) Absorption spectra of (a) C1, (b) C3, (c) C4 and (d) C5 (10 µM) in absence and presence of ct-DNA(0-141 µM) at 30°C in 15 mM Tris-HCl/150 mM NaCl buffer (pH=7.5). The downward arrow shows a decrease in absorption intensity with increasing DNA concentrations (e), (f) plots of [DNA]/(ε_A-ε_F) vs. [DNA] for all complexes

We can observe that the absorption band around 270 nm (caused by π-π* transition) suffered a significant hypochromism in all complexes by 25-45% (Figures 5.20, S5.4*). These results are evident of the fact that the complexes could bind to DNA *via* intercalative mode.

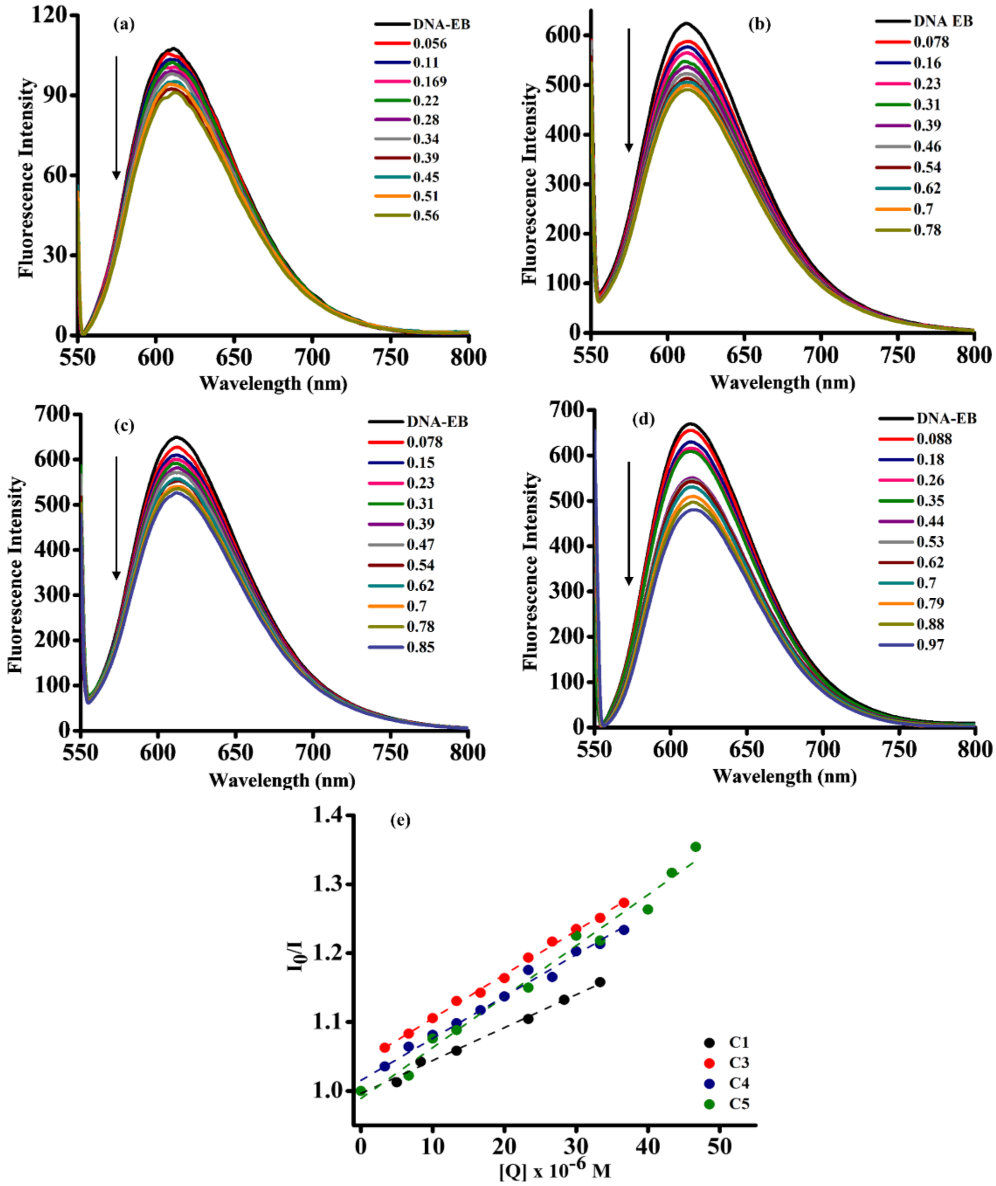

Figure 5.21 Emission spectra of EB bound to DNA in presence of (a) C1, (b) C3, (c) C4 and (d) C5 ([EB]= 166.67 µM, [DNA]= 36.73 µM, λ_{ex} = 546 nm and λ_{em} = 610 nm) (e) Stern-Volmer plots of emission intensity I_0/I vs. [Q]

The intrinsic binding constant, K_b was determined using Mehan's equation[65] (equation 5.5):

$$[DNA] / (\varepsilon_A - \varepsilon_F) = [DNA] / (\varepsilon_b - \varepsilon_F) + 1 / K_b (\varepsilon_b - \varepsilon_F) \qquad - (5.5)$$

where [DNA]= concentration of DNA in base pairs, $\varepsilon_A = A_{obsd}$/[compound], ε_F = extinction coefficient for unbound compound, ε_b = extinction coefficient for compound in fully bound form. The plot of [DNA]/(ε_A-ε_F) vs. [DNA] (Figure 5.6) gave a slope 1/(ε_b-ε_F) and an intercept of 1/K_b(ε_b-ε_F).

It is known that shape, size, hydrophobicity, and electrolytic behavior of the complexes play a vital role in their interactions with DNA. Higher K_b values for **C4** and **C5** suggests that the aromatic bicyclic ligands contribute to a stronger affinity, and hence, better binding ability with ct-DNA. Further, **C5** has the highest binding constant because of having a strongly basic and hydrogen bonding site besides having an aromatic moiety leading to stronger interactions.

Ethidium Bromide (EB) displacement assay was also performed by fluorescence spectral titration technique. These studies too, were performed for all complexes as well as ligands. The titration plots are displayed in Figures 5.21, S5.5*. Addition of complexes cause a quenching in the fluorescence intensity of DNA-EB by ~ 15, 21, 19 and 28% respectively for the complexes. It shows that the complexes can fairly bind to ct-DNA, releasing the already bound EB. The quenching constant, K_{SV} of the compounds was determined from the Stern-Volmer equation (equation 5.2):
$\mathbf{I_0/I = 1 + K_{SV} [Q]}$; K_{SV} was obtained from the slope of the plot of I_0/I vs. [Q] (Figures 5.21, S5.5*) and the values are listed in Table 5.5.

The values follow the order **C5 > C3 > C4 > C1** and fall in the magnitude of 10^4 M^{-1}, which suggests that the complexes interact with DNA *via* intercalative mode. Also, the interaction of **C5** with DNA is strongest. These results are consistent with those obtained from the absorption studies.

5.5 CONCLUSIONS

Four novel mononuclear copper(II) complexes have been synthesized and characterized by various physico-chemical techniques. The single crystal X-ray studies confirmed their structures as having nearly square planar geometry in all the complexes with coordination by the O and N donor atoms of the bidentate ligands. The SOD mimic activity follows the order, **C3 > C4 > C1 > C5.** The IC_{50} values for the complexes reported here are much lower than those reported so far in the literature. The lowest IC_{50} value of **C3** may be attributed to the increased basicity of the nitrogen atom of thiazole ring due to the presence of electron donating methyl group. The higher basicity can enhance the extent of interaction between the superoxide anion and the copper center. The trend observed in the IC_{50} values of SOD activity nearly match the observed band gap values obtained from computational studies. DNA cleavage studies also support the results obtained from SOD mimic activity, all the complexes could cleave supercoiled, nicked and linear forms of plasmid DNA. The binding with BSA indicated a static quenching mechanism and the conformational analyses revealed that the complexes could interact with both the tyrosine and tryptophan residues of BSA; interactions of **C5** were found to be more pronounced than other complexes. DNA binding studies showed that complexes **C4** and **C5** had a better binding ability than **C1** and **C3** with ct-DNA owing to the presence of planar aromatic rings in their structures *via* a moderate intercalative mode.

REFERENCES

1. Beatty, A. M. Hydrogen bonded networks of coordination complexes. *CrystEngComm* **51**, 1–13 (2001).
2. Braga, D., Grepioni, F. & Desiraju, G. R. Crystal Engineering and Organometallic Architecture. *Chem. Rev.* **2665**, 1375–1405 (1998).
3. Braga, D. Intermolecular Interactions in Nonorganic Crystal Engineering. *Acc. Chem. Res.* **33**, 601–608 (2000).
4. Desiraju, G. R. Supramolecular Synthons in Crystal Engineering-A New Organic Synthesis. *Angew. Chem. Int. Ed. Engl.* **34**, 2311–2327 (1995).
5. Desiraju, G. R. Chemical crystallography and crystal engineering. *IUCrJ* vol. 1 380–381 (2014).
6. Bhardwaj, V. & Ballabh, A. Design, synthesis, and application of a new series of organogelator using crystal engineering approach and solvent parameter study: A synergetic approach. *J. Mol. Liq.* **322**, 114520 (2021).
7. Lan, Y., Corradini, M. G., Weiss, R. G., Raghavan, S. R. & Rogers, M. A. To gel or not to gel: correlating molecular gelation with solvent parameters. *Chem. Soc. Rev.* **44**, 6035–6058 (2015).
8. Yadav, P., Kour, D., Gupta, V., Kant, R. & Ballabh, A. Probing the role of weaker interactions in immobilization of solvents in a new class of supramolecular gelator. *RSC Adv.* **3**, 8417–8421 (2013).
9. Yadav, P. & Ballabh, A. Odd–even effect in a thiazole based organogelator: understanding the interplay of non-covalent interactions on property and applications. *New J. Chem.* **39**, 721–730 (2015).
10. Bhardwaj, V. & Ballabh, A. A series of multifunctional pivalamide based Low Molecular Mass Gelators (LMOGs) with potential applications in oil-spill remediation and toxic dye removal. *Colloids Surfaces A Physicochem. Eng. Asp.* **632**, 127813 (2022).
11. Bhardwaj, V. & Ballabh, A. Remediation of Marine Oil Spills and Water Pollution using Low Molecular Weight Organo-Gelators. *Recent Adv. Petrochemical Sci.* **7**, 3 (2022).
12. Etter, M. C. Encoding and Decoding Hydrogen-Bond Patterns of Organic Compounds. *Acc. Chem. Res.* **23**, 120–126 (1990).
13. Mruthyunjayaswamy, B. H. M. & Basavarajaiah, S. M. Synthesis and antimicrobial activity of novel ethyl-5-(ethoxycarbonyl)- 4-methylthiazol-2-yl-carbamate compounds. *Indian J. Chem. - Sect. B Org. Med. Chem.* **48**, 1274–1278 (2009).
14. Biradar, V. D. & Mruthyunjayaswamy, B. H. M. Synthesis characterization and antimicrobial activity studies of some transition metal complexes derived from 5-chloro-3-phenyl-N'-((2-thioxo-1,2-dihydroquinoline-3-yl)methylene)-1H-indole-2-carbohydrazide. *Int. J. Chem. Sci. Res.* **2**, 29–48 (2012).
15. Yernale, N. G. & Mathada, M. B. H. Synthesis, characterization, antimicrobial, DNA cleavage, and in vitro cytotoxic studies of some metal complexes of Schiff base ligand derived from thiazole and quinoline moiety. *Bioinorg. Chem. Appl.* **2014**, 1–17 (2014).
16. Uhlenheuer, D. A., Petkau, K. & Brunsveld, L. Combining supramolecular chemistry with biology. *Chem. Soc. Rev.* **39**, 2817–2826 (2010).
17. Riley, D. P. Functional Mimics of Superoxide Dismutase Enzymes as Therapeutic Agents. *Chem. Rev.* **99**, 2573–2587 (1999).
18. Sheng, Y., Abreu, I. A., Cabelli, D. E., Maroney, M. J., Miller, A. F., Teixeira, M. & Valentine, J. S. Superoxide dismutases and superoxide reductases. *Chem. Rev.* **114**,

3854–3918 (2014).
19. Sankaralingam, M., Lee, Y. M., Nam, W. & Fukuzumi, S. Amphoteric reactivity of metal–oxygen complexes in oxidation reactions. *Coord. Chem. Rev.* **365**, 41–59 (2018).
20. Fukuzumi, S., Ohtsu, H., Ohkubo, K., Itoh, S. & Imahori, H. Formation of superoxide-metal ion complexes and the electron transfer catalysis. *Coord. Chem. Rev.* **226**, 71–80 (2002).
21. Fukuzumi, S., Lee, Y. M. & Nam, W. Structure and reactivity of the first-row d-block metal-superoxo complexes. *Dalt. Trans.* **48**, 9469–9489 (2019).
22. Balasubramanian, V., Ezhevskaya, M., Moons, H., Markus Neuburger, Carol Cristescu, S. V. D. & Cornelia, P. Structural characterization of a highly active superoxide-dismutase mimic. *Phys. Chem. Chem. Phys.* **11**, 6778–6787 (2009).
23. Silavi, R., Divsalar, A. & Saboury, A. A. A short review on the structure – function relationship of artificial catecholase / tyrosinase and nuclease activities of Cu-complexes. *J. Biomol. Struct. Dyn.* **30**, 752–772 (2012).
24. Vamsikrishna, N., Kumar, M. P., Ramesh, G., Ganji, N. & Daravath, S. DNA interactions and biocidal activity of metal complexes of benzothiazole Schiff bases : synthesis , characterization. *J. Chem. Sci.* **129**, 609–622 (2017).
25. Li, D., Tian, J., Kou, Y., Huang, F., Chen, G., Gu, W., Liu, X. & Liao, D. Synthesis , X-ray crystal structures , magnetism , and DNA cleavage properties of copper (II) complexes with 1,4-tpbd ligand. *Dalt. Trans.* 3574–3583 (2009).
26. Patel, M. N., Bhatt, B. S. & Dosi, P. A. Study of SOD mimic and nucleic acid interaction activity exerted by enrofloxacin-based copper(II) complexes. *Chem. Biodivers.* **9**, 2810–2824 (2012).
27. Liu, J., Zhang, T., Lu, T., Qu, L., Zhou, H., Zhang, Q. & Ji, L. DNA-binding and cleavage studies of macrocyclic copper (II) complexes. *J. Inorg. Biochem.* **91**, 269–276 (2002).
28. Metcalfe, C. & Thomas, J. A. Kinetically inert transition metal complexes that reversibly bind to DNA. *Chem. Soc. Rev.* **32**, 215–224 (2003).
29. Krishnamoorthy, P., Sathyadevi, P., Cowley, A. H., Butorac, R. R. & Dharmaraj, N. Evaluation of DNA binding, DNA cleavage, protein binding and in vitro cytotoxic activities of bivalent transition metal hydrazone complexes. *Eur. J. Med. Chem.* **46**, 3376–3387 (2011).
30. Kellett, A., Molphy, Z., Slator, C., Mckee, V. & Farrell, N. P. Molecular methods for assessment of non-covalent metallodrug–DNA interactions. *Chem. Soc. Rev.* **48**, 971–988 (2019).
31. Xiang, Y. & Wu, F. Study of the interaction between a new Schiff-base complex and bovine serum albumin by fluorescence spectroscopy. *Spectrochim. Acta. A. Mol. Biomol. Spectrosc.* **77**, 430–436 (2010).
32. Theodore Peters, J. *All About Albumin - Biochemistry, Genetics, and Medical Applications*. (Elsevier Inc., 1995).
33. Potapov, A. S., Nudnova, E. A., Domina, G. A., Kirpotina, L. N., Quinn, M. T., Khlebnikov, A. I. & Schepetkin, I. A. Synthesis, characterization and potent superoxide dismutase-like activity of novel bis(pyrazole)-2,2′-bipyridyl mixed ligand copper(II) complexes. *Dalt. Trans.* 4488–4498 (2009).
34. Lian, W.-J., Wang, X.-T., Xie, C.-Z., Tian, H., Song, X.-Q., Pan, H.-T., Qiao, X. & Xu, J.-Y. Mixed-ligand copper(II) Schiff base complexes: the role of co- ligand in DNA binding, DNA cleavage, protein binding and cytotoxicity. *Dalt. Trans.* **45**, 9073–9087 (2016).

35. Grau, J., Renau, C., Caballero, A. B., Caubet, A., Pockaj, M., Lorenzo, J. & Gamez, P. Evaluation of the metal-dependent cytotoxic behaviour of coordination compounds. *Dalt. Trans.* **47**, 4902–4908 (2018).
36. Dolomanov, O. V., Bourhis, L. J., Gildea, R. J., Howard, J. A. K. & Puschmann, H. OLEX2: A complete structure solution, refinement and analysis program. *J. Appl. Crystallogr.* **42**, 339–341 (2009).
37. Sheldrick, G. M. A short history of SHELX. *Acta Crystallogr. Sect. A Found. Crystallogr.* **64**, 112–122 (2008).
38. Frisch, M. J., Trucks, G. W., Schlegel, H. B., Scuseria, G. E., Robb, M. A., Cheeseman, J. R. Scalmani, G., Barone, V., Petersson, G. A., Nakatsuji, H., Li, X., Caricato, M., Marenich, A. V., Bloino, J., Janesko, B. G., Gomperts, R., Mennucci, B., Hratchian, H. P., Ortiz, J. V., Izmaylov, A. F. Sonnenberg, J. L. Williams-Young, D., *et al.* Gaussian 16, Revision C.01. *Gaussian, Inc., Wallingford CT, 2016.*
39. Becke, A. D. Density-functional thermochemistry. III. The role of exact exchange. *J. Chem. Phys.* **98**, 5648–5656 (1993).
40. Vosko, S. H., Wilk, L. & Nusair, M. Accurate spin-dependent electron liquid correlation energies for local spin density calculations: a critical analysis. *Can. J. Phys.* **58**, 1200–1211 (1980).
41. Stephens, P. J., Devlin, F. J., Chabalowski, C. F. & Frisch, M. J. Ab Initio calculation of vibrational absorption and circular dichroism spectra using density functional force fields. *J. Phys. Chem.* **98**, 11623–11627 (1994).
42. Lee, C., Yang, W. & Parr, R. G. Development of the Colle-Salvetti correlation-energy formula into a functional of the electron density. *Phys. Rev. B* **37**, 785–789 (1988).
43. McLean, A. D. & Chandler, G. S. Contracted Gaussian basis sets for molecular calculations. I. Second row atoms, Z=11-18. *J. Chem. Phys.* **72**, 5639–5648 (1980).
44. Krishnan, R., Binkley, J. S., Seeger, R. & Pople, J. A. Self-consistent molecular orbital methods. XX. A basis set for correlated wave functions. *J. Chem. Phys.* **72**, 650–654 (1980).
45. Spackman, M. A. & Byrom, P. G. A novel definition of a molecule in a crystal. *Chem. Phys. Lett.* **267**, 215–220 (1997).
46. Spackman, M. A. & Mckinnon, J. J. Fingerprinting intermolecular interactions in molecular crystals. *CrystEngComm* **4**, 378–392 (2002).
47. Wolff, S. K., Grimwood, D. J., McKinnon, J. J., Turner, M. J., Jayatilaka, D. & Spackman, M. A. CrystalExplorer (Version 3.1). *University of Western Australia, Perth* (2012).
48. Spackman, M. A. & Jayatilaka, D. Hirshfeld surface analysis. *CrystEngComm* **11**, 19–32 (2009).
49. Anacona, J. R., Gutierrez, C. & Rodriguez-Barbarin, C. Crystal structure and superoxide dismutase activity of [Cu(ethylenediamine)2Cl] [PF6]. *Monatshefte fur Chemie* **135**, 785–792 (2004).
50. Weser, U. & Schubotz, L. M. Imidazole-bridged copper complexes as Cu2Zn2-Superoxide dismutase models. *J. Mol. Catal.* **13**, 249–261 (1981).
51. Li, Y., Yang, Z. Y. & Wu, J. C. Synthesis, crystal structures, biological activities and fluorescence studies of transition metal complexes with 3-carbaldehyde chromone thiosemicarbazone. *Eur. J. Med. Chem.* **45**, 5692–5701 (2010).
52. Terra, W. S., Ferreira, S. S., Costa, R. O., Mendes, L. L., Franco, R. W. A., Bortoluzzi, A. J., Resende, J. A. L. C., Fernandes, C. & Horn, A. Evaluating the influence of the

diamine unit (ethylenediamine, piperazine and homopiperazine) on the molecular structure, physical chemical properties and superoxide dismutase activity of copper complexes. *Inorganica Chim. Acta* **450**, 353–363 (2016).

53. O'Connor, M., Kellett, A., McCann, M., Rosair, G., McNamara, M., Howe, O., Creaven, B. S., McClean, S., Foltyn-Arfa Kia, A., O'Shea, D. & Devereux, M. Copper(II) complexes of salicylic acid combining superoxide dismutase mimetic properties with DNA binding and cleaving capabilities display promising chemotherapeutic potential with fast acting in vitro cytotoxicity against cisplatin sensitive and resista. *J. Med. Chem.* **55**, 1957–1968 (2012).
54. Roy, S., Banerjee, A., Lima, S., Horn, A., Sampaio, R. M. S. N., Ribeiro, N., Correia, I., Avecilla, F., Carvalho, M. F. N. N., Kuznetsov, M. L., Pessoa, J. C., Kaminsky, W. & Dinda, R. Unusual chemistry of Cu(ii) salan complexes: Synthesis, characterization and superoxide dismutase activity. *New J. Chem.* **44**, 11457–11470 (2020).
55. Rizvi, M. A., Zaki, M., Afzal, M., Mane, M., Kumar, M., Shah, B. A., Srivastav, S., Srikrishna, S., Peerzada, G. M. & Tabassum, S. Nuclear blebbing of biologically active organoselenium compound towards human cervical cancer cell (HeLa): In vitro DNA/HSA binding, cleavage and cell imaging studies. *Eur. J. Med. Chem.* **90**, 876–888 (2015).
56. Brissos, R. F., Torrents, E., Mello, F. M., Pires, W. C., Silveira-Lacerda, E. de P., Caballero, A. B., Caubet, A., Massera, C., Roubeau, O., Teat, S. J. & Gamez, P. Highly cytotoxic DNA-interacting copper(II) coordination compounds. *Metallomics* **6**, 1853–1868 (2014).
57. Pitie, M. & Pratviel, G. Activation of DNA Carbon - Hydrogen Bonds by Metal Complexes. *Chem. Rev.* **110**, 1018–1059 (2010).
58. Kumar, R. R., Subarkhan, M. K. M. & Ramesh, R. Synthesis and Structure of Nickel(II) thiocarboxamide Complexes: Effect of ligand substitutions on DNA/Protein binding, Antioxidant and Cytotoxicity. *RSC Adv.* **5**, 46760–46773 (2015).
59. Zhou, X.-Q. Sun, Q. Jiang, L. Li, S.-T. Gu, W. Tian, J.-L. Liu, X. Yan, S.-P. Synthesis, Characterization, DNA/BSA interactions and Anticancer Activity of achiral and chiral copper complexes. *Dalt. Trans.* **44**, 9516–9527 (2015).
60. Lakowicz, J. R. & Weber, G. Quenching of fluorescence by oxygen. A probe for structural fluctuations in macromolecules. *Biochemistry* **12**, 4161–4170 (1973).
61. Min, J., Meng-Xia, X., Dong, Z., Yuan, L., Xiao-Yu, L. & Xing, C. Spectroscopic studies on the interaction of cinnamic acid and its hydroxyl derivatives with human serum albumin. *J. Mol. Struct.* **692**, 71–80 (2004).
62. Shahabadi, N. & Mohammadpur, M. Study on the interaction of sodium morin-5-sulfonate with bovine serum albumin by spectroscopic techniques. *Spectrochim. Acta Part A Mol. Biomol. Spectrosc.* **86**, 191–195 (2012).
63. Tang, J., Luan, F. & Chen, X. Binding analysis of glycyrrhetinic acid to human serum albumin: Fluorescence spectroscopy, FTIR, and molecular modeling. *Bioorganic Med. Chem.* **14**, 3210–3217 (2006).
64. Senthil Raja, D., Bhuvanesh, N. S. P. & Natarajan, K. Effect of N(4)-phenyl substitution in 2-oxo-1,2-dihydroquinoline-3- carbaldehyde semicarbazones on the structure, DNA/protein interaction, and antioxidative and cytotoxic activity of Cu(II) complexes. *Inorg. Chem.* **50**, 12852–12866 (2011).
65. Pyle, A. M. Rehmann, J. P. Meshoyrer, R. Kumar, C. V. Turro, N. J. Barton, J. K. Mixed-Ligand Complexes of Ruthenium(II): Factors Governing Binding to DNA. *J. Am. Chem. Soc.* **111**, 3051–3058 (1989).

*SUPPLEMENTARY DATA

SOD plots of ligands

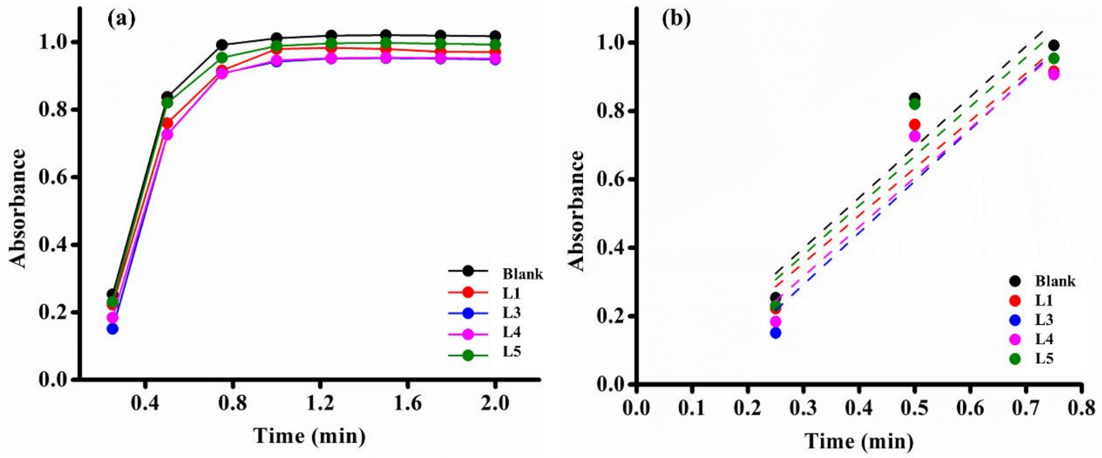

Figure S5.1 Plots of Absorbance recorded at 560.0 nm at an interval of 15 sec for different concentrations of ligands (0.25 mM)

PXRD of C4

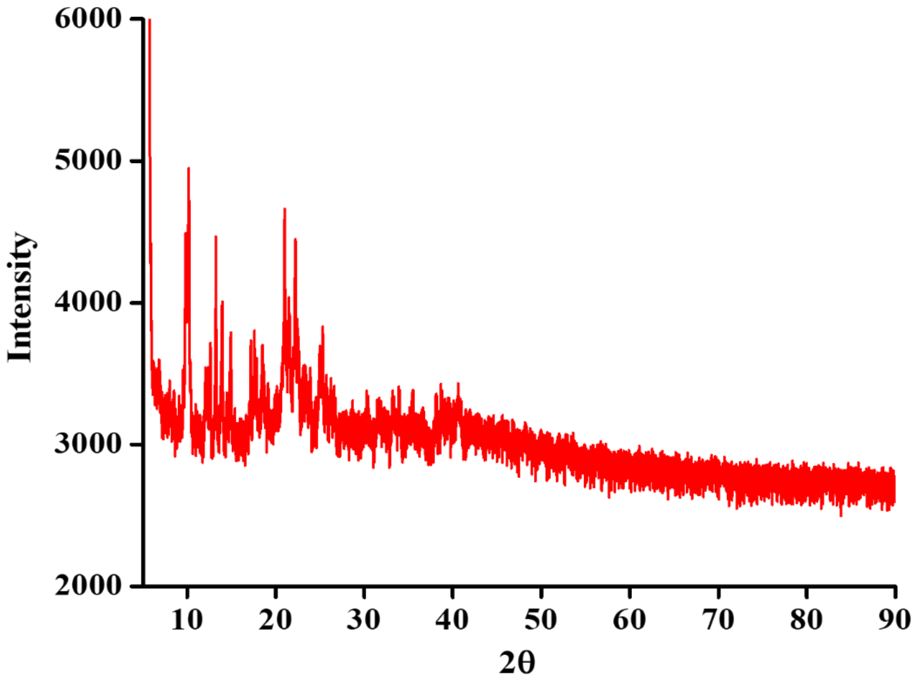

Figure S5.2 Powder X-ray diffraction spectrum of complex C4

BSA plots of ligands

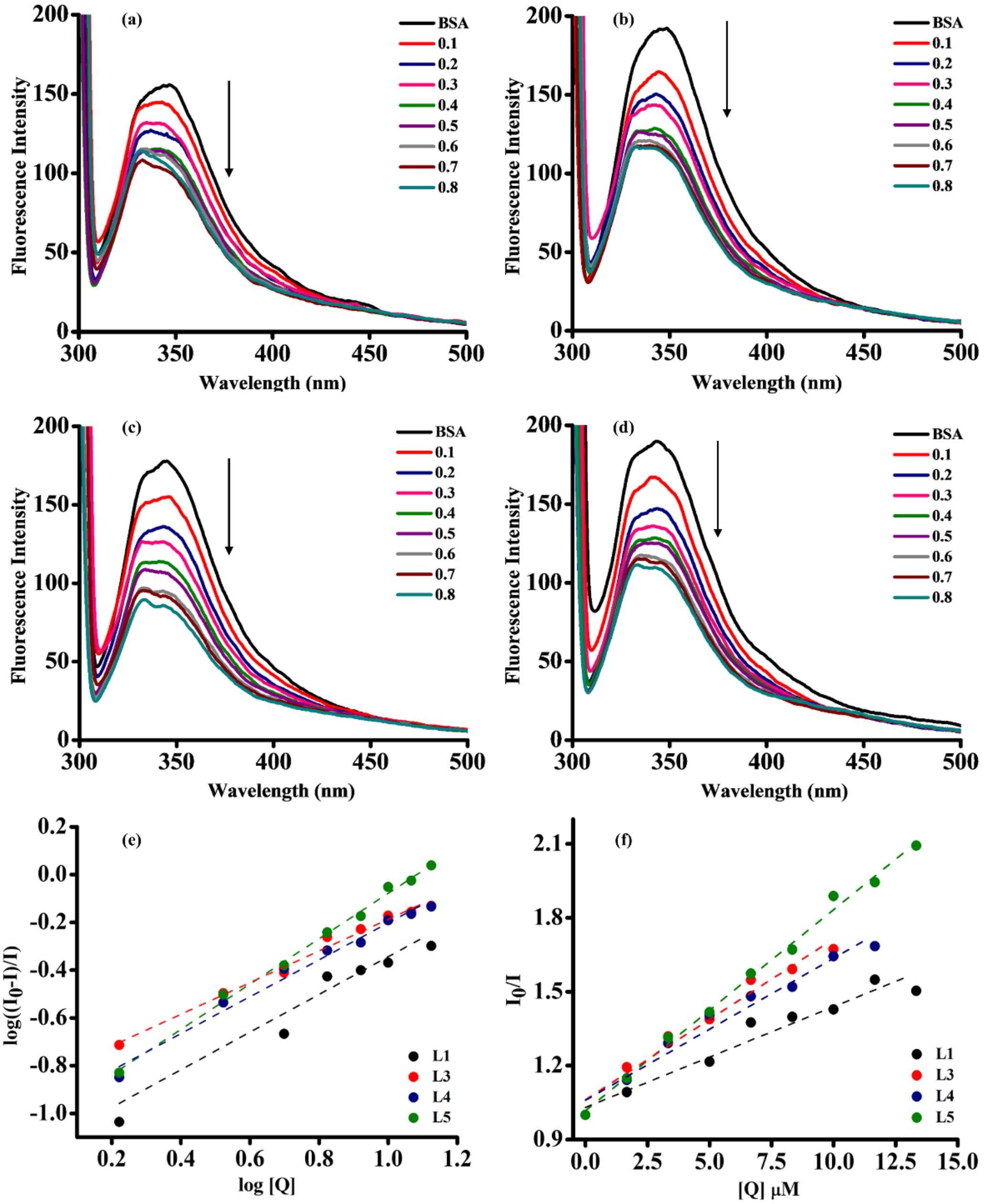

Figure S5.3 Emission spectra of BSA in presence of increasing amounts of (a) L1, (b) L3, (c) L4 and (d) L5 (e) Scatchard plots and (f) Stern-Volmer plots of fluorescence quenching with different concentrations of ligands

DNA plots of ligands

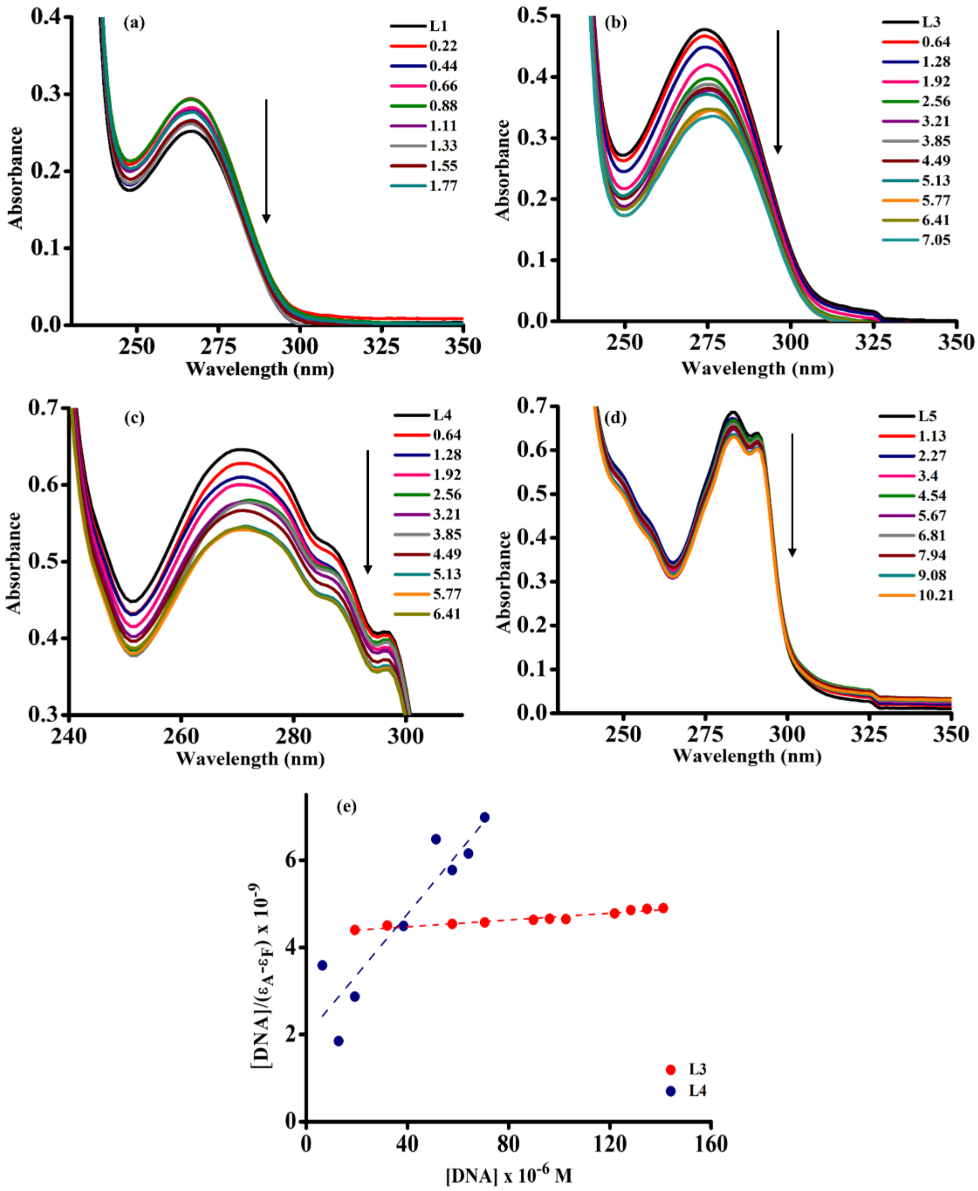

Figure S5.4 Absorption spectra of (a) L1, (b) L3, (c) L4 and (d) L5 (10 μM) in absence and presence of ct-DNA(0-141 μM) at 30°C in 15 mM Tris-HCl/150 mM NaCl buffer (pH=7.5). The downward arrow shows a decrease in absorption intensity with increasing DNA concentrations (e), (f) plots of [DNA]/(ε_A-ε_F) vs. [DNA] for all ligands

DNA-EB plots of ligands

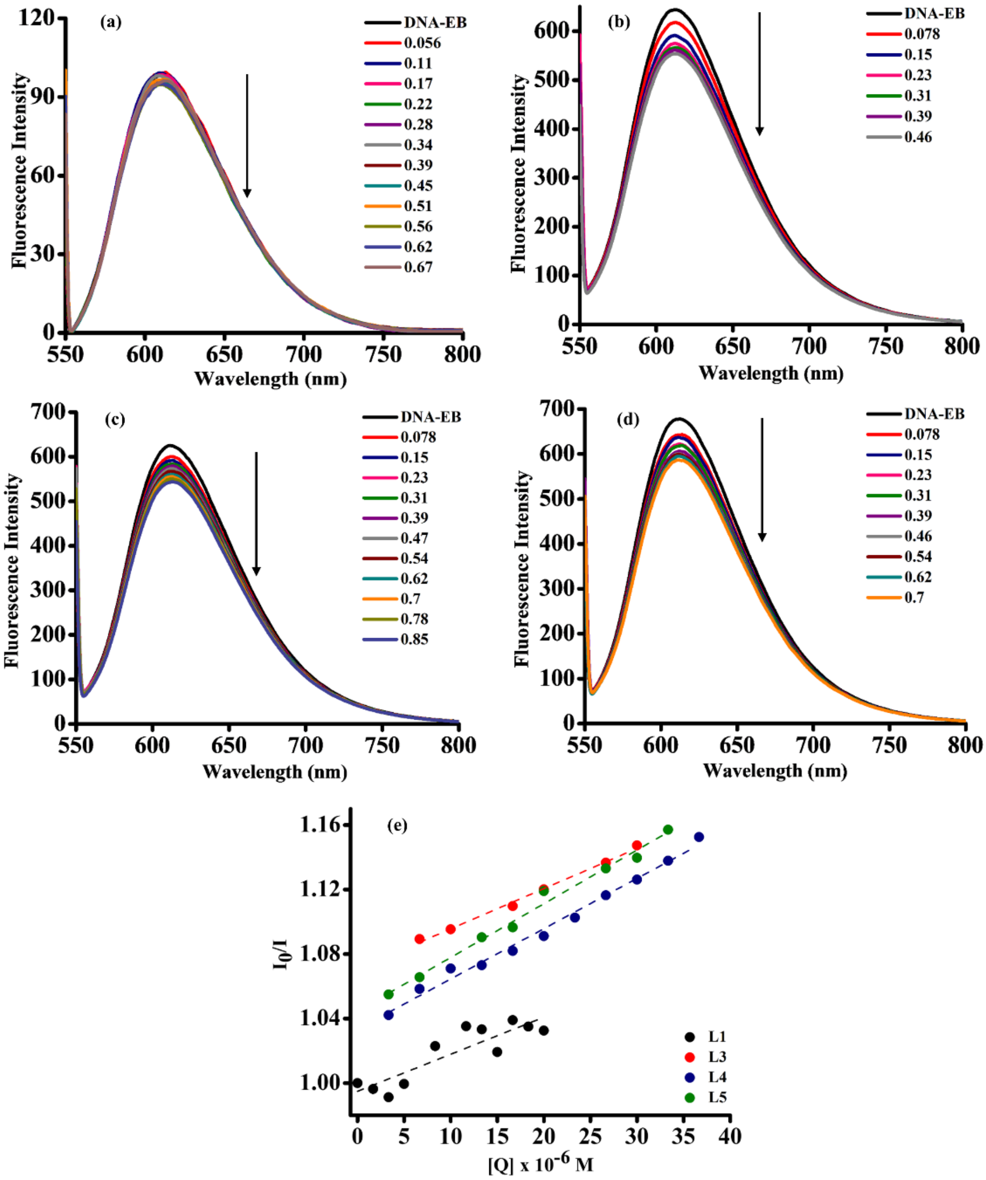

Figure S5.5 Emission spectra of EB bound to DNA in presence of (a) L1, (b) L3, (c) L4, (d) L5 and (e) Stern-Volmer plot

Crystallographic Parameters

Table S5.1 Crystallographic parameters

	L1	L2	L3	L5
Empirical formula	$C_8H_{12}N_2OS$	$C_9H_{14}N_2OS$	$C_9H_{14}N_2OS$	$C_{12}H_{15}N_3O$
Formula weight	184.26	198.28	198.28	217.27
Temperature/K	293	293	293	293
Crystal system	monoclinic	monoclinic	orthorhombic	orthorhombic
Space group	$P2_1/c$	$P2_1/c$	*Pbca*	$Pca2_1$
a/Å	11.0493(8)	10.1121(8)	12.4853(7)	11.8348(13)
b/Å	8.2781(5)	10.8147(7)	11.9525(7)	9.8438(7)
c/Å	11.5947(10)	10.2917(6)	14.2122(7)	10.0286(10)
α/°	90	90	90	90
β/°	117.457(10)	101.451(7)	90	90
γ/°	90	90	90	90
Volume/Å^3	941.09(15)	1103.10(13)	2120.9(2)	1168.33(19)
Z	4	4	8	4
ρ_{calc}g/cm^3	1.3004	1.194	1.242	1.2351
μ/mm^{-1}	0.299	0.260	0.270	0.082
F(000)	392.6	424.0	848.0	464.2
Crystal size/mm^3	0.2 × 0.1 × 0.1	0.3 × 0.3 × 0.2	0.1 × 0.05 × 0.05	0.2 × 0.2 × 0.1
Radiation	Mo Kα (λ = 0.71073)	Mo Kα (λ = 0.71073)	Mo Kα (λ = 0.71073)	Mo Kα (λ = 0.71073)
2Θ range for data collection/°	6.32 to 52.72	7.35 to 56.562	6.526 to 56.528	6.74 to 52.72
Index ranges	$-13 \le h \le 14$, $-10 \le k \le 11$, $-15 \le l \le 15$	$-13 \le h \le 13$, $-14 \le k \le 13$, $-13 \le l \le 13$	$-16 \le h \le 16$, $-15 \le k \le 13$, $-18 \le l \le 18$	$-15 \le h \le 14$, $-13 \le k \le 13$, $-11 \le l \le 12$
Reflections collected	10539	12256	13010	6367
Independent reflections	1926 [R_{int} = 0.0206, R_{sigma} = 0.0168]	2608 [R_{int} = 0.0290, R_{sigma} = 0.0237]	2568 [R_{int} = 0.0763, R_{sigma} = 0.0725]	2234 [R_{int} = 0.0331, R_{sigma} = 0.0445]
Data/restraints/parameters	1926/0/112	2608/0/122	2568/0/122	2234/1/148
Goodness-of-fit on F^2	1.077	1.060	0.983	1.032
Final R indexes [I>=2σ (I)]	R_1 = 0.0346, wR_2 = 0.0920	R_1 = 0.0408, wR_2 = 0.0996	R_1 = 0.0589, wR_2 = 0.1446	R_1 = 0.0601, wR_2 = 0.1437
Final R indexes [all data]	R_1 = 0.0392, wR_2 = 0.0977	R_1 = 0.0582, wR_2 = 0.1110	R_1 = 0.1266, wR_2 = 0.1991	R_1 = 0.0795, wR_2 = 0.1598
Largest diff. peak/hole / e Å^{-3}	0.26/-0.21	0.19/-0.23	0.25/-0.27	0.26/-0.25
Flack Parameter	-	-	-	-1.5(11)
CCDC Number	1858954	1991876	1991874	1858955

	C1	C3	C5
Empirical formula	$C_{16}H_{22}CuN_4O_2S_2$	$C_9H_{13}Cu_{0.5}N_2OS$	$C_{24}H_{28}CuN_6O_2$
Formula weight	430.03	229.04	496.06
Temperature/K	293	293	293
Crystal system	triclinic	monoclinic	monoclinic
Space group	***P-1***	***$P2_1/c$***	***$P2_1/n$***
a/Å	5.8591(3)	5.8532(6)	11.5145(4)
b/Å	12.6848(7)	13.8390(12)	12.0598(8)
c/Å	13.8414(7)	13.1745(11)	17.8638(7)
α/°	73.829(4)	90	90
β/°	86.604(4)	96.376(9)	99.826(3)
γ/°	78.576(4)	90	90
Volume/Å^3	968.43(9)	1060.56(18)	2444.2(2)
Z	2	4	4
ρ_{calc}g/cm^3	1.475	1.434	1.348
μ/mm^{-1}	1.360	1.247	0.926
F(000)	446.0	478.0	1036.0
Crystal size/mm^3	0.3 × 0.2 × 0.08	0.3 × 0.05 × 0.05	0.2 × 0.1 × 0.01
Radiation	MoKα (λ = 0.71073)	MoKα (λ = 0.71073)	MoKα (λ = 0.71073)
2Θ range for data collection/°	6.664 to 58.208	6.66 to 58.248	5.7 to 58.616
Index ranges	$-8 \le h \le 7$, $-16 \le k \le 17$, $-18 \le l \le 18$	$-7 \le h \le 7$, $-17 \le k \le 18$, $-17 \le l \le 17$	$-15 \le h \le 15$, $-16 \le k \le 16$, $-23 \le l \le 23$
Reflections collected	21178	12804	27508
Independent reflections	4665 [R_{int} = 0.0404, R_{sigma} = 0.0344]	2632 [R_{int} = 0.0633, R_{sigma} = 0.0556]	5997 [R_{int} = 0.1293, R_{sigma} = 0.1413]
Data/restraints/parameters	4665/0/235	2632/0/128	5997/0/304
Goodness-of-fit on F^2	1.090	1.081	1.056
Final R indexes [I>=2σ (I)]	R_1 = 0.0584, wR_2 = 0.1414	R_1 = 0.0445, wR_2 = 0.0843	R_1 = 0.0828, wR_2 = 0.1896
Final R indexes [all data]	R_1 = 0.0727, wR_2 = 0.1490	R_1 = 0.0847, wR_2 = 0.1026	R_1 = 0.1809, wR_2 = 0.2429
Largest diff. peak/hole / e Å^{-3}	1.34/-0.62	0.64/-0.34	1.16/-0.52
CCDC Number	1991875	1991865	1991893

H-bond parameters

Table S5.2

D	H	A	d(D-H)/Å	d(H-A)/Å	d(D-A)/Å	D-H-A/°	Symmetry Op. for A
				L1			
N2	H2	N1	0.86	2.26	3.1071	167.6	1-X,1-Y,1-Z
C3	H3	O1	0.93	2.55	3.210	128.1	-X,-1/2+Y,1/2-Z
				L2			
N2	H2	O1	0.86	2.22	3.0617	168.1	+X,1/2-Y,1/2+Z
				L3			
N2	H2	N1	0.86	2.25	3.100	170.3	1-X,1-Y,-Z
C1	H1B	O1	0.96	2.65	3.476	143.9	+X,3/2-Y,-1/2+Z
				L5			
N2	H2	N3	0.86	2.11	2.894	151.8	1/2-X,+Y,1/2+Z
N2	H2	O1	0.86	2.28	2.748	114.1	+X,+Y,+Z
N1	H1	O1	0.86	2.59	3.223	131.2	1/2-X,+Y,-1/2+Z
				C1			
C1	H1	O1	0.93	2.45	2.910	110.3	1-X,1-Y,-Z
C9	H9	O2	0.93	2.45	2.901	110.2	1-X,-Y,1-Z
				C3			
C7	H7	O1	0.93	2.43	2.896	110.8	1-X,1-Y,-Z
				C5			
N2	H2	N4	0.86	2.10	2.948	167.8	-1/2+X,1/2-Y,-1/2+Z
N5	H5	N1	0.86	2.16	2.989	161.3	1/2+X,1/2-Y,1/2+Z
C8	H8	O2	0.93	2.50	3.123	124.1	+X,+Y,+Z
C24	H24	O1	0.93	2.42	3.029	123.4	+X,+Y,+Z

Spectral Data – NMR – ^{1}H and ^{13}C

L1

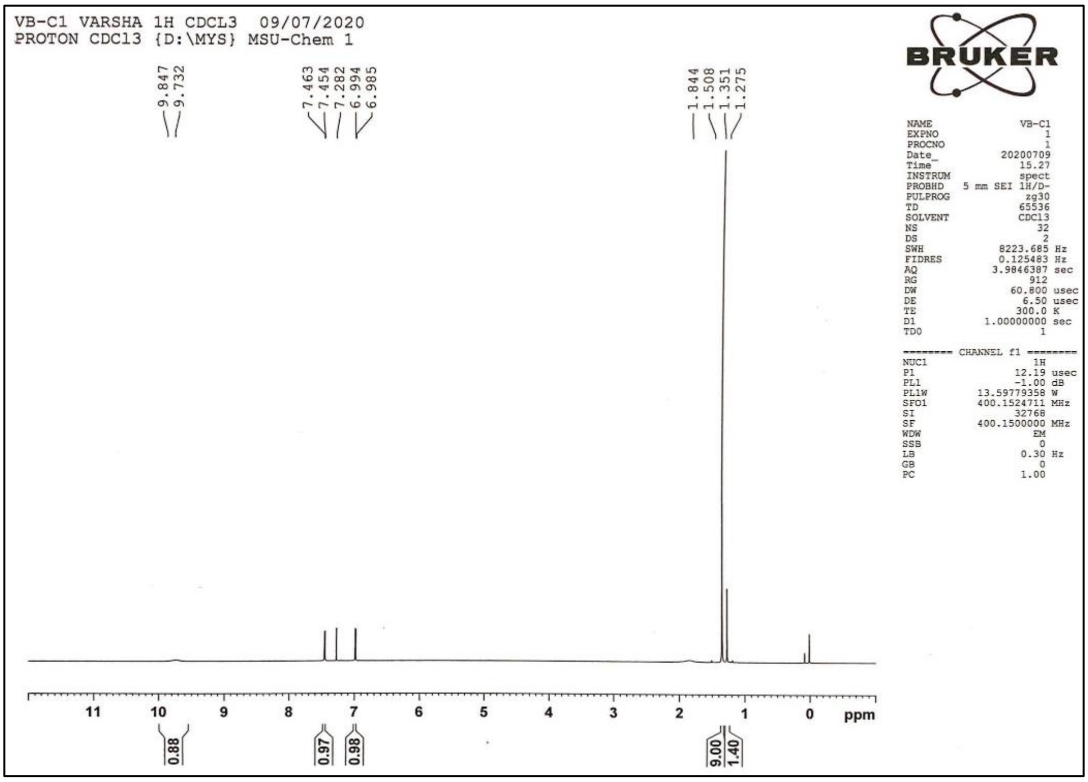

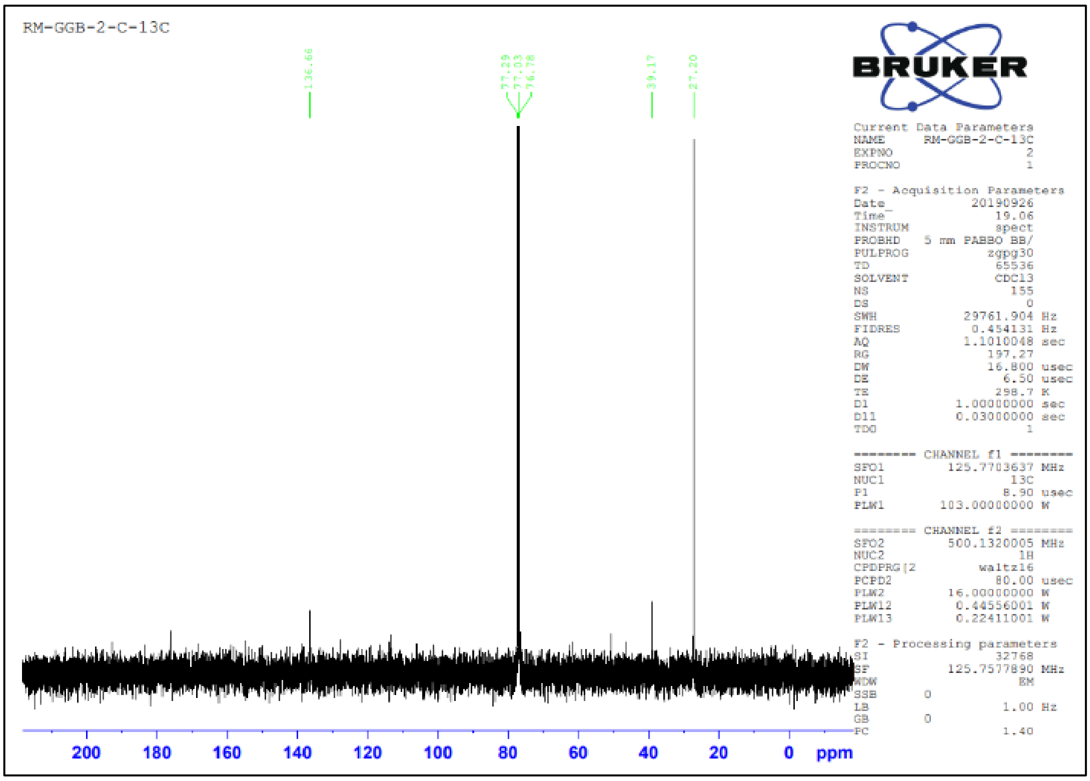

L2

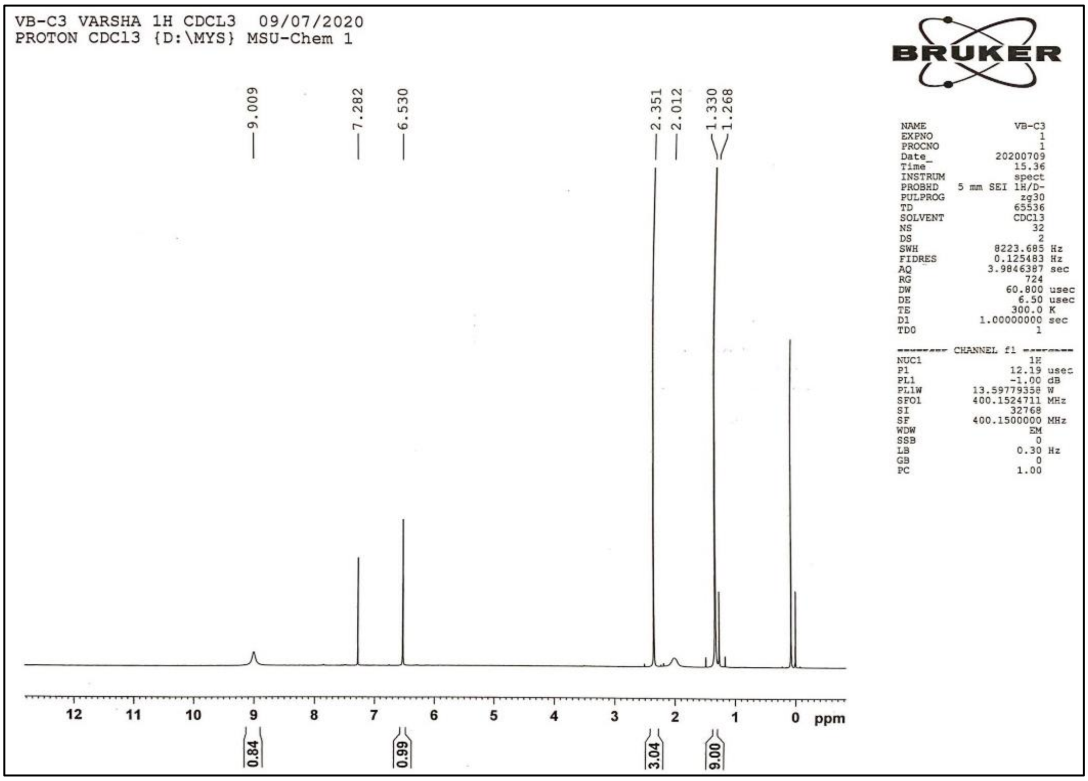
VB-C3 VARSHA 1H CDCL3 09/07/2020
PROTON CDCl3 {D:\MYS} MSU-Chem 1
9.009
7.282
6.530
2.351
2.012
1.330
1.268
NAME VB-C3
EXPNO 1
PROCNO 1
Date_ 20200709
Time 15.36
INSTRUM spect
PROBHD 5 mm SEI 1H/D-
PULPROG zg30
TD 65536
SOLVENT CDCl3
NS 32
DS 2
SWH 8223.685 Hz
FIDRES 0.125483 Hz
AQ 3.9846387 sec
RG 724
DW 60.800 usec
DE 6.50 usec
TE 300.0 K
D1 1.00000000 sec
TD0 1
CHANNEL f1
NUC1 1H
P1 12.19 usec
PL1 -1.00 dB
PL1W 13.59779358 W
SFO1 400.1524711 MHz
SI 32768
SF 400.1500000 MHz
WDW EM
SSB 0
LB 0.30 Hz
GB 0
PC 1.00
ppm
0.84
0.99
3.04
9.00

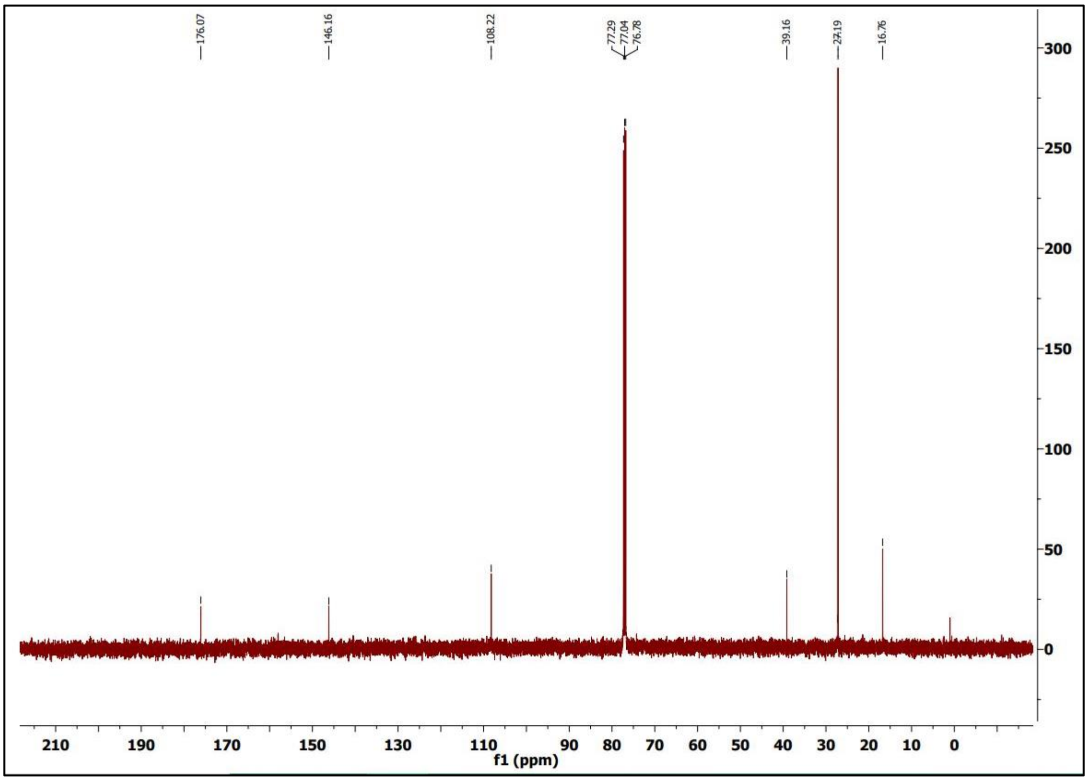
176.07
146.16
108.22
77.29
77.04
76.78
39.16
27.19
16.76
f1 (ppm)

L3

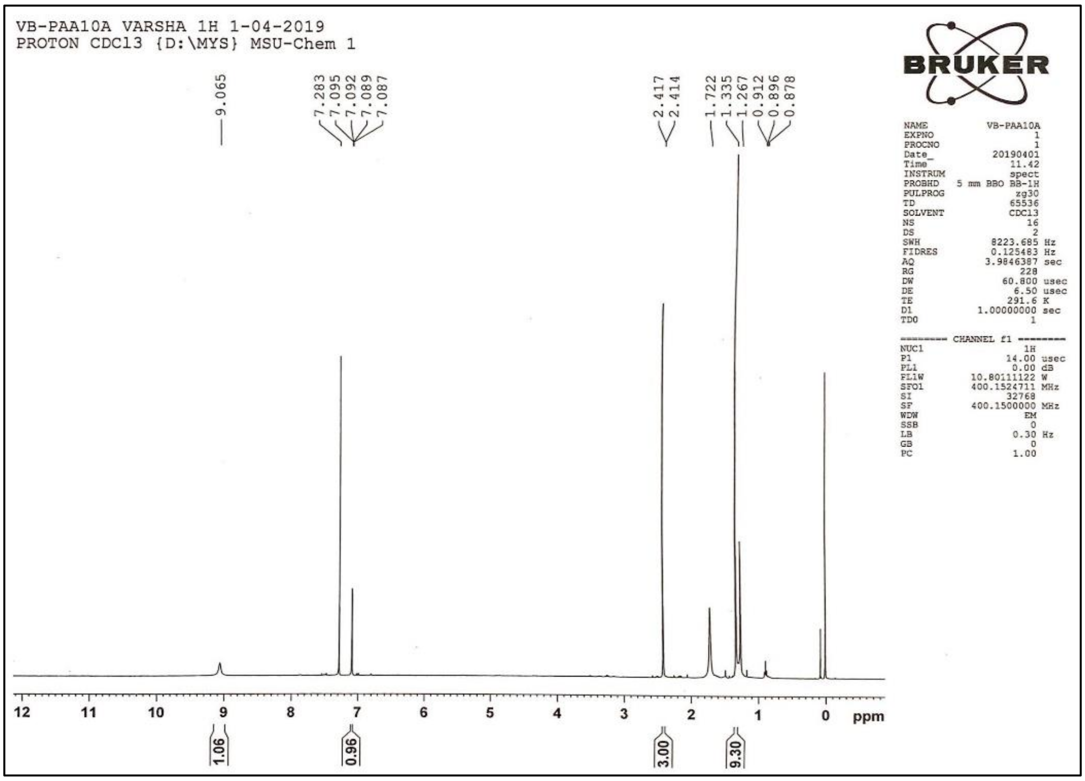
VB-PAA10A VARSHA 1H 1-04-2019
PROTON CDCl3 {D:\MYS} MSU-Chem 1
9.065
7.283
7.095
7.092
7.089
7.087
2.417
2.414
1.722
1.335
1.267
0.912
0.896
0.878
BRUKER
1.06
0.96
3.00
9.30
ppm

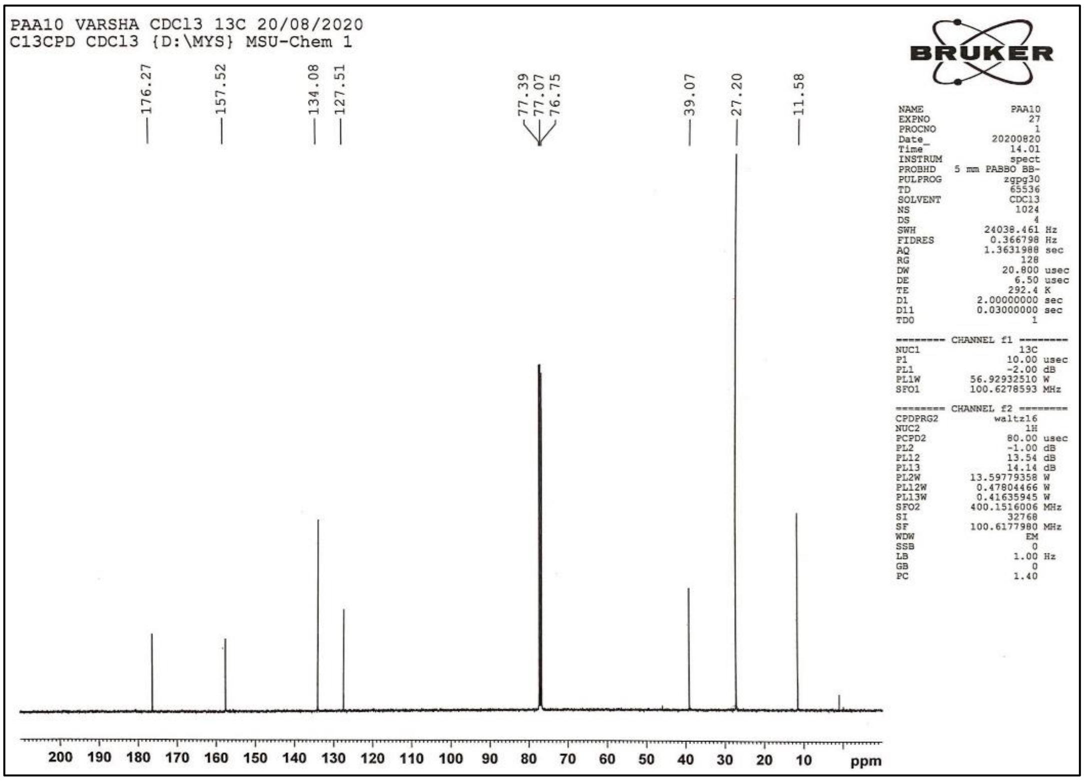
PAA10 VARSHA CDCl3 13C 20/08/2020
C13CPD CDCl3 {D:\MYS} MSU-Chem 1
176.27
157.52
134.08
127.51
77.39
77.07
76.75
39.07
27.20
11.58
BRUKER
ppm

L4

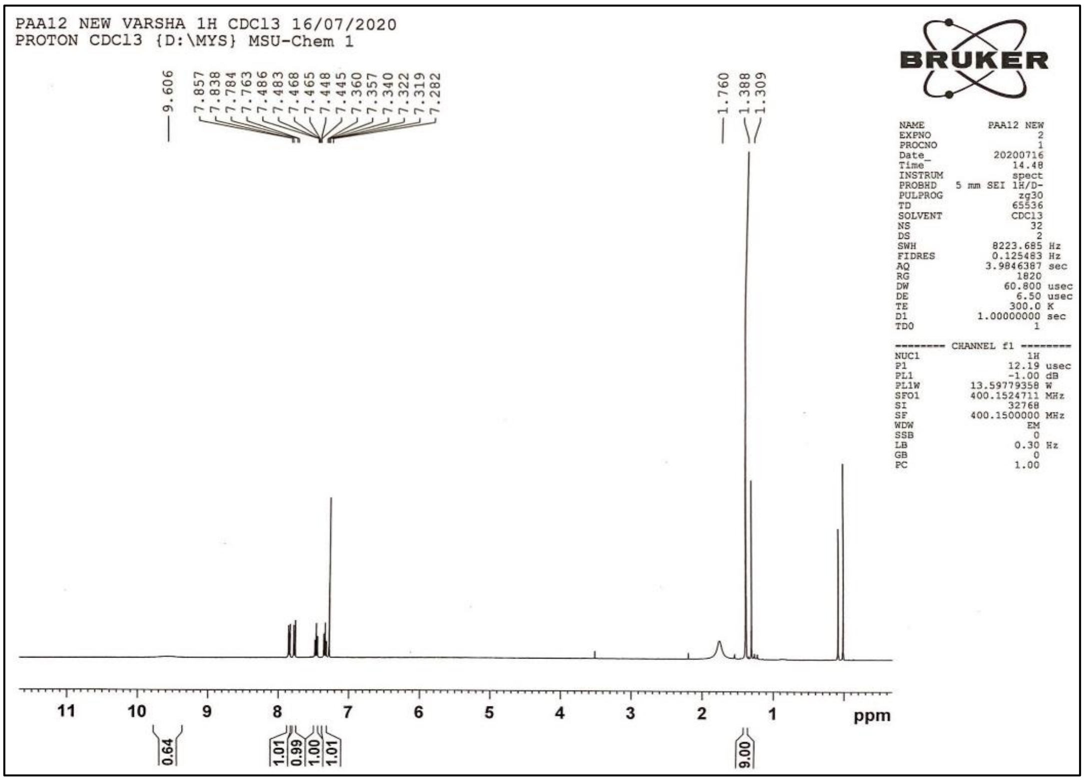
PAA12 NEW VARSHA 1H CDCl3 16/07/2020
PROTON CDCl3 {D:\MYS} MSU-Chem 1
BRUKER
9.606
7.857 7.838 7.784 7.763 7.486 7.483 7.468 7.465 7.448 7.445 7.360 7.357 7.340 7.322 7.319 7.282
1.760 1.388 1.309
NAME PAA12 NEW
EXPNO 2
PROCNO 1
Date_ 20200716
Time 14.48
INSTRUM spect
PROBHD 5 mm SEI 1H/D-
PULPROG zg30
TD 65536
SOLVENT CDCl3
NS 32
DS 2
SWH 8223.685 Hz
FIDRES 0.125483 Hz
AQ 3.9846387 sec
RG 1820
DW 60.800 usec
DE 6.50 usec
TE 300.0 K
D1 1.00000000 sec
TD0 1
======== CHANNEL f1 ========
NUC1 1H
P1 12.19 usec
PL1 -1.00 dB
PL1W 13.59779358 W
SFO1 400.1524711 MHz
SI 32768
SF 400.1500000 MHz
WDW EM
SSB 0
LB 0.30 Hz
GB 0
PC 1.00
11 10 9 8 7 6 5 4 3 2 1 ppm
0.64
1.01 0.99 1.00 1.01
9.00

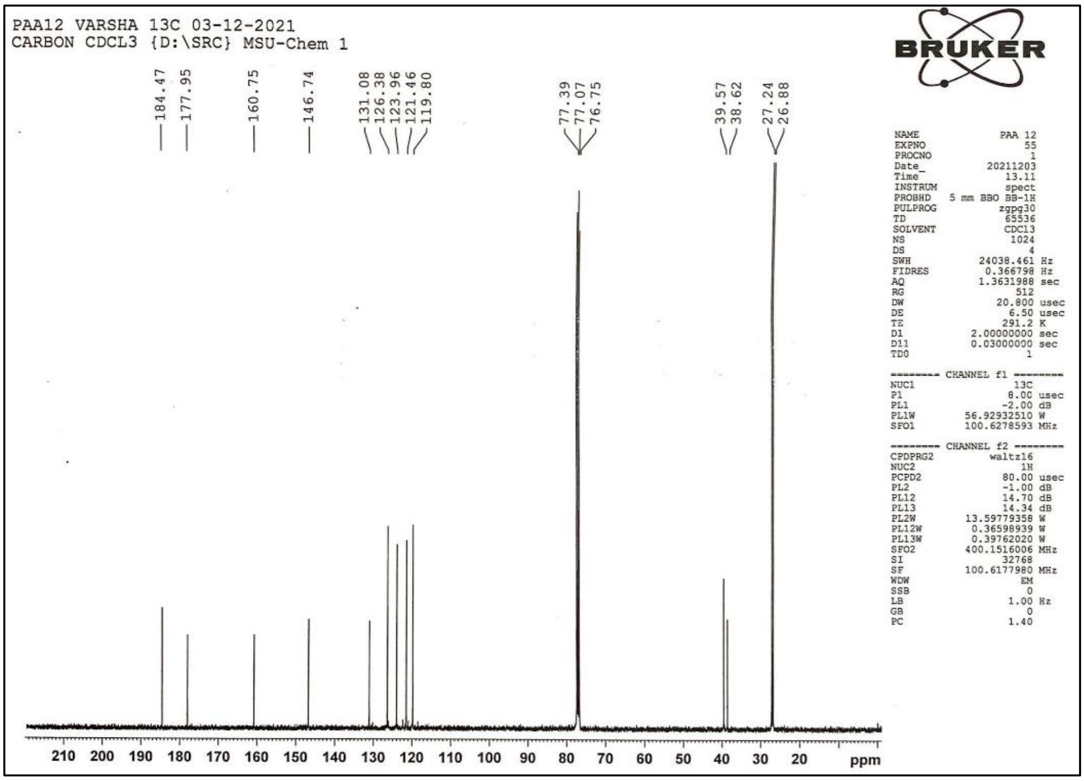
PAA12 VARSHA 13C 03-12-2021
CARBON CDCL3 {D:\SRC} MSU-Chem 1
BRUKER
184.47 177.95 160.75 146.74 131.08 126.38 123.96 121.46 119.80 77.39 77.07 76.75 39.57 38.62 27.24 26.88
NAME PAA 12
EXPNO 55
PROCNO 1
Date_ 20211203
Time 13.11
INSTRUM spect
PROBHD 5 mm BBO BB-1H
PULPROG zgpg30
TD 65536
SOLVENT CDCl3
NS 1024
DS 4
SWH 24038.461 Hz
FIDRES 0.366798 Hz
AQ 1.3631988 sec
RG 512
DW 20.800 usec
DE 6.50 usec
TE 291.2 K
D1 2.00000000 sec
D11 0.03000000 sec
TD0 1
======== CHANNEL f1 ========
NUC1 13C
P1 8.00 usec
PL1 -2.00 dB
PL1W 56.92932510 W
SFO1 100.6278593 MHz
======== CHANNEL f2 ========
CPDPRG2 waltz16
NUC2 1H
PCPD2 80.00 usec
PL2 -1.00 dB
PL12 14.70 dB
PL13 14.34 dB
PL2W 13.59779358 W
PL12W 0.36598939 W
PL13W 0.39762020 W
SFO2 400.1516006 MHz
SI 32768
SF 100.6177980 MHz
WDW EM
SSB 0
LB 1.00 Hz
GB 0
PC 1.40
210 200 190 180 170 160 150 140 130 120 110 100 90 80 70 60 50 40 30 20 ppm

L5

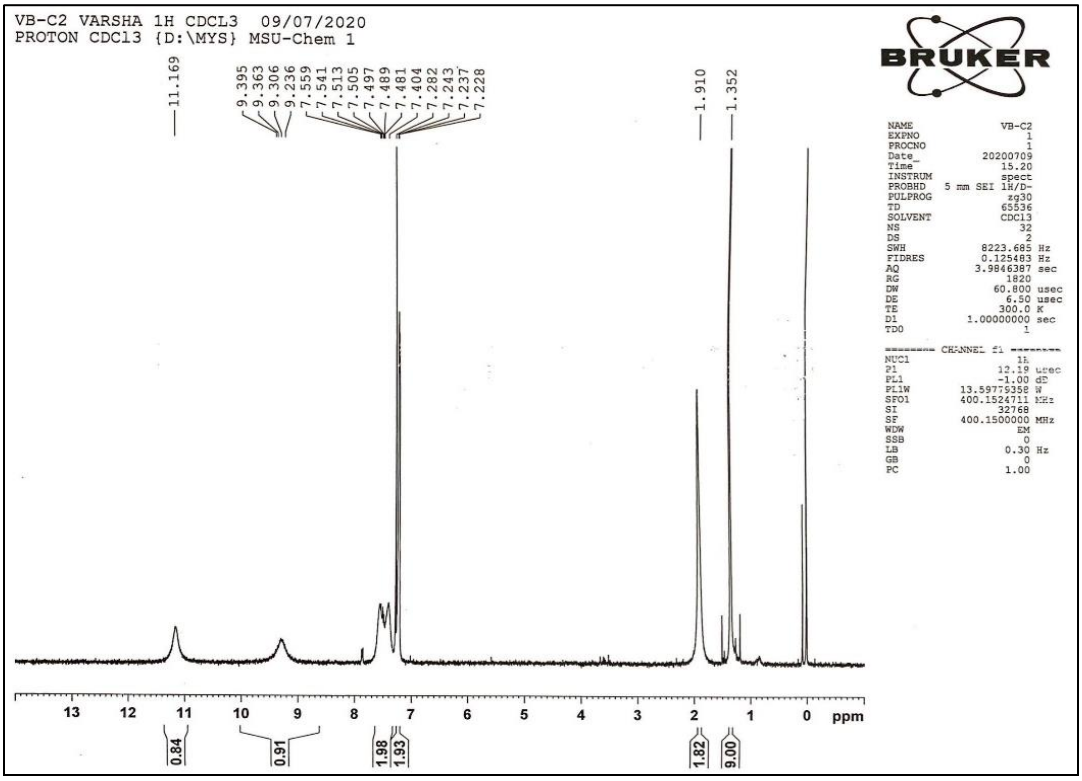
VB-C2 VARSHA 1H CDCL3 09/07/2020
PROTON CDCl3 {D:\MYS} MSU-Chem 1
11.169
9.395
9.363
9.306
9.236
7.559
7.541
7.513
7.505
7.497
7.489
7.481
7.404
7.282
7.243
7.237
7.228
1.910
1.352
BRUKER
ppm
0.84
0.91
1.98
1.93
1.82
9.00

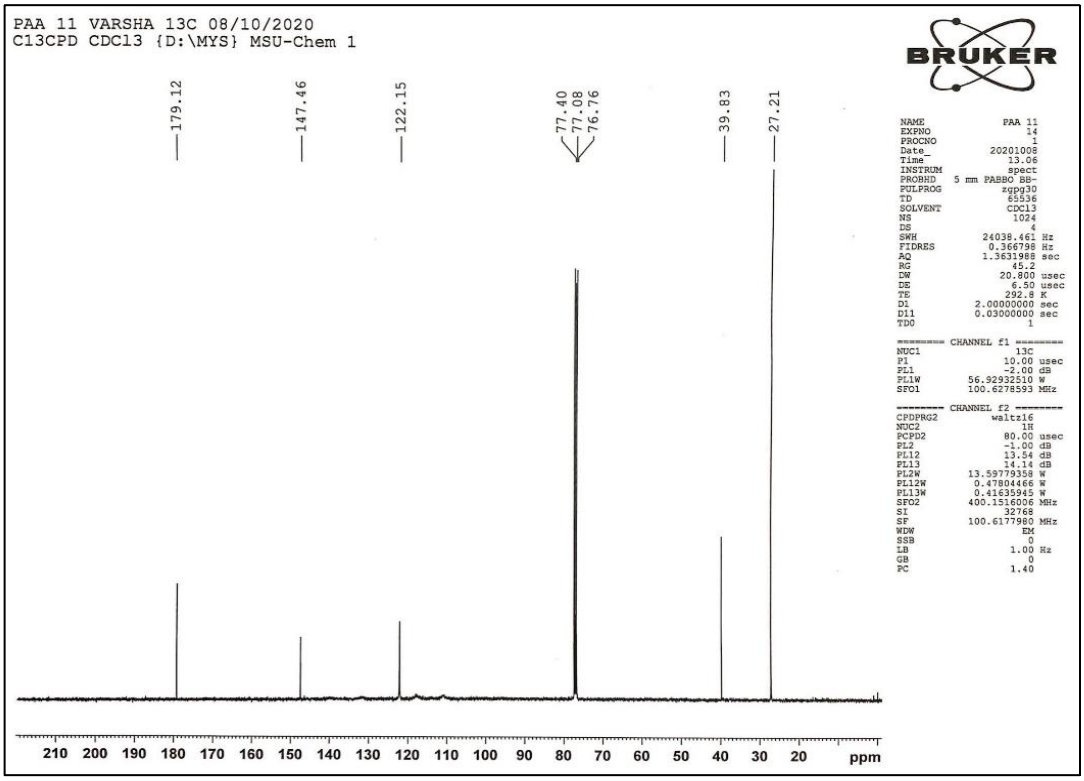
PAA 11 VARSHA 13C 08/10/2020
C13CPD CDCl3 {D:\MYS} MSU-Chem 1
179.12
147.46
122.15
77.40
77.08
76.76
39.83
27.21
BRUKER
ppm

FT-IR

L1

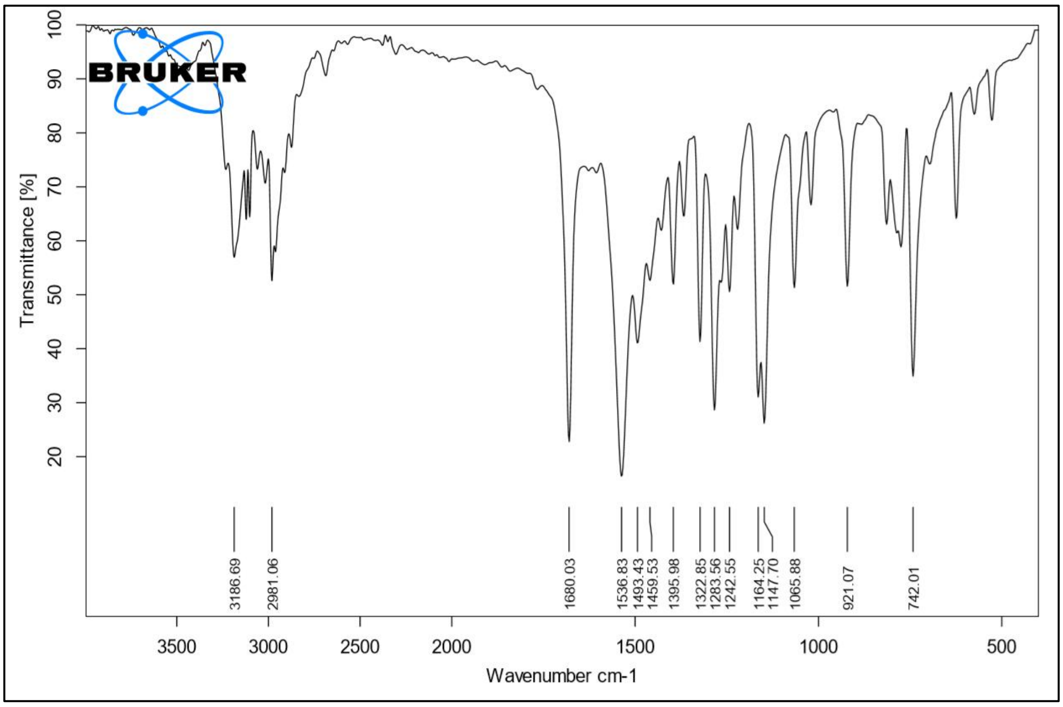
BRUKER
Transmittance [%]
100
90
80
70
60
50
40
30
20
3186.69
2981.06
1680.03
1536.83
1493.43
1459.53
1395.98
1322.85
1283.56
1242.55
1164.25
1147.70
1065.88
921.07
742.01
3500
3000
2500
2000
1500
1000
500
Wavenumber cm-1

L2

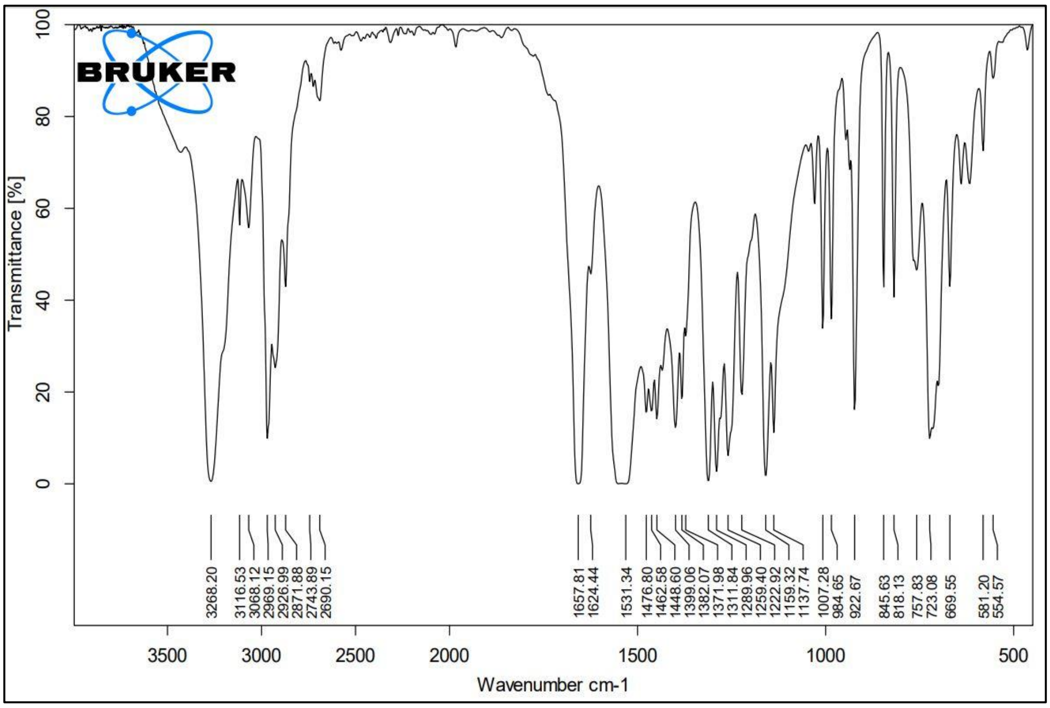
BRUKER
Transmittance [%]
100
80
60
40
20
0
3268.20
3116.53
3068.12
2969.15
2926.99
2871.88
2743.89
2690.15
1657.81
1624.44
1531.34
1476.80
1462.58
1448.60
1399.06
1382.07
1371.98
1311.84
1289.96
1259.40
1222.92
1159.32
1137.74
1007.28
984.65
922.67
845.63
818.13
757.83
723.08
669.55
581.20
554.57
3500
3000
2500
2000
1500
1000
500
Wavenumber cm-1

L3

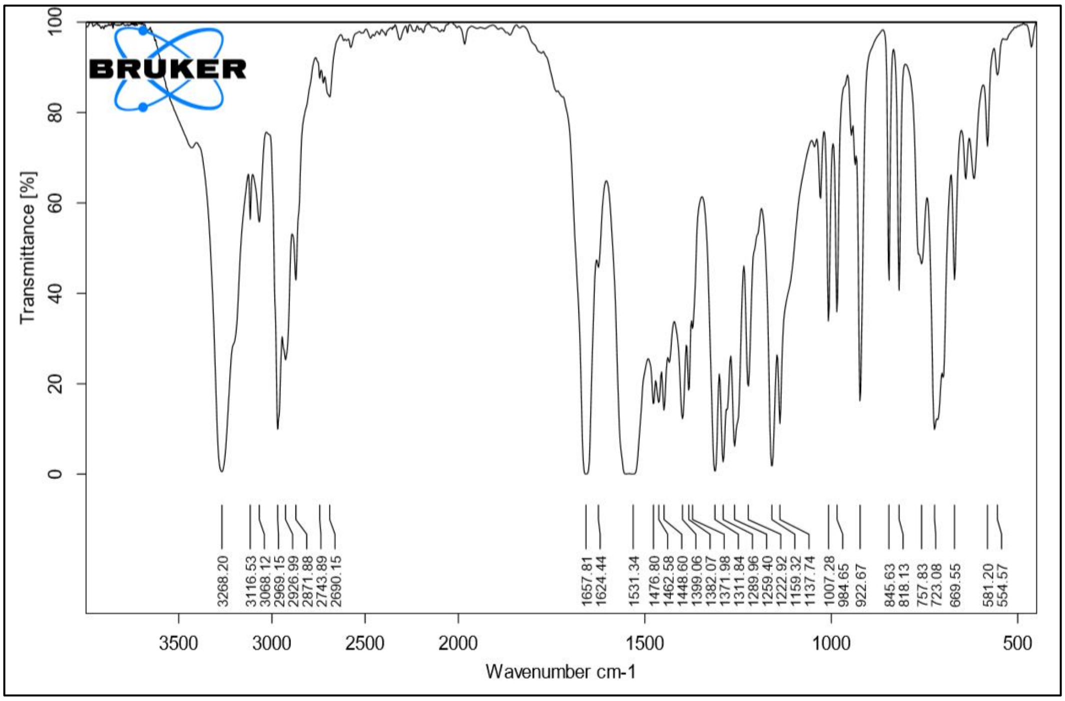
BRUKER
Transmittance [%]
100
80
60
40
20
0
3268.20
3116.53
3068.12
2969.15
2926.99
2871.88
2743.89
2690.15
1657.81
1624.44
1531.34
1476.80
1462.58
1448.60
1399.06
1382.07
1371.98
1311.84
1289.96
1259.40
1222.92
1159.32
1137.74
1007.28
984.65
922.67
845.63
818.13
757.83
723.08
669.55
581.20
554.57
3500
3000
2500
2000
1500
1000
500
Wavenumber cm-1

L4

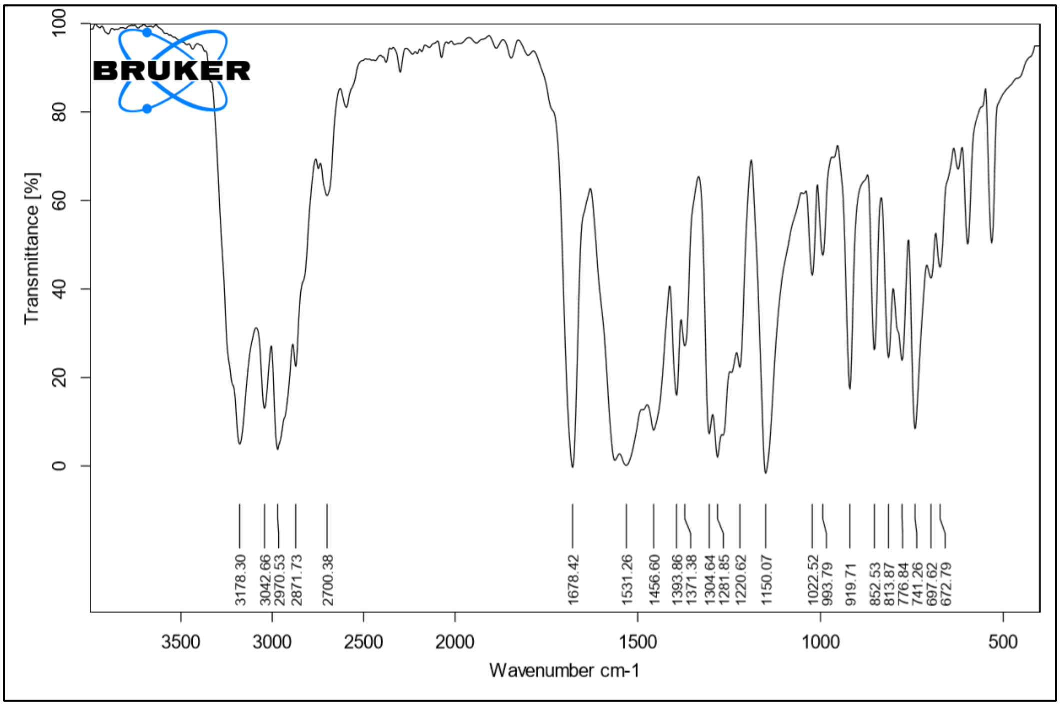
BRUKER
Transmittance [%]
100
80
60
40
20
0
3178.30
3042.66
2970.53
2871.73
2700.38
1678.42
1531.26
1456.60
1393.86
1371.38
1304.64
1281.85
1220.62
1150.07
1022.52
993.79
919.71
852.53
813.87
776.84
741.26
697.62
672.79
3500
3000
2500
2000
1500
1000
500
Wavenumber cm-1

L5

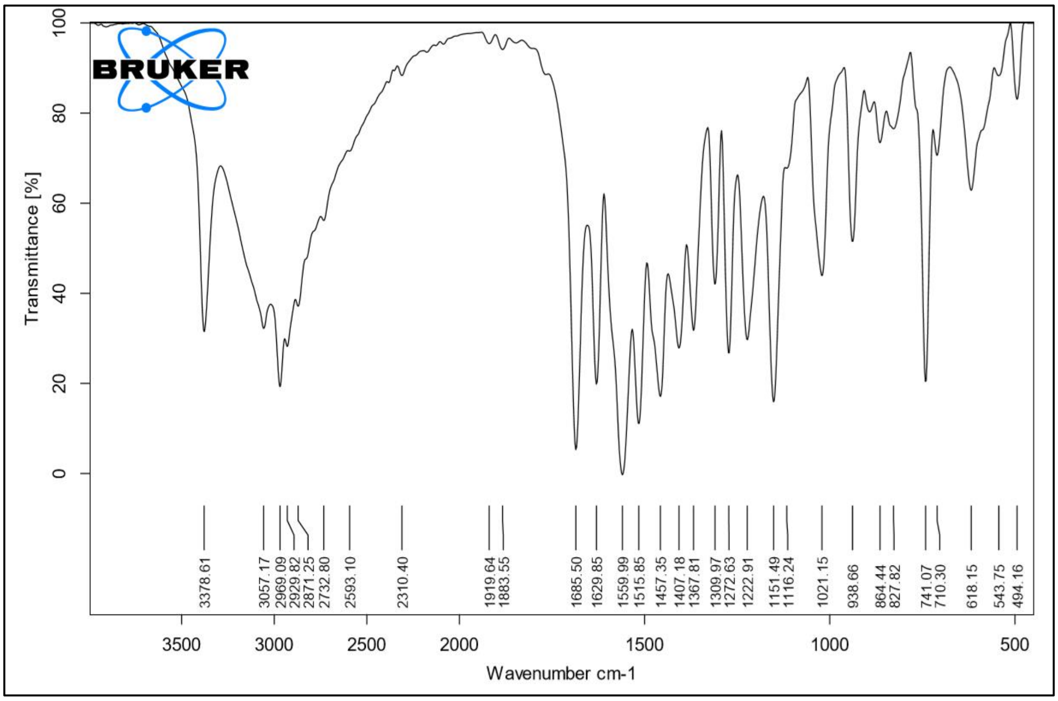

BRUKER
Transmittance [%]
100
80
60
40
20
0
3378.61
3057.17
2969.09
2929.82
2871.25
2732.80
2593.10
2310.40
1919.64
1883.55
1685.50
1629.85
1559.99
1515.85
1457.35
1407.18
1367.81
1309.97
1272.63
1222.91
1151.49
1116.24
1021.15
938.66
864.44
827.82
741.07
710.30
618.15
543.75
494.16
3500
3000
2500
2000
1500
1000
500
Wavenumber cm-1

C1

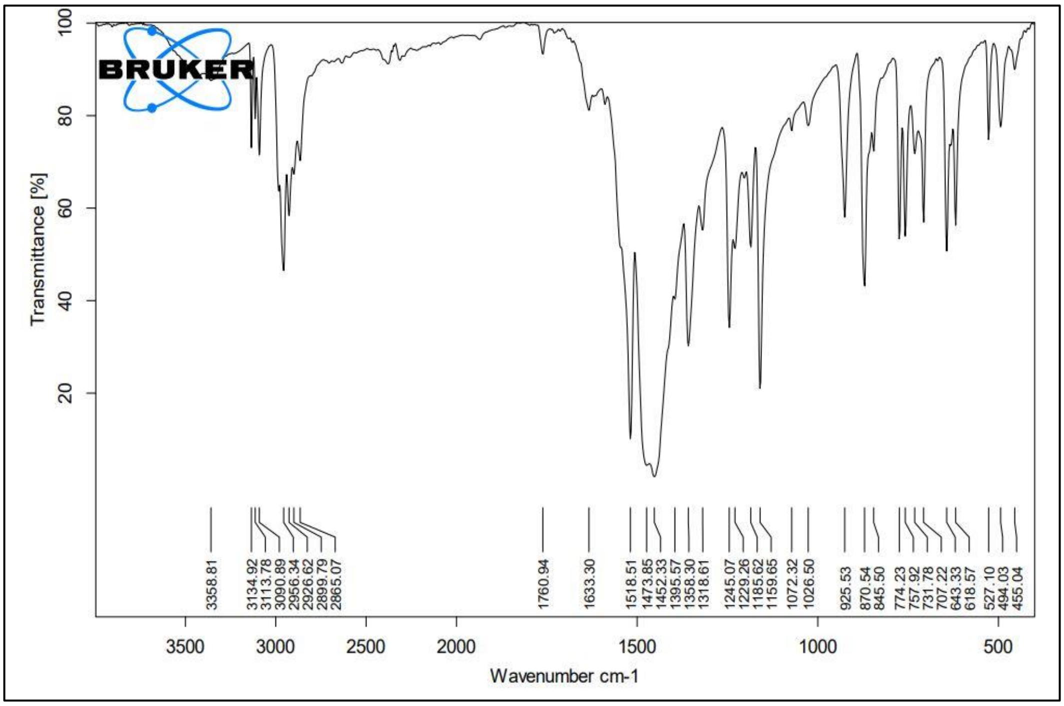
BRUKER
Transmittance [%]
Wavenumber cm-1
3358.81
3134.92
3113.78
3090.89
2956.34
2926.62
2899.79
2865.07
1760.94
1633.30
1518.51
1473.85
1452.33
1395.57
1358.30
1318.61
1245.07
1229.26
1185.62
1159.65
1072.32
1026.50
925.53
870.54
845.50
774.23
757.92
731.78
707.22
643.33
618.57
527.10
494.03
455.04

C3

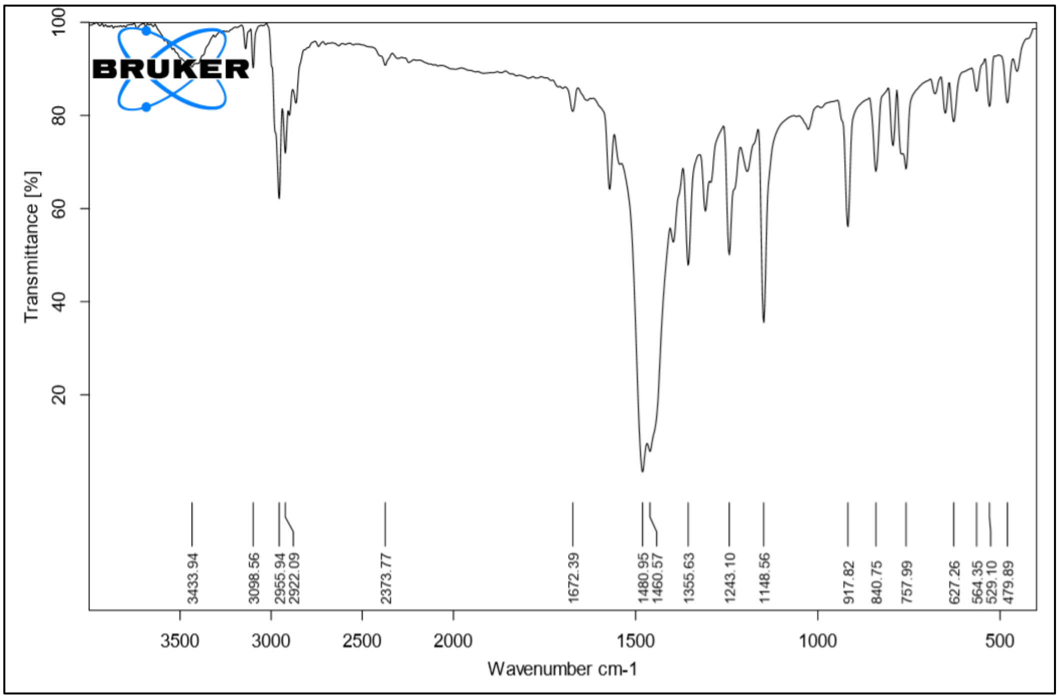
BRUKER
Transmittance [%]
Wavenumber cm-1
3433.94
3098.56
2955.94
2922.09
2373.77
1672.39
1480.95
1460.57
1355.63
1243.10
1148.56
917.82
840.75
757.99
627.26
564.35
529.10
479.89

C4

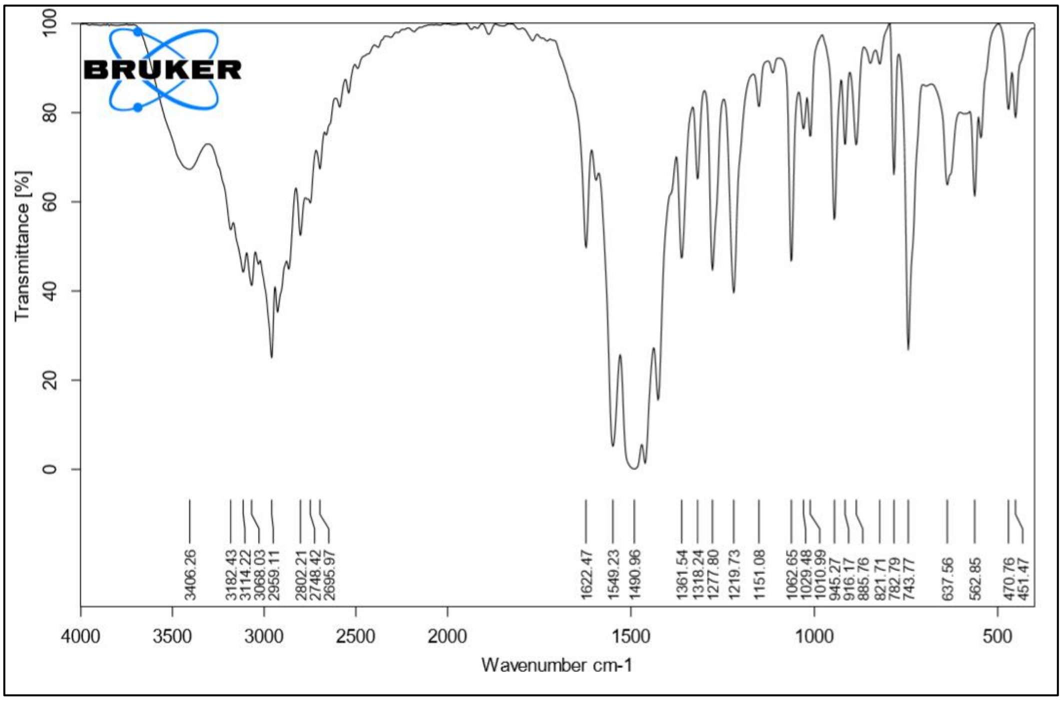
BRUKER
Transmittance [%]
0
20
40
60
80
100
3406.26
3182.43
3114.22
3068.03
2959.11
2802.21
2748.42
2695.97
1622.47
1549.23
1490.96
1361.54
1318.24
1277.80
1219.73
1151.08
1062.65
1029.48
1010.99
945.27
916.17
885.76
821.71
782.79
743.77
637.56
562.85
470.76
451.47
4000
3500
3000
2500
2000
1500
1000
500
Wavenumber cm-1

C5

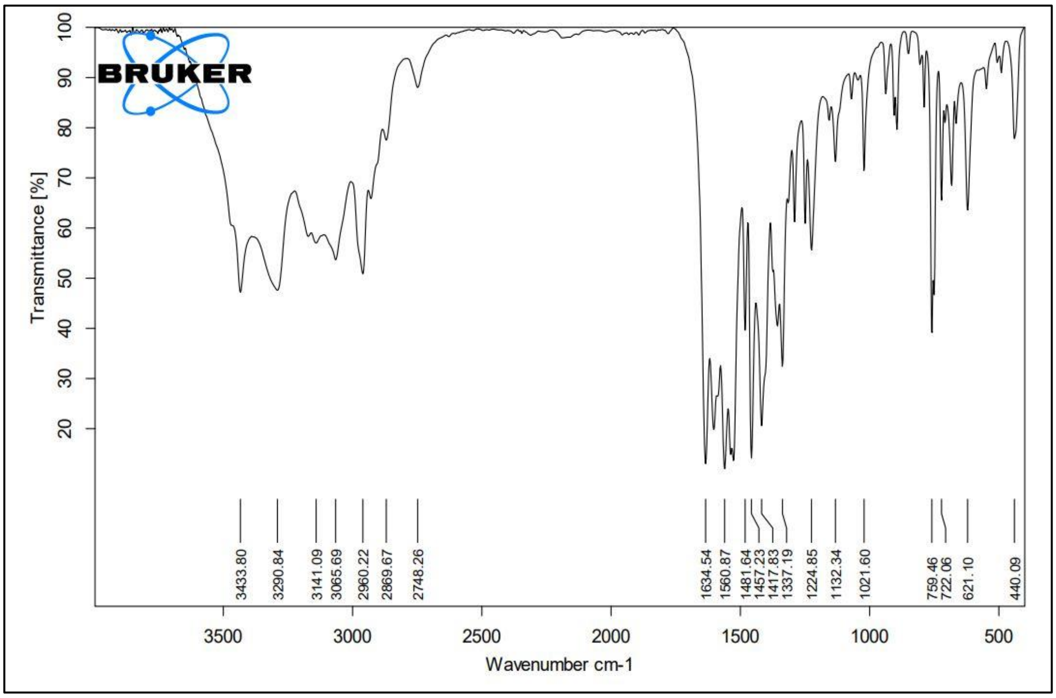
BRUKER
Transmittance [%]
20
30
40
50
60
70
80
90
100
3433.80
3290.84
3141.09
3065.69
2960.22
2869.67
2748.26
1634.54
1560.87
1481.64
1457.23
1417.83
1337.19
1224.85
1132.34
1021.60
759.46
722.06
621.10
440.09
3500
3000
2500
2000
1500
1000
500
Wavenumber cm-1

ESI-Mass

C1

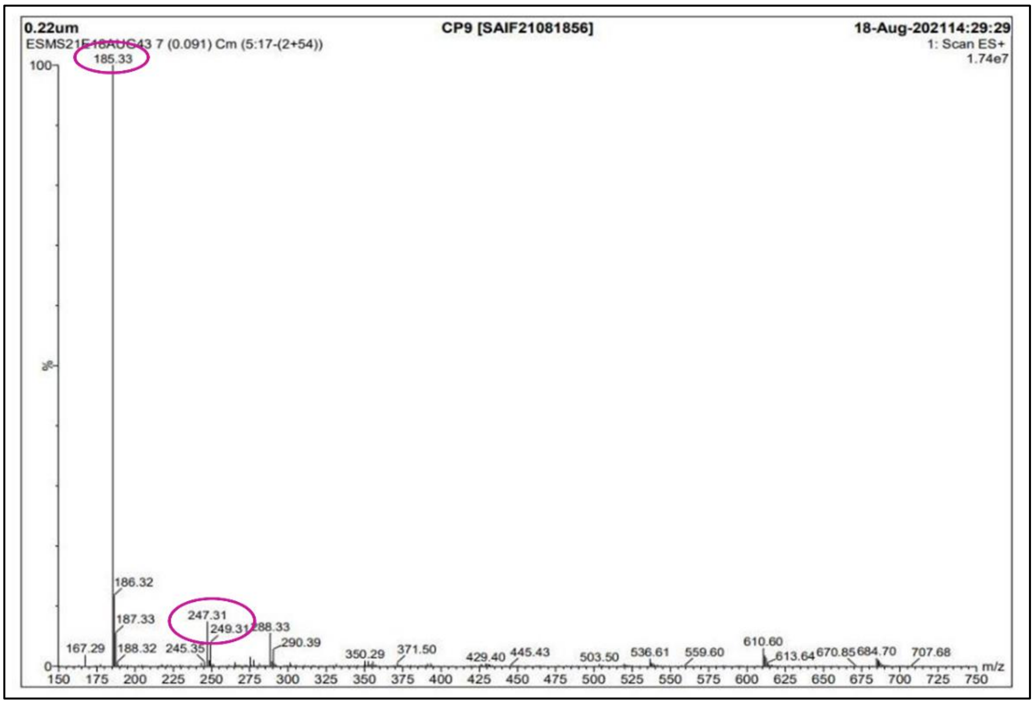

C3

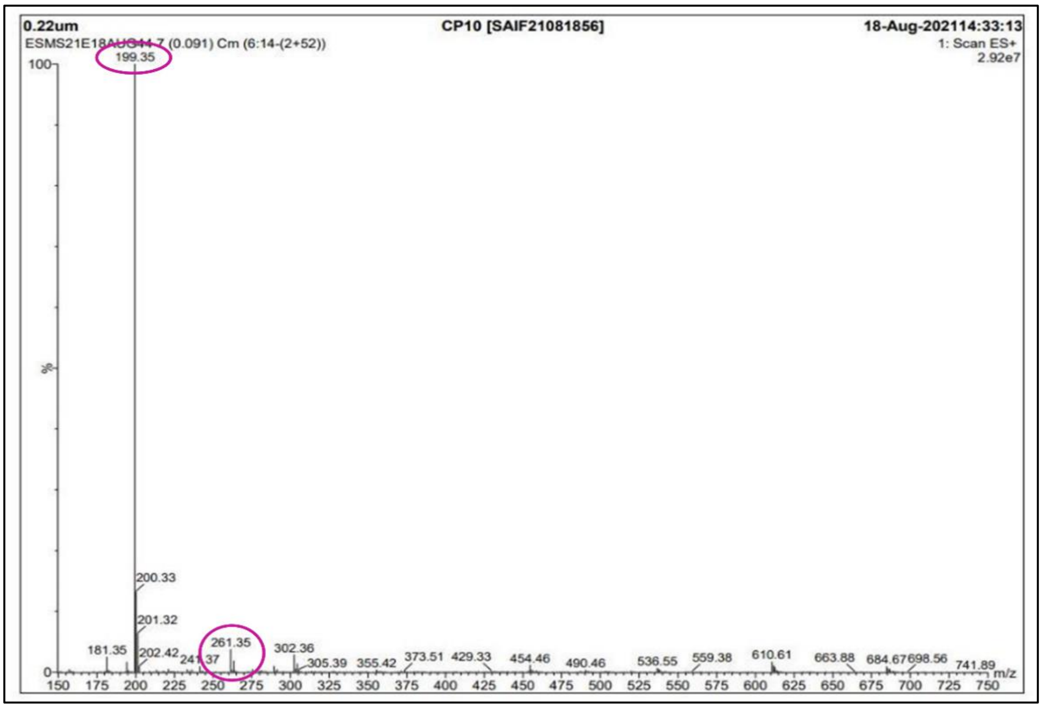

C4

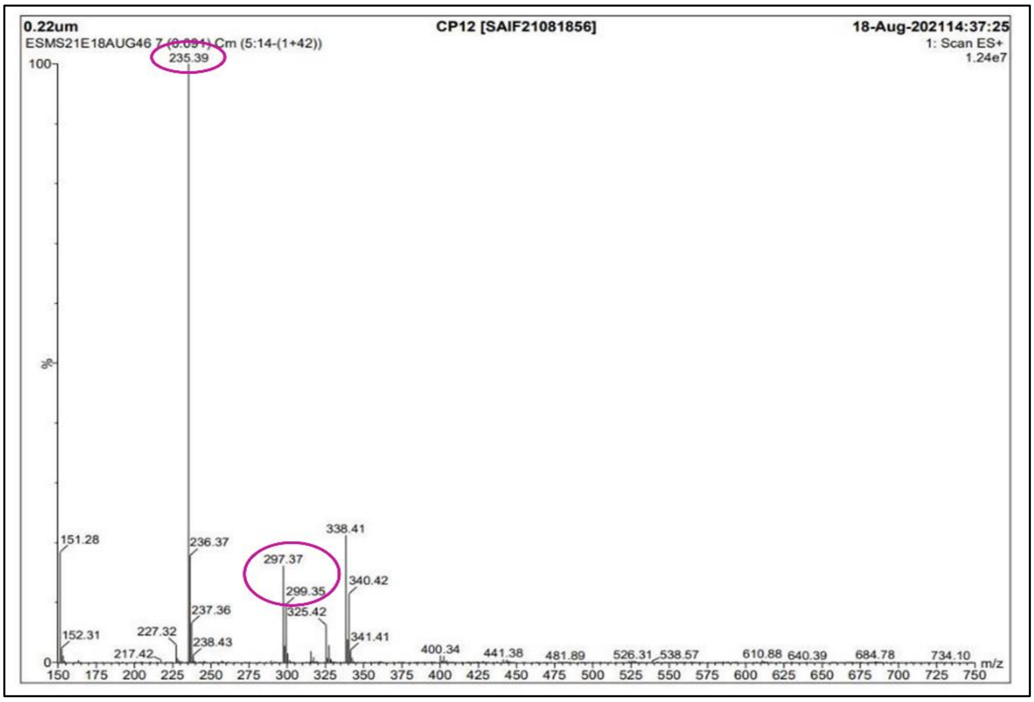
0.22um
CP12 [SAIF21081856]
18-Aug-202114:37:25
ESMS21E18AUG46 7 (0.091) Cm (5:14-(1+42))
1: Scan ES+
1.24e7
235.39
100
%
151.28
236.37
338.41
297.37
340.42
299.35
237.36
325.42
152.31
227.32
341.41
238.43
217.42
400.34
441.38
481.89
526.31
538.57
610.88
640.39
684.78
734.10
0
m/z
150 175 200 225 250 275 300 325 350 375 400 425 450 475 500 525 550 575 600 625 650 675 700 725 750

C5

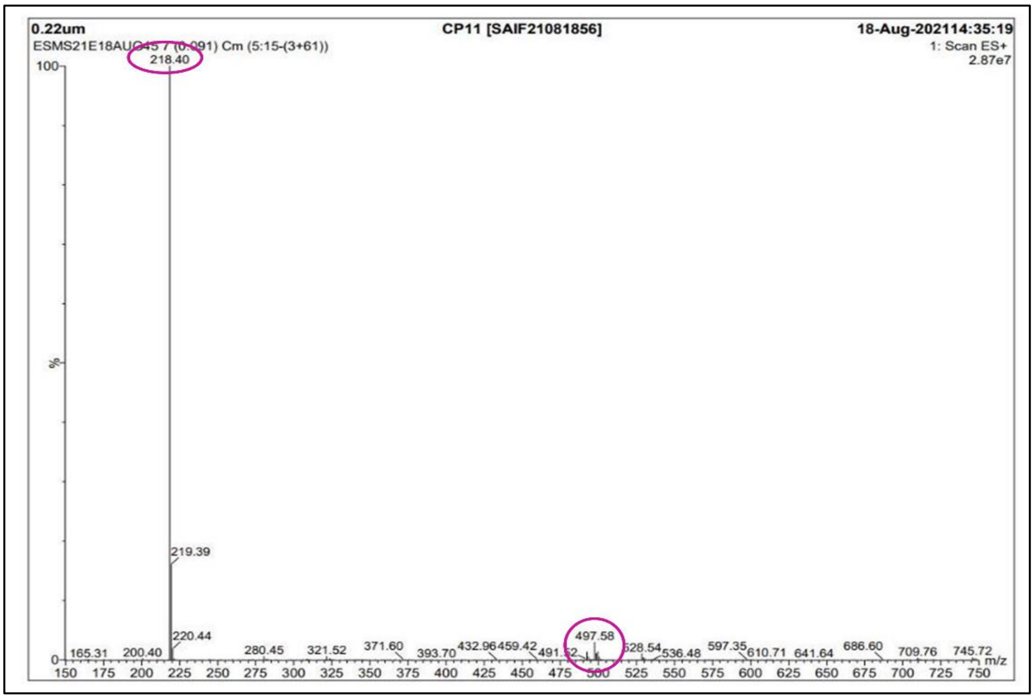
0.22um
CP11 [SAIF21081856]
18-Aug-202114:35:19
ESMS21E18AUG45 7 (0.091) Cm (5:15-(3+61))
1: Scan ES+
2.87e7
218.40
100
%
219.39
220.44
497.58
165.31
200.40
280.45
321.52
371.60
393.70
432.96
459.42
491.52
528.54
536.48
597.35
610.71
641.64
686.60
709.76
745.72
0
m/z
150 175 200 225 250 275 300 325 350 375 400 425 450 475 500 525 550 575 600 625 650 675 700 725 750

•